MULTISCALE MODELING OF GAS-FLUIDIZED BEDS

M.A. van der Hoef[1], M. Ye[1], M. van Sint Annaland[1], A.T. Andrews IV[2], S. Sundaresan[2] and J.A.M. Kuipers[1,*]

[1]**Department of Science & Technology, University of Twente, 7500 AE Enschede, The Netherlands**

[2]**Department of Chemical Engineering, Princeton University, Princeton, NJ 08544, USA**

*Corresponding author. Tel: +31 53 489 3039; Fax: +31 53 489 2882 E-mail: j.a.m.kuipers@tnw.utwente.nl

Advances in Chemical Engineering, vol. 31
ISSN 0065-2377
DOI 10.1016/S0065-2377(06)31002-2

Abstract

Numerical models of gas-fluidized beds have become an important tool in the design and scale up of gas-solid chemical reactors. However, a single numerical model which includes the solid-solid and solid-fluid interaction in full detail is not feasible for industrial-scale equipment, and for this reason one has to resort to a multiscale approach. The idea is that gas-solid flow is described by a hierarchy of models at different length scales, where the particle-particle and fluid-particle interactions are taken into account with different levels of detail. The results and insights obtained from the more fundamental models are used to develop closure laws to feed continuum models which can be used to compute the flow structures on a much larger (engineering) scale. Our multi-scale approach involves the lattice Boltzmann model, the discrete particle model, and the continuum model based on the kinetic theory of granular flow. In this chapter we give a detailed account of each of these models as they are employed at the University of Twente, accompanied by some illustrative computational results. Finally, we discuss two promising approaches for modeling industrial-size gas-fluidized beds, which are currently being explored independently at the Princeton University and the University of Twente.

I. Introduction

A. Gas-Fluidized Beds

Gas-fluidized beds consist of fine granular material (usually smaller than 5 mm) that are subject to a gas flow from below, large enough so that the gas drag on the particles can overcome the gravity and the particles can fluidize. When in the fluidized state, the moving particles work effectively as a mixer resulting in a uniform temperature distribution and a high mass transfer rate, which are beneficial for the efficiency of many physical and chemical processes. For this reason, gas-fluidized beds are widely applied in the chemical, petrochemical, metallurgical, environmental, and energy industries in large-scale operations involving adhesion optimized coating, granulation, drying, and synthesis of fuels and base chemicals (Kunii and Levenspiel, 1991). Lack of understanding of the fundamentals of dense gas–particle flows in general has led to severe difficulties in the design and scale-up of these industrially important gas–solid contactors (van Swaaij, 1985). In most cases, the design and scale-up of fluidized bed reactors is a fully empirical process based on preliminary tests on pilot-scale model reactors, which is a very time consuming and thus expensive activity.

Clearly, computer simulations can be a very useful tool to aid this design and scale-up process. Basically, such simulations can be used for two different

purposes. Firstly, to contribute to our *understanding*—that is, the simulations are used to obtain a fundamental insight into the complex dynamic behavior of dense fluidized suspensions, which should lead to an understanding based on elementary physical principles such as drag, friction, dissipation, etc.; this also includes the testing of elementary assumptions in theoretical models, such as the Maxwell velocity distribution of the particles. Secondly, the simulations can be used as a *design tool*, where the ultimate goal is to have a numerical model with *predictive* capabilities for the dense gas–particle flows encountered in engineering-scale equipment. Clearly, it will not be possible to have one single simulation method that can achieve this, but one rather needs a hierarchy of methods for modeling the flow phenomena on different length and time scales.

Obviously, these two items are not strictly separated; in contrast, the most fruitful approach is when they are simultaneously followed, so that they can mutually benefit from each other. In this chapter, we want to focus on the use of simulation methods as a design tool for gas-fluidized bed reactors, for which we consider gas–solid flows at four distinctive levels of modeling. However, before discussing the multilevel scheme, it is useful to first briefly consider the numerical modeling of the gas and solid phase separately.

B. Numerical Models for Gas and Solid Flows

1. Gas Phase

The description of a gas flow is well established from the micro- to macroscales. The length scale of a gas flow can be characterized by the local Knudsen number Kn, which is defined as

$$Kn = \frac{\lambda}{L}$$

where λ is the mean free path of the molecules and L is the characteristic length scale of the flow. The models to describe a gas flow are schematically shown in Fig. 1. For large-scale systems with $Kn < 0.01$, the gas flow can be described by ordinary fluid dynamics where the macroscopic fields (such as density and velocity) are formulated by Navier–Stokes equations in a three-dimensional (3D) coordinate space, together with no-slip boundary conditions. A number of well-developed numerical algorithms and meshing techniques in computational fluid dynamics (CFD) can be used to handle very complex geometries (Anderson, 1995). If the system becomes smaller, say $0.01 < Kn < 0.1$, the Navier–Stokes equations still hold, but caution must be exercised for the boundary conditions because partial slip might exist between the gas–solid interfaces. For a rarefied gas where $Kn > 0.1$, the continuum assumption breaks down, and the so-called kinetic theory of (dense) molecular gases should be applied. Kinetic theory differs from the ordinary fluid dynamics as there is just one field (the density of molecules) in the phase space. The basic equation in kinetic theory, in the

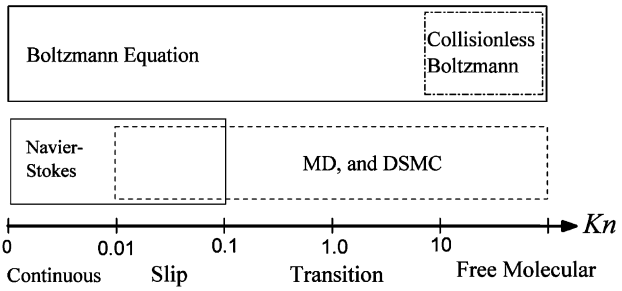

FIG. 1. The various levels of modeling gas flow.

simplest form, is the Boltzmann equation that describes the evolution of the density function f in a six-dimensional (6D) space (three coordinates and three velocity components) (Chapman and Cowling, 1970). At this scale, computational techniques such as molecular dynamics (MD) (Allen and Tildesley, 1990) and direct simulation Monte Carlo (DSMC) approach (Bird, 1976) can be very efficient. In these techniques, the motion of molecules is traced on an individual basis. Gas pressure and other transport coefficients, including gas viscosity and thermal conductivity, are obtained by methods from statistical mechanics (Chapman and Cowling, 1970). Molecules can be treated either as hard spheres or points with certain interaction potentials, depending on their physical properties. In the extreme case where the mean free path is very large compared to the system sizes (i.e., $Kn > 10$), the molecules move freely and just collide with the walls. This is the limit of *free molecular flow*, where the system behaves as an ideal gas.

Clearly, there are two quite different types of models for a gas flow: the continuum models and the molecular models. Although the molecular models can, in principle, be used to any length scale, it has been almost exclusively applied to the microscale because of the limitation of computing capacity at present. The continuum models present the main stream of engineering applications and are more flexible when applying to different macroscale gas flows; however, they are not suited for microscale flows. The gap between the continuum and molecular models can be bridged by the kinetic theory that is based on the Boltzmann equation.

2. *Solid Phase*

The methods used for modeling pure granular flow are essentially borrowed from that of a molecular gas. Similarly, there are two main types of models: the continuous (Eulerian) models (Dufty, 2000) and discrete particle (Lagrangian) models (Herrmann and Luding, 1998; Luding, 1998; Walton, 2004). The continuum models are developed for large-scale simulations, where the controlling equations resemble the Navier–Stokes equations for an ordinary gas flow. The discrete particle models (DPMs) are typically used in small-scale simulations or

in the investigation of the detailed physics of granular flow. A kinetic theory of granular flow (KTGF) has also been proposed to connect the microscale picture of granular flow to the macroscale description (Jenkins and Savage, 1983; Lun *et al.*, 1984).

However, a granular flow differs significantly from a molecular gas flow. The collisions between molecules are elastic, and the kinetic energy is conserved in isothermal systems. For the molecular gas, there is a well-defined equilibrium state in the absence of external energy sources, and one can define a thermal temperature based on the internal kinetic energy. The interaction between macroscopic particles, however, is far more complicated. The collision between two macroscopic particles will come with surface friction and elastic–plastic deformation, which leads to the dissipation of kinetic energy. This inelasticity forms the primary feature of granular flow that differentiates it from a molecular gas (Campbell, 1990). Clearly, without any external energy sources, a granular system will continuously ''cool down,'' and an equilibrium state can never be reached.

To model granular systems, DPMs using the same techniques as MD methods can be used, where it is assumed that the particle motion can be well described by the Newtonian equations. However, in order to establish a continuum description, a number of serious difficulties are encountered when one tries to describe the fields in phase space. First, an energy source term and a dissipative term should be included in the Boltzmann equations, which complicates the (approximate) solution. Also, particle sizes may show a certain distribution even for the same type of materials. It is well known that a difference in particle sizes will result in the segregation of granular materials (e.g., the Brazil nut effect). Furthermore, in most granular flows the effect of gravity cannot be ignored, which introduces an anisotropy in the velocity fluctuation of particles. Clearly, the definitions of the particle-phase pressure and other transport coefficients are not straightforward because normally a homogeneous equilibrium state does not exist. For these reasons, the construction of a reliable hydrodynamical model for granular flow offers a great challenge for both scientists and engineers (Goldhirsch, 1999).

3. *The Interphase Coupling*

The prime difficulty of modeling two-phase gas–solid flow is the interphase coupling, which deals with the effects of gas flow on the motion of solids and vice versa. Elgobashi (1991) proposed a classification for gas–solid suspensions based on the solid volume fraction ε_s, which is shown in Fig. 2. When the solid volume fraction is very low, say $\varepsilon_s < 10^{-6}$, the presence of particles has a negligible effect on the gas flow, but their motion is influenced by the gas flow for sufficiently small inertia. This is called ''one-way coupling.'' In this case, the gas flow is treated as a pure fluid and the motion of particle phase is mainly controlled by the hydrodynamical forces (e.g., drag force, buoyancy force, and so

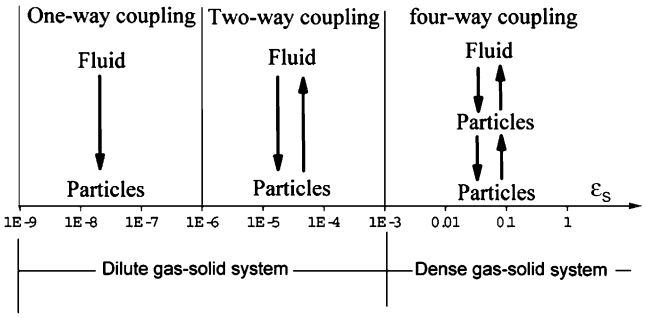

FIG. 2. Interphase coupling. Based on Elgobashi, *Appl. Sci. Res.* (1991).

on), while the particle–particle interaction is assumed to be irrelevant. With increasing solid volume fraction up to $\varepsilon_s < 10^{-3}$, the effects of the particle phase on the gas-phase flow pattern will become important. In this region, turbulent structures encountered in gas flows can be modified by the presence of particles. It is commonly accepted that particle–particle interactions still do not play a dominant role in this regime, which we normally refer to as "two-way coupling." For even higher solid volume fractions ($\varepsilon_s > 10^{-3}$), the momentum of particles will be transported not only by the free-flight mechanism but also by the collisions between particles and particles with the confining walls. This means that the particle–particle interaction will be very important and "four-way coupling" should be taken into account. Note that it is precisely this dense-particle regime that is important for the industrial applications of two-phase flows. However, a numerical model that includes the solid–solid and solid–fluid interactions in full detail is not feasible for industrial-scale equipment, and for this reason one has to resort to a multilevel approach.

C. The Multi Level Modeling Approach for Gas–Solid Flows

As mentioned previously, the construction of reliable models for large-scale gas–solid contactors is seriously hindered by the lack of understanding of the fundamentals of dense gas–particle flows (van Swaaij, 1985). In particular, the phenomena that can be related to the effective gas–particle interaction (drag forces), particle–particle interactions (collision forces), and particle–wall interaction are not well understood (Kuipers and van Swaaij, 1998; Kuipers *et al.*, 1998). The prime difficulty here is the large separation of scales: the largest flow structures can be of the order of meters, and yet, these structures are directly influenced by details of the particle–particle and particle–gas interactions, which take place on the scale of millimeters, or even micrometers. As shown above, for both the gas and particle phase, continuum-(Eulerian) and discrete-(Lagrangian) type of models can be applied, depending on the length scales involved. Thus, in order to model gas–solid two-phase flows at different scales, one can

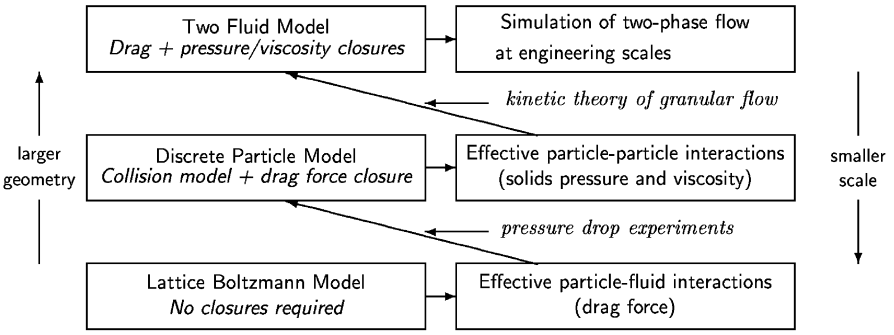

FIG. 3. Multilevel modeling scheme.

choose appropriate combinations of the gas- and solid-phase models, where in all cases a four-way coupling is used either directly or effectively, depending on the scale of the simulation. The basic idea is that the smaller scale models, which take into account the various interactions (fluid–particle, particle–particle) in detail, are used to develop closure laws that can represent the effective "coarse-grained" interactions in the larger scale models. Note that it is not guaranteed that some subtle correlations between small- and large-scale processes exist, which cannot be captured by effective interactions. However, experience has shown that in many cases the main characteristics of gas–solid flows can be well described by the use of closure relations. In this chapter, we discuss three levels of modeling: the lattice Boltzmann model (LBM), the DPM and the two-fluid model (TFM) based on the KTGF. In Fig. 3, we show a schematic representation of the three models, including the information that is abstracted from the simulations, which is incorporated in higher scale models via closure relations, with the aid of experimental data or theoretical results. We will next give a brief description of each of these models.

1. *Two-Fluid Model*

At the largest scale, a continuum description is employed for both the solid phase and the gas phase, and a CFD-type Eulerian code is used to describe the time evolution of the local mass and momentum density of both phases (see Refs. Kuipers *et al.*, 1992 and Gidaspow, 1994 amongst others). In a more sophisticated model, based on the KTGF, also the local granular temperature of the solid phase is a dynamical variable, and thus included in the update. With modernday computers, the TFM model can predict the flow behavior of gas–solid flows of systems with a linear dimension of the order of 1 m, denoted as the "engineering" scale, corresponding typically to the size of pilot plants, which is in between the laboratory scale (0.1 m) and the industrial scale (10 m). The TFM relies heavily on closure relations for the effective solid pressure and viscosity, and gas–solid drag. The basic idea of the multiscale modeling is that

these relations are obtained from kinetic theory and from numerical data collected in the more detailed scale models.

2. *Discrete Particle Model*

At one level higher in detail (and thus smaller in scale), we have the DPM. Here the continuum description for the solid phase is replaced by a description with discrete particles, which are modeled by spheres (Hoomans *et al.*, 1996, 2000). The flow field is still continuous and updated by the same methods as in the TFM, where the scale at which the gas flow field is described is an order of magnitude larger than the particles (a CFD-grid cell typically contains $O(10^2)$–$O(10^3)$ particles). The motion of the particles is governed by Newton's law, where the forces on the particles are integrated using standard schemes for ordinary differential equations (ODEs). These forces follow from the interaction with the fluid phase and collisions with the other particles. Therefore, both a drag-force closure and a collision model have to be specified for this level of modeling. The advantage of this model is that it can account for the particle–wall and particle–particle interactions in a realistic manner. This model allows one to validate (and modify) the viscosity and pressure closures derived from the KTGF, which are used in the TFM simulations. Still, a closure law for the effective momentum exchange between the two phases has to be specified for this model. The system sizes that can be studied are of the order of $O(10^5)$ particles, which corresponds (for millimeter-sized particles) to systems that have a linear dimension of the order of 0.1 m (i.e., laboratory scale).

3. *Lattice Boltzmann Model*

At the most detailed level of description, the gas flow field is modeled at scales *smaller* than the size of the solid particles. The interaction of the gas phase with the solid phase is incorporated by imposing "stick" boundary conditions at the surface of the solid particles. This model thus allows one to measure the effective momentum exchange between the two phases, which is a key input in all the higher scale models. A particularly efficient method to solve the flow field between the spheres is the LBM (Ladd, 1994; Ladd and Verberg, 2001), although in principle other direct numerical simulation (DNS) techniques can also be used. The number of particles in such a simulation is typically around 500, which is sufficiently high to account for swarm effects. The goal of these simulations is to construct drag laws for dense gas–solid systems. For low Reynolds numbers (Re), the functional form of the drag law can be derived from theory using the Carman–Kozeny approximation, where the simulation data is then used to determine the unknown parameters such as the Kozeny constant. For higher Reynolds numbers, a theoretical evaluation of the functional form is not possible and the drag law is simply constructed as the best possible fit to the simulation data, where the functional form is dictated by a compromise between

simplicity and accuracy. For both low and high Reynolds numbers, the drag laws are validated (and possibly adjusted) on the basis of pressure-drop data.

A graphical representation of the multilevel approach is shown in Fig. 4. All three models are now commonly accepted and are widely used by a number of research groups (both academic and industrial) around the world. In a recent paper, we have given an overview of the three models as they are employed at the University of Twente, together with some illustrative examples (Van der Hoef *et al.*, 2004). In this chapter, we will focus on the technical details of each of the models, much of which has not been published elsewhere. The development of detailed closure relations from the simulations, as indicated in Fig. 3, is still ongoing. Some preliminary results for both the drag-force closures and solid pressure will be presented in the Sections II and III. In this chapter, we will

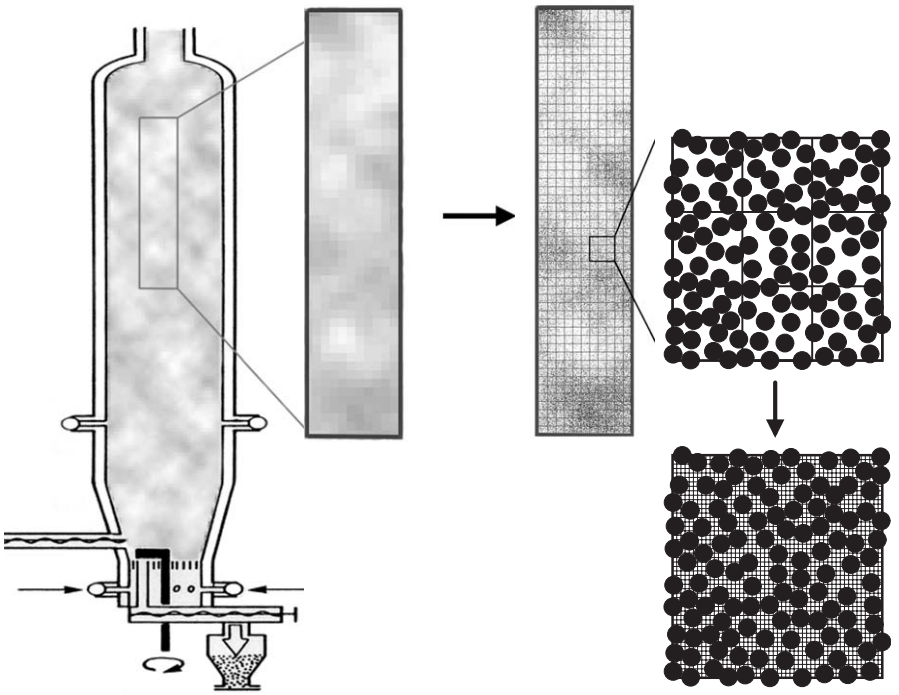

FIG. 4. Graphical representation of the multilevel modeling scheme. The arrows represent a change of model. On the left is a fluidized bed on a life-size scale, a section of which is modeled by the two-fluid model (TFM) (see enlargement), where the shade of grey of a cell indicates the solid-phase volume fraction. On the right, the same section is modeled using discrete particles. The gas phase is solved on the same grid as in the TFM. The bottom graph shows the most detailed level, where the gas phase is solved on a grid much smaller than the size of the particles. Note that in reality, the separation in scales is much more extreme, and also that the section that can be modeled by the TFM of the industrial-scale fluidized bed is much smaller.

only consider monodisperse systems, but nevertheless we will formulate the soft-sphere model in Section III.B for general polydisperse systems where a particle a has an individual radius R_a. Apart from Section III.B, the size of the particles are indicated by a single radius R or a diameter d.

Finally, we note that the TFM can simulate fluidized beds only at engineering scales corresponding typically to the size of pilot plants, and the industrial-scale fluidized bed reactors (diameter 1–5 m, height 3–20 m) are still far beyond its capabilities. In Section V, we discuss two promising approaches for modeling large-scale gas–solid flow, which are currently being explored independently at the Princeton University and the University of Twente. We stress, however, that these approaches are still under development and that they should be recognized as only preliminary.

II. Lattice Boltzmann Model

As mentioned in Section I, there are two fundamentally different types of models to describe a gas flow: the continuum models and the molecular models. In principle, the molecular models can be applied at any length scale; however, in practice this is limited to microscopic scales only because of the limitation of computer time. The continuum models present the main stream of engineering applications and are more flexible when applying to different macroscale gas flows. The gap between the continuum and molecular models can be bridged, however, by the lattice Boltzmann (LB) simulation model that applies at a "mesoscopic" scale, which is in between fully microscopic and macroscopic scales. The LB model that is currently the most widely used—the lattice Bhatnagar–Gross–Krook (BGK) model—is nothing but a finite difference version of the continuous, macroscopic BGK equation introduced in 1954 (Bhatnagar *et al.*, 1954). Historically, however, this LB model has evolved from the microscopic lattice-gas simulation models for fluids, and we will also follow this route here.

A. From Lattice-Gas to Lattice-Boltzmann

1. Lattice-Gas Models

As mentioned earlier, in principle, one can model the dynamics of a simple classical fluid by means of MD simulations. This technique, although straightforward, is relatively time-consuming, and therefore not suitable for observation of large-scale "macroscopic" phenomena in the fluid. However, one often does not need such a detailed description of the microdynamics as provided by MD. In such cases, it would be more efficient to strip the MD model down to its barest essentials, where the only requirement is that the model behaves like a fluid macroscopically, but is still atomistic in character—i.e., the mechanism underlying the fluid motion is the movement of particles. From the derivation of

the fluid dynamics equations it is clear that a key ingredient in such a model must be local conservation of mass and momentum. The simplest model to think of would be one with a single species of particles moving on a lattice with discrete velocities. In 1985, such a model was introduced for two-dimensional (2D) fluid flow by Frisch *et al.* (1986), where particles move on a triangular lattice. Such a lattice has just enough symmetry to guarantee isotropic, macroscopic equations of motion. The rules and basic idea of the FHP model are illustrated in Fig. 5. Later, the model has been extended to three dimensions as well. From the update rules it is clear that lattice-gas cellular automata (LGCA) make an efficient simulation scheme, in particular on a parallel computer, since the rules are completely local. Moreover, stability of the algorithm is guaranteed, since the update involves only bit manipulation, i.e., the update is exact with no round-off errors. We will continue with a more formal description of general LGCA models.

2. *Definitions and Equation of Motion*

In LGCA models, time and space are discrete; this means that the model system is defined on a lattice and the state of the automaton is only defined at regular points in time with separation δt. The distance between nearest-neighbor sites in the lattice is denoted by δl. At discrete times, particles with mass m are situated at the lattice sites with b possible velocities $\mathbf{c}_i$, where $i \in \{1, 2, \ldots, b\}$. The set $\mathbf{c}_i$ can be chosen in many different ways, although they are restricted by the constraint that

$$\mathbf{r}' = \mathbf{r} + c_i \delta t \tag{1}$$

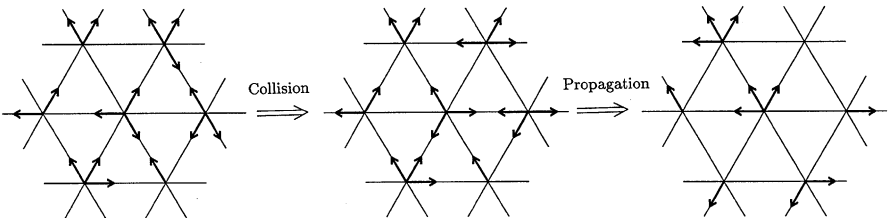

FIG. 5. Example of the time evolution in a small section of the FHP model. In the figure, each arrow represents the velocity of a single particle. The particles are situated at the lattice sites. The update of the lattice consists of two steps. First there are local collisions at all sites, simultaneously, and such that locally the number of particles and momentum is conserved. Note that only some cases lead to a new configuration. The next step is a propagation step: all the particles move simultaneously according to their velocities to neighboring sites. Particles do not interact during this step. Note that the figure only represents a small section of the lattice; therefore, we can only give the complete final configuration of the central site, as the state of the other sites after the propagation depends on neighboring sites that are not shown. Next there will again be a collision step, etc.

where $\mathbf{r}$ and $\mathbf{r}'$ must be lattice sites. Apart from Eq. (1), it has been proved essential to have additional symmetry requirements on the velocity set in order to get isotropic, macroscopic behavior from these models. These requirements turn out to be that the even-rank tensors that can be constructed from the velocity set are isotropic up to 4th rank, and the odd-rank tensors are zero. The time evolution of the LGCA consists of two steps:

1. Propagation: All particles move in one time step δt from their initial lattice position $\mathbf{r}$ to a new lattice position $\mathbf{r}' = \mathbf{r} + \mathbf{c}_i \delta t$.
2. Collision: The particles at all lattice sites undergo a collision that conserves the total number of particles and the total momentum at each site. The collision rules may or may not be deterministic.

The state of the automaton at time t can be completely determined by the "boolean" variable $n_i(\mathbf{r},t)$, which is equal to 1(0) if a particle is present (absent) on site $\mathbf{r}$ with velocity $\mathbf{c}_i$. From this it follows that the local microscopic density $\tilde{\rho}$ and flow velocity $\tilde{\mathbf{u}}$ at site $\mathbf{r}$ are given by

$$\tilde{p}(\mathbf{r}, t) = m \sum_i n_i(\mathbf{r}, t), \quad \tilde{p}(\mathbf{r}, t)\tilde{u}(\mathbf{r}, t) = m \sum_i n_i(\mathbf{r}, t)\mathbf{c}_i \tag{2}$$

with m as the mass of the particles. The update of $n_i(\mathbf{r},t)$ (from propagation and collision) can formally be written by the following equation of motion:

$$n_i(\mathbf{r} + \mathbf{c}_i\delta t, t + \delta t) = n_i(\mathbf{r}, t) + \Delta_i(n(\mathbf{r}, t)) \tag{3}$$

with

$$\Delta_i(n(\mathbf{r}, t)) = \sum_{s,s'} (s_i' - s_i)\xi(s, s') \prod_j n_j^{sj}(1 - n_j)^{1-sj}$$

With the sum is over all possible states s and s' of a single site, and $\xi(s, s')$ is a collision function that is equal to one for states s, s' where s goes over into s' in a collision, and zero for all other possible pairs of states. Note that expression in Eq. (3) is the formal expression for the update. In a numerical code, the state $n_i(\mathbf{r},t)$ of the systems is represented by a b—bit word for every site r at time t. The collision process can then be done by a very quick table lookup; whereas, for the propagation step the bits from one word have to be put at the same bit positions in the words describing the states of the neighboring sites. Despite its extremely simplified microdynamical behavior, it turns out that the analogy of these models with the "real" fluid models is very close, such that the theoretical framework of statistical mechanics of simple fluids can be applied, to a great extent, to these discrete fluids. That is, starting from the formal expression in Eq. (3), it can be proven that the macroscopic equations of motions are, in a well-defined limit, equivalent to the Navier–Stokes equations (Frisch *et al.*, 1987; Ernst and Dufty, 1989). This solid theoretical basis makes the LGCA method not just a toy model of computer scientists but also a numerical scheme that can be seriously

considered for the study of hydrodynamic flow phenomena. However, such an application is seriously hindered by two big drawbacks of LGCA. Firstly, their inherent noisiness, which means that massive averaging is required to get accurate numbers. And secondly, it turns out that the method is not suitable for modeling fluid flow at Reynolds numbers above $Re = 100$, which is related to the fact that the viscosity cannot be made lower than a certain value, since it is dictated by the collision function ξ. It is for these reasons that the current class of LGCA methods cannot compete with CFD methods for modeling large-scale fluid flow.

3. *Averaged Equation of Motion*

The two drawbacks mentioned above can be overcome, however, by considering the *ensemble-averaged* version of the microscopic equation of motion, Eq. (3):

$$f_i(\mathbf{r} + \mathbf{c}_i\delta t, t + \delta t) = f_i(\mathbf{r}, t) + C_i(f(\mathbf{r}, t)) \tag{4}$$

with $f_i(\mathbf{r},t) = \langle n_i(\mathbf{r},t) \rangle$—the average occupation number of link i at site r and time t, which is now a floating number between zero and one, and

$$C_i(f) = \langle \Delta_i(n) \rangle = \sum_{s,s'} (s_i' - s_i)\ \ \xi(s, s')\ \ \prod_j f_j^{s_j} (1 - f_j)^{1 - s_j} \tag{5}$$

where in the second step the assumption is made that the particle occupation numbers on a single site are not correlated, so that the average of the product can be written as the product of the average. The ensemble averaged density ρ and flow velocity $\mathbf{u}$ follow from Eq. (2):

$$\rho = \langle \tilde{\rho} \rangle = m \sum_i f_i, \qquad \rho \mathbf{u} = \langle \tilde{\rho} \tilde{\mathbf{u}} \rangle = m \sum_i f_i\, \mathbf{c}_i \tag{6}$$

where we have omitted the space and time dependence. In its present form, the collision operator in Eq. (5) is not very useful for simulations, since the update of f_i at each site requires the double sum over all possible states, where there are over 16 million states (2^{24}) for the 3D models. This problem can be circumvented by expanding the collision function about the equilibrium distribution function f_i^{eq}, for which it holds that $C(f_i^{\mathrm{eq}}) = 0$:

$$f_i(\mathbf{r} + \mathbf{c}_i\delta t,\ \ t + \delta t) = f_i(\mathbf{r}, t) + \sum_{j=1}^{b} L_{ij}(f_j(\mathbf{r}, t) - f_j^{\mathrm{eq}}(\mathbf{r}, t)) \tag{7}$$

where L is the linearized collision operator:

$$L_{ij} = \left(\frac{\partial C_i}{\partial f_j} \right)_{f_j\ =\ f_j^{\mathrm{eq}}}$$

which can be evaluated directly from Eq. (5). Note that L, which has to be calculated only *once* for a given set of collision rules, is now a small $b \times b$ matrix, compared to ξ that is a $2^b \times 2^b$ matrix. Equation (7) can be directly converted into an algorithm for simulation purpose. The advantage of an LB simulation is that the system is essentially free of noise. Also, the linearized collision operator need not necessarily be evaluated from an existing set of microscopic collision rules $\xi(s, s')$. One is free to define any operator L, which has the correct symmetry and conserves momentum and number of particles. As an example, for the 2D hexagonal lattice, one can derive from the requirements of symmetry and conservation that L should have the following form:

$$L = \begin{pmatrix} a & b & c & d & c & b \\ b & a & b & c & d & c \\ c & b & a & b & c & d \\ d & c & b & a & b & c \\ c & d & c & b & a & b \\ b & c & d & c & b & a \end{pmatrix} \tag{8}$$

with

$$a = -\frac{4}{21} + \frac{1}{3}\lambda, \quad b = \frac{1}{7} - \frac{1}{6}\lambda, \quad c = \frac{4}{21} - \frac{1}{6}\lambda, \quad d = \frac{1}{7} + \frac{1}{3}\lambda$$

where λ can take any value between 0 and 2 and is related to the kinematic viscosity via

$$\mu = \left(\frac{1}{4\lambda} - \frac{1}{8}\right) \rho \frac{\delta l^2}{\delta t}$$

This gives the possibility to make the viscosity arbitrarily small, so that simulations can be performed also at Reynolds numbers higher than 100.

B. The Lattice Bhatnagar–Gross–Krook Model

In the linearized LB equation Eq. (7), the ensemble averaged effect of the particle–particle collision is now represented by a relaxation of the distribution function f_i to the equilibrium function f_i^{eq}, where the matrix L_{ij} does not necessarily have to correspond to an existing set of collision rules. The question now arises if L can be simplified even further to the form $L_{ij} = a\delta_{ij}$, so that the LB equation takes the form (with $\tau = -\delta t/a$)

$$f_i(\mathbf{r} + \mathbf{c}_i\delta t, \ t + \delta t) = f_i(\mathbf{r}, t) - \frac{\delta t}{\tau}(f_i(\mathbf{r}, t) - f_i^{\mathrm{eq}}(\mathbf{r}, t)) \tag{9}$$

At first sight this does not seem possible because the specific form of L, for instance Eq. (8), which followed from the requirement of symmetry. However, it turns out that b, c, and d can be put to zero, if an equilibrium function f_i^{eq} with different weights is used for the different directions, so that the lack of symmetry can be remedied (Qian *et al.*, 1992; Ladd, 1994; Succi, 2001). Specifically, the f_i^{eq} should take the form

$$f_i^{\mathrm{eq}} = a^{ci}\rho \left[1 + \frac{\mathbf{c}_i \cdot \mathbf{u}}{c_s^2} + \frac{(\mathbf{c}_i \cdot \mathbf{u})^2}{2c_s^4} - \frac{u^2}{2c_s^2}\right] \tag{10}$$

where the weight a^{c_i} only depends on the magnitude c_i of the velocity $\mathbf{c}_i$ connected to the link direction i, and c_s is the speed of sound. For the popular D3Q19 model (3D, 19 velocities), there are 6 velocities with $c_i = 1\delta l/\delta t$, 12 velocities with $c_i = \sqrt{2}\delta l/\delta t$, and one zero velocity, $c_i = 0$ (see Fig. 6). The parameters that yield the proper equilibrium distribution in Eq. (10) are $a^0 = 1/3$, $a^1 = 1/36$, and $a^{\sqrt{2}} = 1/18$, and the speed of sound is usually set to $c_s = 1/3(\delta l/\delta t)$ (Ladd and Verberg, 2001; Succi, 2001).

To first order, expression in Eq. (9) represents the finite difference form of the well-known BGK equation:

$$\left(\frac{\partial}{\partial t} + \nabla \cdot \mathbf{c}_i\right) f_i = -\frac{1}{\tau}\left[f_i - f_i^{\mathrm{eq}}\right] \tag{11}$$

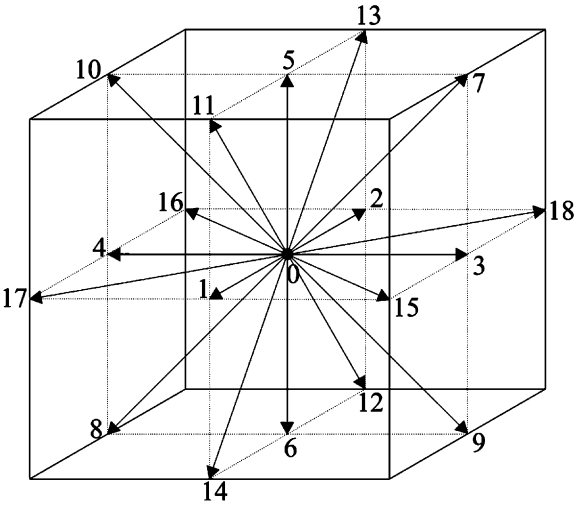

FIG. 6. The D3Q19 model.

It can be shown that this equation will yield the familiar conservation of mass and momentum equations

$$\frac{\partial}{\partial t}\rho + \nabla\cdot(\rho\mathbf{u}) = 0, \quad \frac{\partial}{\partial t}(\rho\mathbf{u}) + \nabla\cdot(\rho\mathbf{u}\mathbf{u}) = -\nabla\cdot\bar{\mathbf{p}} \tag{12}$$

where the pressure tensor is equal to

$$\bar{\mathbf{p}} = p\bar{\mathbf{I}} - \mu\left[(\nabla\mathbf{u}) + (\nabla\mathbf{u})^T\right] - \left(\lambda - \frac{2}{3}\mu\right)\ \left[(\nabla\cdot\mathbf{u}_s)\ \bar{\mathbf{I}}\right]$$

with $\bar{\mathbf{I}}$ the unit tensor, $(\nabla \mathrm{u})_{\alpha\beta} = \nabla_\alpha u_\beta$, $(\nabla u)^T_{\alpha\beta} = \nabla_\beta \mathrm{u}_\alpha$, and the pressure p, shear viscosity μ, and bulk viscosity λ given by

$$p = c_s^2\rho, \quad \mu = \tau c_s^2\rho, \quad \lambda = 0 \tag{13}$$

As said, the lattice BGK in Eq. (9) is the finite difference version of Eq. (11) to first order in δt. To *second* order in δt, however, Eq. (9) represents the finite difference version of a slightly different expression:

$$\left(\frac{\partial}{\partial t} + \nabla\cdot\mathbf{c}_i\right)f_i = -\frac{1}{\tau}\left[f_i - f_i^{\mathrm{eq}}\right] + \frac{\delta t}{2\tau}\left(\frac{\partial}{\partial t} + \nabla\cdot\mathbf{c}_i\right)\left[f_i - f_i^{\mathrm{eq}}\right] \tag{14}$$

In the route to Navier–Stokes, it turns out that f_i^{eq} in the second term on the right-hand side (RHS) does not play a role, so that we can rewrite Eq. (14) as a normal BKG equation with a different prefactor on the RHS:

$$\left(\frac{\partial}{\partial t} + \nabla\cdot\mathbf{c}_i\right)\ f_i = -\frac{\delta t}{\tau - \delta t/2}\left[f_i - f_i^{\mathrm{eq}}\right]$$

We thus find that the lattice BGK model describes, to second order in δt, the fluid according to the Navier–Stokes equation with a viscosity

$$\mu = \left(\tau - \frac{1}{2}\delta t\right)c_s^2\rho$$

where the extra term $-(1/2)\delta t$ is due to the finite difference scheme. As a demonstration of how well the simple lattice BGK scheme in Eq. (9) can describe fluid flow, we show in Fig. 7 the velocity profile from a lattice BGK simulation for forced Poiseuille flow and shear flow; it can be seen that excellent agreement is found with the theoretical results that follow from the Navier–Stokes equation. Note that for the simulations shown in Fig. 7 we used stick-boundary

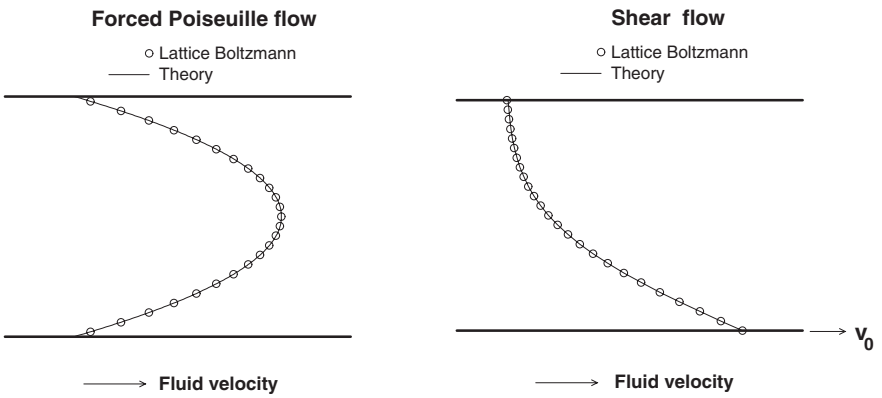

FIG. 7. Velocity profile for Poiseuille flow and shear flow. The points are the LBM data, and the solid lines are the theoretical profiles. For the simulations, we used the D3Q18 model with 25 lattice sites across the channel.

conditions at the walls of the channel. The implementation of such conditions is similar to the boundary conditions that are required to model large, solid objects in the LB model, which is described in Section II.C.

C. Modeling Solid Particles

In order to simulate large, moving particles in the LB model, we should define additional rules that describe the interaction of the LB gas with the surface of the solid particles. One essential ingredient of the moving-boundary rules is that these rules result, on average, in a dissipative force on the suspended particle. An obvious choice of rules is those according to which the gas next to the solid particle moves with the local velocity of the surface of the solid particle. In this way, one models the hydrodynamic "stick" boundary condition; for a spherical particle suspended in an infinite 3D system, moving with velocity $\mathbf{v}$, this will give rise to a frictional force on the particle $\mathbf{F} = 3\pi\mu d\mathbf{v}$, at least in the limit of low Reynolds numbers $Re = \rho d\mathbf{v}/\mu$, where d is the hydrodynamic diameter of the particle and μ is the shear viscosity. A particular efficient and simple way to enforce stick-boundary rules was introduced by Ladd (1994). First the boundary nodes are identified, which are defined as the points halfway two lattice sites that are inside and outside the particle and closest to the actual surface (see Fig. 8, left graph, solid squares). For a static particle, the boundary rule is simply that a distribution moving such that it would cross the boundary is "bounced back" at the boundary node. Since this node is halfway the link, the bounce-back rule has the effect so (see Fig. 8):

$$f_i(\mathbf{r}, t + \delta t) = f_{i'}(\mathbf{r}, t) \tag{15}$$

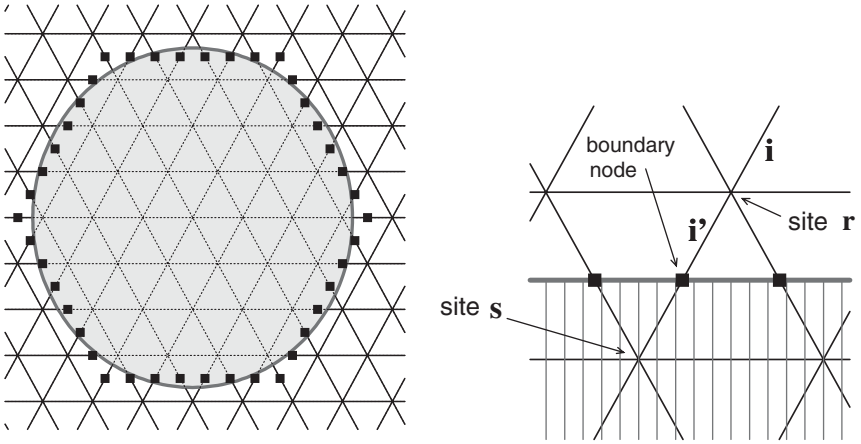

FIG. 8. Left graph: example of a boundary node map for a disc in a 2D hexagonal lattice. Right graph: illustration of the bounce-back rule on an enlarged section of the boundary. The distribution at site r that moves at time t into direction i', instead of arriving at the (virtual) site **s**, is bounced at the boundary node, and thus arrives back at site r at time $t+\delta t$, but is now headed in the opposite direction i.

where i and i' are opposite links. This rule ensures that the fluid velocity at the boundary node indeed vanishes; the momentum at the boundary node at time $t+(1/2)\delta t$ is given by

$$\rho_b \mathbf{u}_b = f_{i'}(\mathbf{r}, t)\, \mathbf{c}_{i'} + f_i(\mathbf{r}, t+\delta t)\, \mathbf{c}_i \tag{16}$$

Inserting Eq. (15) and using $\mathbf{c}_i = -\mathbf{c}_{i'}$ gives $\rho_b \mathrm{u}_b = 0$. For nonstatic particles, the local fluid velocity must be set equal to the local boundary velocity $\mathbf{v}_b$. This can be achieved by a simple modification of the bounce-back rule:

$$f_i(\mathbf{r}, t+\delta t) = f_{i'}(\mathbf{r}, t) + \mathbf{a} \cdot \mathbf{c}_i \tag{17}$$

where a is chosen such that $\mathbf{u}_b = \mathbf{v}_b$. Note that only the component of $\mathbf{v}_b$ in the direction of the link can be set in this way. For more details we refer to the papers by Ladd (1994) and Ladd and Verberg (2001). In Fig. 9 (right graph), we show the LBM simulation results for the velocity of a single free-falling sphere in an (effectively) unbounded fluid. As can be seen from Fig. 9, the boundary rule results in a terminal velocity according to the Stokes–Einstein friction force. Note that the actual plateau value of the velocity is slightly smaller than the theoretical prediction. This can be attributed to the fact that the radius of the particle is not well defined because of the irregular shape of boundary–node surface of the sphere. In fact, the free-falling sphere experiment (or a similar experiment with periodic boundary conditions) is used for *calibration* purposes,

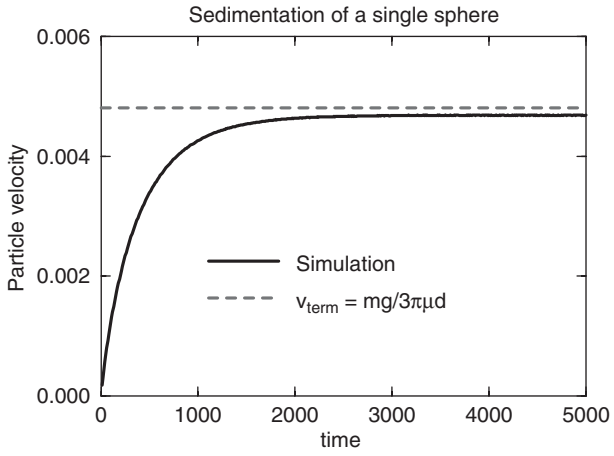

FIG. 9. Velocity of a single sphere in a 3D LB gas. The black line is the data from LBM, which has the proper functional form $v(t) = v_\infty(1 - \exp(-gt/v_\infty))$. The grey line is theoretical terminal velocity, which is slightly higher than v_∞.

i.e., the effective hydrodynamic radius of the spheres is obtained from the terminal velocity, where it is assumed that the Stokes–Einstein relation holds.

D. Results for the Gas–Solid Drag Force

The drag force from the gas phase on an assembly of spheres can, in principle, be obtained from the terminal velocity in a sedimentation experiment. However, the drag force can also be directly measured in the simulation from the change in gas momentum due to the boundary rules. The change in gas momentum per unit time, required to maintain stick-boundary conditions for particle a, is equal to minus the total force $\mathbf{F}_{g\to s,a}$ that the gas phase exerts on particle a. This total force has two contributions (see also Section III.D), namely the drag force $\mathbf{F}_{d,a}$ due the fluid–solid friction at the surface of the spheres and a force $\mathbf{F}_{p,a} = -V_a\nabla p$ due to the static pressure gradient ∇p, which drives the gas flow past the spheres ($V_a = \pi d^3/6$ is the volume of the sphere). From a balance of forces it follows that $V\nabla p = \sum_a \mathrm{F}_{\mathrm{g}\to s,a}$, with V the total volume of the system; eliminating ∇p from the expressions gives $\mathbf{F}_{d,a} = \varepsilon \mathrm{F}_{\mathrm{g}\to s,a}$ with ε the volume fraction of the gas phase. The procedure to obtain the drag force for monodisperse systems in an LB simulation is then as follows. N particles with diameter d are distributed randomly in a box of $n_x \times n_y \times n_z$ lattice sites, so that the gas fraction equals $\varepsilon = 1 - N\pi d^3/(6n_x n_y n_z\ \delta l^3)$. Some typical values are $N = 54$ and $d = 25\delta l$, where periodic boundary conditions are used. All spheres are forced to move with the same constant velocity $\mathbf{v}^{\mathrm{sim}}$ in some arbitrary direction, so that the array of spheres moves as a static configuration through the system. A uniform force is applied to the gas phase, to balance the total force

$-\sum_{a=1}^{N}\mathbf{F}_{g\to s,a}$ from the moving particles on the gas phase. From this it follows that in a frame of reference where the particles are static, the superficial flow velocity is equal to $-\mathbf{v}^{\mathrm{sim}}$, so that $Re = pd|\mathbf{v}^{\mathrm{sim}}|/\mu$, where μ is the viscosity. Once an equilibrium state is obtained, the average value $\bar{\mathbf{F}}_{g\to s} = \langle\sum_{a=1}^{N}\mathbf{F}_{g\to s,a}/N\rangle_t$ is determined, with $\langle\cdot\rangle_t$ a time average. The momentum exchange coefficient β, as defined in Eq. (44), is then determined via

$$\beta = -\frac{\bar{\mathbf{F}}_{g\to \mathrm{s}}(1-\varepsilon)\varepsilon^2}{\mathbf{v}^{\mathrm{sim}}V_{\mathrm{a}}}$$

since the relative velocity $\mathbf{u}$–$\mathbf{v}_a$ in Eq. (44) corresponds to $-\mathbf{v}^{\mathrm{sim}}/\varepsilon$ in the LB simulations and $\mathbf{F}_{d,a} = \varepsilon\mathbf{F}_{\mathrm{g}\to s,a}$. Note that the dimensionless quantity $\beta d^2/\mu$ will only depend on the Reynolds number and the gas fraction ε. Ergun (1952) showed that when the experimental data for β for different ε and Re is plotted in a single $\{\log(x), \log(y)\}$ graph with

$$x = \frac{Re}{1-\varepsilon} \qquad y = \frac{\beta d^2\varepsilon}{\mu(1-\varepsilon)}\frac{1}{Re}$$

all data fall onto a single curve $y = 150/x + 1.75$, which corresponds to

$$\frac{\beta d^2\varepsilon}{\mu(1-\varepsilon)} = 150(1-\varepsilon) + 1.75Re \tag{18}$$

which is the famous Ergun equation. In Fig. 10, we show the data from extensive LB simulations (Van der Hoef *et al.*, 2004; Beetstra *et al.*, 2006) for a range of gas fractions and Reynolds numbers, on the same $\{\log(x), \log(y)\}$ graph. We find that our LBM data deviates substantially from the Ergun equation: for low Re numbers the Ergun equation underestimates the drag force, whereas for high Re numbers the Ergun equation overestimates the drag force. A simple remedy would be to use different coefficients in the Ergun equation, for instance 180 instead of 150 and 1.0 instead of 1.75. However, it can be seen from Fig. 10 that not all data obey the functional form $y = A/x + B$. Note also that the Ergun equation was derived for packed beds, and is not expected to be valid for high gas fractions; for that range, normally the Wen and Yu Eq. (46) is used. However, we find that this equation significantly underpredicts the drag force at higher Reynolds numbers (see Fig. 10). Based on our data from the LB simulations, we suggest the following new drag-force correlation that we write in the form of an Ergun-type equation (Beetstra *et al.*, 2006; Van der Hoef *et al.*, 2005):

$$\frac{\beta d^2\varepsilon}{\mu(1-\varepsilon)} = A(1-\varepsilon) + BRe \tag{19}$$

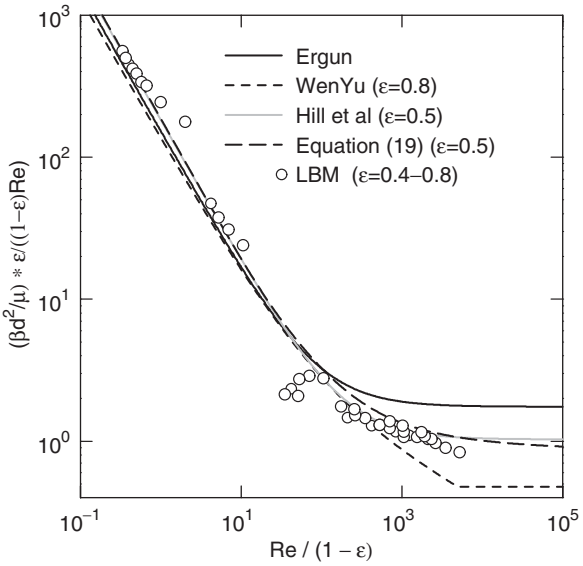

FIG. 10. Normalized drag force at arbitrary Reynolds numbers and gas fractions. The symbols represent the simulation data, the solid line the Ergun correlation Eq. (18), the dashed line the Wen–Yu correlation Eq. (46) for $\varepsilon = 0.8$, and the grey line the correlation by Hill *et al.* (2001a,b) Eq. (47) and the long-dashed line Eq. (19), both for $\varepsilon = 0.5$.

only with coefficients that depend on both ε and Re:

$$A = 180 + \frac{18\varepsilon^4}{1-\varepsilon}\left(1 + 1.5\sqrt{1-\varepsilon}\right)$$

and

$$B = \frac{0.31(\varepsilon^{-1} + 3\varepsilon(1-\varepsilon) + 8.4Re^{-0.343})}{1 + 10^{3(1-\varepsilon)}Re^{2\varepsilon-2.5}}$$

Expression in Eq. (19) is within 8% of all simulation data up to $Re = 1000$. Since this relation has been derived very recently (Beetstra *et al.*, 2006), it has not been applied yet in the higher scale models discussed in Sections III and IV. However, the expression by Hill *et al.* in Eq. (47) derived from similar type of LBM simulations is consistent with our data, in particular when compared to the large deviations with the Ergun and Wen and Yu equations. So, we expect that the simulation results presented in Section IV.F using the Hill *et al.* correlation will not be very different from the results that would be obtained with expression in Eq. (19). A more detailed account of the derivation of expression in Eq. (19) and a comparison with other drag-force relations can be found in Ref. Beetstra *et al.* (2006).

III. Discrete Particle Model

A. Introduction

DPMs offer a viable tool to study the macroscopic behavior of assemblies of particles and originate from MD methods. Initiated in the 1950s by Alder and Wainwright (1957), MD is by now a well-developed method with thousands of papers published in the open literature on just the technical and numerical aspects. A thorough discussion of MD techniques can be found in the book by Allen and Tildesley (1990), where the details of both numerical algorithms and computational tricks are presented. Also, Frenkel and Smit (1996) provide a comprehensive introduction to the "recipes" of classical MD with emphasis on the physics underlying these methods. Nearly all techniques developed for MD can be directly applied to discrete particles models, except the formulation of particle–particle interactions. Based on the mechanism of particle–particle interaction, a granular system may be modeled either as "hard-spheres" or as "soft-spheres."

1. Hard-Sphere Model

In a hard-sphere system, the trajectories of particles are determined by momentum conserving binary collisions. The interactions between particles are assumed to be pair-wise additive and instantaneous. In the simulation, the collisions are processed one by one according to the order in which the events occur. For not too dense systems, the hard-sphere models are considerably faster than the soft-sphere models. Note that the occurrence of multiple collisions at the same instant cannot be taken into account.

Campbell and Brennen (1985) reported the first hard-sphere discrete particle simulation used to study granular systems. Since then, the hard-sphere models have been applied to study a wide range of complex granular systems. Hoomans *et al.* (1996) used the hard-sphere model, in combination with a CFD approach for the gas-phase conservation equations, to study gas–solid two-phase flows in gas-fluidized beds. By using this model, they studied the effect of particle–particle interaction on bubble formation (Hoomans *et al.*, 1996) and the segregation induced by particle-size differences and density differences (Hoomans *et al.*, 2000). This model has been further used in connection with the kinetic theory of granular dynamics by Goldschmidt *et al.* (2001), high-pressure fluidization by Li and Kuipers (2002), and circulating fluidized beds by Hoomans (2000).

Similar simulations have been carried out by other research groups. Ouyang and Li (1999) developed a slightly different version of this model. Helland *et al.* (1999) recently developed a DPM in which hard-sphere collisions are assumed, but where a time-driven scheme (typically found in the soft-sphere model) is used to locate the collisional particle pair. Effect of the gas turbulence has also

been taken into account in some hard-sphere models by Helland *et al.* (2000), Lun (2000), and Zhou *et al.* (2004).

At high-particle number densities or low coefficients of normal restitution e, the collisions will lead to a dramatical decrease in kinetic energy. This is the so-called inelastic collapse (McNamara and Young, 1992), in which regime the collision frequencies diverge as relative velocities vanish. Clearly in that case, the hard-sphere method becomes useless.

2. *Soft-Sphere Model*

In more complex situations, the particles may interact via short- or long-range forces, and the trajectories are determined by integrating Newtonian equations of motion. The soft-sphere method originally developed by Cundall and Strack (1979) was the first granular dynamics simulation technique published in the open literature. In soft-sphere models, the particles are allowed to overlap slightly and the contact forces are subsequently calculated from the deformation history of the contact using a contact-force scheme. The soft-sphere models allow for multiple particle overlap, although the net contact force is obtained from the addition of all pair-wise interactions. The soft-sphere models are essentially time-driven, where the time step should be carefully chosen in calculating the contact force. The soft-sphere models that can be found in literature mainly differ from each other with respect to the contact-force scheme that is used. A review of various popular schemes for repulsive interparticle forces is presented by Schäfer *et al.* (1996). Walton and Braun (1986) developed a model that uses two different spring constants to model the energy dissipation in the normal and tangential directions. In the force scheme proposed by Langston *et al.* (1994), a continuous potential of an exponential form is used, which contains two unknown parameters: the stiffness of the interaction and an interaction constant.

A 2D soft-sphere approach was first applied to gas-fluidized beds by Tsuji *et al.* (1993), where the linear spring–dashpot model—similar to the one presented by Cundall and Strack (1979)—was employed. Xu and Yu (1997) independently developed a 2D model of a gas-fluidized bed. However in their simulations, a collision detection algorithm that is normally found in hard-sphere simulations was used to determine the first instant of contact precisely. Based on the model developed by Tsuji *et al.* (1993), Iwadate and Horio (1998) incorporated van der Waals forces to simulate fluidization of cohesive particles. Kafui *et al.* (2002) developed a DPM based on the theory of contact mechanics, thereby enabling the collision of the particles to be directly specified in terms of material properties such as friction, elasticity, elasto-plasticity, and auto-adhesion.

It is also interesting to note that soft-sphere models have also been applied to other applications such as gas–particle heat transfer by Li and Mason (2000) and coal combustion by Zhou *et al.* (2003). Clearly, these methods open a new way to study difficult problems in fluidized bed reactors.

3. *Comparison between Hard- and Soft-Sphere Models*

Although both hard- and soft-sphere models have been used in the simulation of granular flow, each has its own characteristics that make them very efficient in some cases, while inefficient in others. The two types of models are compared in Table I. Hard-sphere models use an event-driven scheme because the interaction times are (assumed to be) small compared to the free-flight time of particles, where the progression in physical time depends on the number of collisions that occur. In contrast, in the soft-sphere models a time step that is significantly shorter than the contact time should be used. This directly implies that the computational efficiency of the soft-sphere model (compared to the hard-sphere model) decreases when the ratio of the free-flight time to the contact time increases, which is the case when the system becomes less dense. In the soft-sphere models, a slight deformation of particles is allowed, so that multiple contacts between several pairs of particles are possible, which should never happen in the event-driven models. As mentioned above, a lower coefficient of normal restitution may lead to the inelastic collapse in hard-sphere simulations. Incorporation of cohesive forces, especially the pair-wise forces, is quite straightforward in soft-sphere models. This is because the collisional process in the soft-sphere model is described via the Newtonian equations of motion of individual particles, that is, in terms of forces. In the hard-sphere system, the update is not via forces (since they are, loosely speaking, either zero or infinite), but via a momentum exchange at contact. This means that for short-range forces, such as the cohesive force, a kind of hybrid method for the interaction at close encounters has to be devised, which is not straightforward. In contrast, for systems with different size particles, it is the soft-sphere model that poses some difficulties. In a soft-sphere system using a linear spring–dashpot scheme, the spring stiffness is dependent on the particle size. This means that in principle a different spring stiffness should be used for calculating the contact forces between particles with different sizes, otherwise the computing efficiency will drop substantially.

TABLE I
COMPARISON BETWEEN HARD- AND SOFT-SPHERE MODELS. THE SYMBOLS INDICATE GOOD (++), NORMAL (+), AND NOT SUITABLE (−)

	Hard-sphere	Soft-sphere
Computing efficiency	++	+
Multiple contacts	—	++
Dense systems	—	++
Incorporation of cohesive force	+	++
Energy conservation during collisions	++	+
Multiple particle sizes	++	+

In the following, we focus on the soft-sphere method since this really is the "workhorse" of the DPMs. The reason is that it can in principle handle any situation (dense regimes, multiple contacts), and also additional interaction forces—such as van der Waals or electrostatic forces—are easily incorporated. The main drawback is that it can be less efficient than the hard-sphere model.

B. Particle Dynamics: The Soft-Sphere Model

1. The Equations of Motion

The linear motion of a single spherical particle a with mass m_a and coordinate $\mathbf{r}_\mathrm{a}$ can be described by Newton's equation:

$$m_\mathrm{a}\frac{d^2\mathbf{r}_\mathrm{a}}{dt^2} = \mathbf{F}_{contact,a} + \mathbf{F}_{pp,a} + \mathbf{F}_{ext,a} \tag{20}$$

where the RHS is the total force on the particle, which has three basic contributions:

(i) The total contact force $\mathbf{F}_{contact,a}$ is the sum of the individual contact forces exerted by all other particles in contact with the particle a, which are naturally divided into a normal and a tangential component:

$$\mathbf{F}_{contact,a} = \sum_{b\in contactlist} (\mathbf{F}_{ab,n} + \mathbf{F}_{ab,t})$$

(ii) The total external force $\mathbf{F}_{ext,a}$:

$$\mathbf{F}_{ext,a} = \mathbf{F}_{g,\mathrm{a}} + \mathbf{F}_{d,\mathrm{a}} + \mathbf{F}_{p,\mathrm{a}}$$

which includes the gravitational force $\mathbf{F}_{\mathrm{g},a} = m_a g$, and forces exerted by the surrounding gas phase: the drag force $\mathbf{F}_{d,a}$ and a force $\mathbf{F}_{p,a}$ from the pressure gradient.

(iii) The sum of all other particle–particle forces $\mathbf{F}_{pp,a}$ that can include short-range cohesive forces $\mathbf{F}_{coh,a}$, which follow from the van der Waals interaction between the molecules that the particles are made up of, as well as long-range electrostatic forces. In this chapter, we will only consider the cohesive forces.

Note that for *liquid*–solid systems, Eq. (20) should also include the short-range lubrication forces and the effects of other forces such as the "virtual mass" force. But this is beyond the scope of this chapter.

Finally, the rotational motion of particle a is given by

$$I_a\frac{d\omega_a}{dt} = \mathbf{T}_a \tag{21}$$

where I_a is moment of inertia, ω_a the angular velocity, and $\mathbf{T}_a$ the torque, which depends only on the tangential component of the individual contact forces:

$$\mathbf{T}_a = \sum_{b \in contactlist} (R_a \mathbf{n}_{ab} \times \mathbf{F}_{ab,t})$$

with R_a as the radius of particle a.

We will next give a more detailed description of the contact force, the cohesive force, and the integration of the equations of motion—Eqs. (20) and (21). The description of the forces resulting from interaction with the gas phase is given in Section III.D, whereas the dynamics of the gas phase itself is described in Section III.C.

2. *Contact Force*

The calculation of the contact force between two particles is actually quite involved. A detailed model for accurately computing contact forces involves complicated contact mechanics (Johnson, 1985), the implementation of which is extremely cumbersome. Many simplified models have therefore been proposed, which use an approximate formulation of the interparticle contact force. The simplest one was originally proposed by Cundall and Strack (1979), where a linear-spring and dashpot model is employed to calculate the contact forces (see Fig. 11 and 12). In this model, the normal component of the contact force between two particles a and b can be calculated by

$$\mathbf{F}_{ab,n} = -k_n \delta_n \mathbf{n}_{ab} - \eta_n \mathbf{v}_{ab,n} \tag{22}$$

where k_n is the normal spring stiffness, $\mathbf{n}_{ab}$ the normal unit vector, η_n the normal damping coefficient, and $\mathbf{v}_{ab,n}$ the normal relative velocity. The overlap δ_n is given by

$$\delta_n = (R_b + R_a) - |\mathbf{r}_b - \mathbf{r}_a|$$

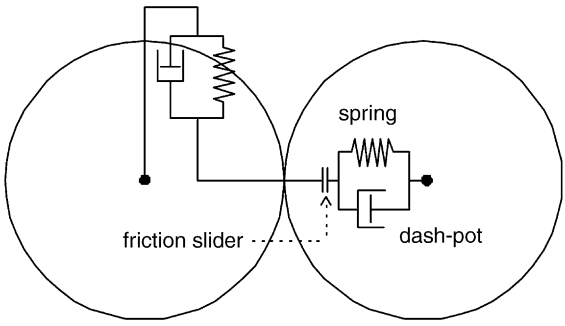

FIG. 11. Graphical representation of the linear spring–dashpot soft-sphere model. From Hoomans, Ph.D. thesis, University of Twente (2000).

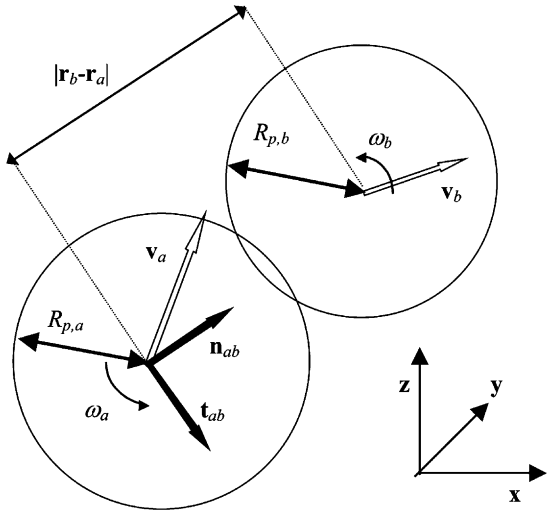

FIG. 12. The coordinate system used in the soft-sphere model.

with R_a and R_b denoting the radii of the particles. The normal unit vector is defined as

$$\mathbf{n}_{ab} = \frac{\mathbf{r}_b - \mathbf{r}_a}{|\mathbf{r}_b - \mathbf{r}_a|} \tag{23}$$

The relative velocity of particles a and b is

$$\mathbf{v}_{ab} = (\mathbf{v}_a - \mathbf{v}_b) + (R_a\omega_a + R_b\omega_b) \times \mathbf{n}_{ab} \tag{24}$$

where $\mathbf{v}_a$ and $\mathbf{v}_b$ are the particle velocities, and ω_a and ω_b the angular velocities. The normal component of the relative velocity between particle a and b is

$$\mathbf{v}_{ab,n} = (\mathbf{v}_{ab} \cdot \mathbf{n}_{ab})\mathbf{n}_{ab} \tag{25}$$

For the tangential component of the contact force, a Coulomb-type friction law is used:

$$\mathbf{F}_{ab,t} = \begin{cases} -k_t\boldsymbol{\delta}_t - \eta_t\mathbf{v}_{ab,t} & \text{for } |\mathbf{F}_{ab,t}| \le \mu_f|\mathbf{F}_{ab,n}| \\ -\mu_f\ |\mathbf{F}_{ab,n}|\mathbf{t}_{ab} & \text{for } |\mathbf{F}_{ab,t}| > \mu_f|\mathbf{F}_{ab,n}| \end{cases} \tag{26}$$

where k_t, $\boldsymbol{\delta}_t$, η_t, and μ_f are the tangential spring stiffness, tangential displacement, tangential damping coefficient, and friction coefficient, respectively. In

Eq. (26), the tangential relative velocity $\mathbf{v}_{ab,t}$, and tangential unit vector $\mathbf{t}_{ab}$ are defined as

$$\mathbf{v}_{ab,t} = \mathbf{v}_{ab} - \mathbf{v}_{ab,n} \qquad \mathbf{t}_{ab} = \frac{\mathbf{v}_{ab,t}}{|\mathbf{v}_{ab,t}|}$$

The calculation of the tangential displacement $\boldsymbol{\delta}_t$ requires some special attention and will be addresses in Section III.B.3.

3. *Tangential Displacement*

Suppose that the tangential displacement at t_o is equal to $\boldsymbol{\delta}_{t_0}$; then one would expect that the displacement $\boldsymbol{\delta}_t$ at time t follows by simply integrating the tangential velocity (Hoomans, 2000):

$$\boldsymbol{\delta}_t = \boldsymbol{\delta}_{t_0} + \int_{t_0}^{t} \mathbf{v}_{ab,t} \; \mathrm{d}t$$

This expression, however, is only justified for 2D systems, where the particles are represented essentially by disks, which are confined in a single plane and the particle–particle contact occurs along a line, as shown in Fig. 13. So, the tangential component of the relative velocity is always in the same plane and no coordinate transformation is required.

In a 3D system, however, it becomes more complicated. The particle–particle contact now occurs in a plane. The tangential component of the relative velocity is always in this plane and vertical to the normal unit vector according to the definition. Since the normal unit vector is not necessarily situated in the same plane at any time, it is desirable to transfer the old tangential displacement to the new contact plane before we calculate the new tangential displacement. To this end, a 3D rotation of the old tangential displacement should be applied. As

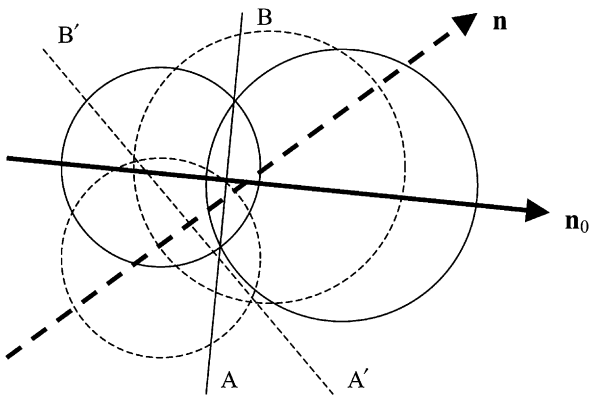

FIG. 13. The rotation of the contact plane during particle–particle collisions.

the tangential velocity vector is always vertical to the normal unit vector, the 3D rotation can be done around the vector determined by $\mathbf{n}_{\mathrm{ab}} \times \mathbf{n}_{0,\mathrm{ab}}$, as shown in Fig. 14. So in a 3D situation, the tangential displacement is determined by

$$\boldsymbol{\delta}_t = \boldsymbol{\delta}_{t_0} \cdot \mathbf{H} + \int_{t_0}^{t} \mathbf{v}_{ab,t} \mathrm{d}t \tag{27}$$

where the rotation matrix is

$$\mathrm{H} = \begin{pmatrix} qh_x^2 + c & qh_x h_y - sh_z & qh_x h_z + sh_y \\ qh_x h_y + sh_z & qh_y^2 + c & qh_y h_z - sh_x \\ qh_x h_z - sh_y & qh_y h_z + sh_x & qh_z^2 + c \end{pmatrix} \tag{28}$$

with $\mathbf{h}$, c, s, and q are defined as

$$\mathbf{h} = \frac{\mathbf{n}_{ab} \times \mathbf{n}_{0,ab}}{\left|\mathbf{n}_{ab} \times \mathbf{n}_{0,ab}\right|}, \quad c = \cos\varphi, \quad s = \sin\varphi, \quad q = 1 - c$$

and

$$\varphi = \arcsin\left(\left|\mathbf{n}_{ab} \times \mathbf{n}_{0,ab}\right|\right)$$

Are Eqs. (27) and (28) sufficient to describe the tangential displacement during particle–particle contact? In the absence of friction, the answer is yes. When we consider friction during particle–particle contact—as pointed out by Brendel

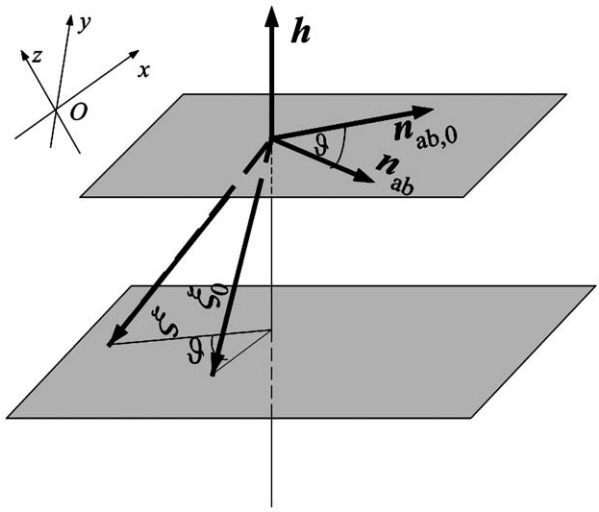

FIG. 14. The transformation of tangential displacement vector.

and Dippel (1998)—the use of Eqs. (27) and (28) may give rise to unphysical behavior for dense systems due to the allowance of an arbitrarily large tangential displacement (Eq. 28). In a dilute system, this will not be a problem since the multiple-particle contacts do not happen frequently. In this case if the contacts ends, the tangential displacements will be set to zero. In contrast for dense systems, multiple-particle contacts are very common and the contact history for a specific particle could be very long. The long contact history causes a relatively large tangential displacement, which means that an extra friction force should be taken into account. This problem can be overcome, however, by using the method proposed by Brendel and Dippel (1998), where the tangential displacement during the friction is calculated by $\boldsymbol{\delta}_{\mathrm{t}} = \mu_{\mathrm{f}}|\mathbf{F}_{\mathrm{ab,n}}|\mathbf{t}_{\mathrm{ab}}/k_{\mathrm{t}}$, so that

$$\boldsymbol{\delta}_t = \begin{cases} \boldsymbol{\delta}_{t_0} \cdot \mathbf{H} + \int_{t_0}^{t} \mathbf{v}_{ab,t}\ \mathrm{d}t & \text{for } \left|\mathbf{F}_{ab,t}\right| \le \mu_f \left|\mathbf{F}_{ab,n}\right| \\ \mu_f \left|\mathbf{F}_{ab,n}\right| \mathbf{t}_{ab}/k_{\mathrm{t}} & \text{for } \left|\mathbf{F}_{ab,t}\right| > \mu_f \left|\mathbf{F}_{ab,n}\right| \end{cases} \tag{29}$$

4. Collision Parameters

To solve the Eqs. (20) and (21), we have to specify five parameters: normal and tangential spring stiffness k_n and k_t, normal and tangential damping coefficient η_n and η_t, and the friction coefficient μ_f . In order to get a better insight into how these parameters are related, it is useful to consider the equation of motion for the overlap in the normal direction δn:

$$m_{eff}\ddot{\delta}_n = -k_n\delta_n - \eta_n\dot{\delta}_n \tag{30}$$

which follows from Eq. (20) when only the normal contact force is taken into account. In Eq. (30), m_{eff} is the reduced mass of the two interacting particles a and b:

$$\frac{1}{m_{\mathrm{eff}}} = \frac{1}{m_{\mathrm{a}}} + \frac{1}{m_{\mathrm{b}}}$$

Equation (30) is the well-known differential equation of the damped harmonic oscillator, the solution of which is

$$\delta_{\mathrm{n}}(t) = (v_0/\Omega)\ \exp(-\Psi t)\ \sin(\Omega t) \tag{31}$$

$$\dot{\delta}_{\mathrm{n}}(t) = (v_0/\Omega)\exp(-\Psi t)(-\Psi \sin(\Omega t) + \Omega\cos(\Omega t)) \tag{32}$$

with $v_0 = \dot{\delta}_n(0)$ as the initial relative velocity, and

$$\Omega = \sqrt{\Omega_0^2 - \Psi^2} \quad \Omega_0 = \sqrt{k_{\mathrm{n}}/m_{\mathrm{eff}}} \quad \Psi = \eta_{\mathrm{n}}/(2m_{\mathrm{eff}})$$

The duration of a contact can be determined from $\delta_n(t_{contact,n}) = 0$, which gives $t_{contact,n} = \pi/\Omega$, so that the relative velocity just after contact equals

$$\dot{\delta}_n(t_{contact,n}) = -v_0 \exp(-\Psi t_{contact,n})$$

According to the definition, the coefficient of normal restitution is given by

$$e = -\frac{\dot{\delta}_n(t_{contact,n})}{\dot{\delta}_n(0)} = \exp(-\pi\Psi/\Omega) \tag{33}$$

Thus, we can calculate the normal damping coefficient via

$$\eta_n = \frac{-2\ln e\sqrt{m_{\text{eff}}k_n}}{\sqrt{\pi^2 + \ln^2 e}} \qquad (e \neq 0)$$

Note that for $e = 0$ we get $\Omega = 0$ according to Eq. (33), so that in that case $\eta_n = 2\sqrt{k_n m_{\text{eff}}}$.

We can follow a similar procedure for the tangential spring–dashpot system. So, the tangential damping coefficient is determined by

$$\eta_t = \frac{-2\ln e_t\sqrt{m'_{\text{eff}}k_t}}{\sqrt{\pi^2 + \ln^2 e_t}} \qquad (e_t \neq 0)$$

where $m'_{\text{eff}} = 2\, m_{\text{eff}}/7$ is the reduced mass of the two-particle system interaction via a tangential linear spring. Note that m'_{eff} is different from m_{eff}, since in a tangential direction both the rotational and translational momentum must be considered. In the case of particle–wall contact, we shall simply treat particle b as a big particle with an infinite radius, so that we have

$$m_{\text{eff}} = m_a \quad m'_{\text{eff}} = \frac{2}{7}m_a$$

The contact force between two particles is now determined by only five parameters: normal and tangential spring stiffness k_n and k_t, the coefficient of normal and tangential restitution e and e_t, and the friction coefficient μ_f. In principle, k_n and k_t are related to the Young modulus and Poisson ratio of the solid material; however, in practice their value must be chosen much smaller, otherwise the time step of the integration needs to become impractically small. The values for k_n and k_t are thus mainly determined by computational efficiency and not by the material properties. More on this point is given in the Section III.B.7 on efficiency issues. So, finally we are left with three collision parameters e, e_t, and μ_f, which are typical for the type of particle to be modeled.

5. Cohesive Force

Cohesion between particles can arise from a variety of sources including van der Waals forces, liquid bridging (i.e., capillary forces), sintering, and so on. Of these forces, which become increasingly important as the particle size decreases, the van der Waals force is generally accepted as the dominating cohesive force in gas-fluidized beds of fine particles (Geldart A and C particles), and will be considered next. The van der Waals force is present between any two molecules (polar or nonpolar) and follows from the interaction of the fluctuating dipole moments on the molecules. According to the London theory, the potential energy of two molecules i and j at distance r_{ij}, due to the van der Waals interaction, is equal to $\varphi(r) = -C_6 r_{ij}^{-6}$. The total energy between two macroscopic bodies a and b, made of the same material, then equals:

$$V = -C_6 \sum_{\{i \text{ on a}\}} \sum_{\{j \text{ on b}\}} r_{ij}^{-6} = -C_6 \rho^2 \int_{v_a} \int_{v_b} \mathrm{d}\mathbf{r}_a \mathrm{d}\mathbf{r}_b |\mathbf{r}_a - \mathbf{r}_b|^{-6} \tag{34}$$

where in the last step we replaced $\Sigma_{i \text{ on } a}$ by $\int_{V_a} d\mathrm{r}_a \rho$(and similarly for b), where ρ is the density of the material, which is justified since the number of molecules present in the particles is very large. For two spheres with radii R_a and R_b, where the centers are at position $\mathbf{r}_a$ and $\mathbf{r}_b$, respectively, expression Eq. (34) can be evaluated analytically (Hunter, 1986; Israelachvili, 1991):

$$V(r_{ab}) = \frac{A}{6}\left[\frac{2}{\bar{r}_{ab}^2 - 4} + \frac{2}{\bar{r}_{ab}^2} + \ln\left(\frac{\bar{r}_{ab}^2 - 4}{\bar{r}_{ab}^2}\right)\right]$$

with

$$\bar{r}_{ab}^2 = \frac{r_{ab}^2 - (R_a - R_b)^2}{R_a R_b}, \quad r_{ab} = |\mathbf{r}_b - \mathbf{r}_a|, \quad A = \pi^2 \rho^2 C_6 \tag{35}$$

The parameter A is known as the Hamaker constant. The force on sphere a then follows via

$$\mathbf{F}_{coh,a} = \frac{\partial V(r_{ab})}{\partial r_{ab}} \mathbf{n}_{ab} = \frac{32}{3} \frac{A}{R_a R_b} \frac{r_{ab} \mathbf{n}_{ab}}{\bar{r}_{ab}^4 (\bar{r}_{ab}^2 - 4)^2} \tag{36}$$

with $\mathbf{n}_{\mathrm{ab}}$ defined by Eq. (23). When the spheres are nearly touching ($r_{\mathrm{ab}} \to R_\mathrm{a} + R_\mathrm{b}$), and for $R_\mathrm{a} = R_\mathrm{b} = R$, the force in Eq. (36) can be simplified to

$$\mathbf{F}_{coh,a} = \frac{AR}{12 s_{ab}^2} \mathbf{n}_{ab} \qquad s_{ab} = r_{ab} - 2R$$

Note that Eq. (36) exhibits an apparent numerical singularity in that the van der Waals interaction diverges if the surface distance between two particles approaches zero. In reality, such a situation will never occur because of the

short-range repulsion between particles. In the present model, we have not included such a repulsion; however, we can avoid the numerical singularity by defining a cut-off (maximal) value of the van der Waals force between two spheres. In practice, it is more convenient to use the equivalent cut-off value for the intersurface distance, s_{ab}^0, instead of for the interparticle force.

The Hamaker constant A can, in principle, be determined from the C_6 coefficient characterizing the strength of the van der Waals interaction between two molecules in vacuum. In practice, however, the value for A is also influenced by the dielectric properties of the interstitial medium, as well as the roughness of the surface of the spheres. Reliable estimates from theory are therefore difficult to make, and unfortunately it also proves difficult to directly determine A from experiment. So, establishing a value for A remains the main difficulty in the numerical studies of the effect of cohesive forces, where the value for glass particles is assumed to be somewhere in the range of 10^{-21} joule.

6. *Integrating the Equations of Motion*

In the following section, we only consider the integration of the equation of linear motion Eq. (20); the procedure for the equation of rotational motion, Eq. (21), will be completely analogous. Mathematically, Eq. (20) represents an initial-value ordinary differential equation. The evolution of particle positions and velocities can be traced by using any kind of method for ordinary differential equations. The simplest method is the first-order integrating scheme, which calculates the values at a time $t + \delta t$ from the initial values at time t (which are indicated by the superscript "0") via:

$$\mathbf{v}_a = \mathbf{v}_a^{(0)} + \mathbf{a}_a^{(0)}\delta t, \qquad \mathbf{r}_a = \mathbf{r}_a^{(0)} + \mathbf{v}_a\delta t \tag{37}$$

where $\mathbf{a}_a$ is the acceleration:

$$\mathbf{a}_a = \frac{\mathbf{F}_{contact,a} + \mathbf{F}_{pp,a} + \mathbf{F}_{ext,a}}{m_a} \tag{38}$$

The first-order integration scheme, however, will introduce a drift in the energy; from Eq. (37), we have

$$(\mathbf{v}_a - \mathbf{a}_a^{(0)}\delta t)^2 = (\mathbf{v}_a)^2 + (\mathbf{a}_a^{(0)}\delta t)^2 - (2\mathbf{v}_a \cdot \mathbf{a}_a^{(0)}\delta t) = (\mathbf{v}_a^{(0)})^2$$

so

$$\frac{1}{2}(\mathbf{v}_a)^2 - (\mathbf{v}_a \cdot \mathbf{a}_a^{(0)}\delta t) + \frac{1}{2}a_a^2\delta t^2 = \frac{1}{2}(\mathbf{v}_a^{(0)})^2 \tag{39}$$

The first term on the left of Eq. (39) is the reduced kinetic energy of the particle at time $t + \delta t$, the second term is the work due to all kinds of external forces, and the first term on the right is the reduced kinetic energy at time t. The remaining

term $\mathbf{a}_a^2 \delta t^2/2$ is always positive, and this energy is introduced into the system solely due to the numerical method, for each time step.

In the past decades, a large number of methods have been proposed to achieve better energy conservation: for example, the Gear family of algorithms and the family of Verlet algorithms (Frenkel and Smit, 1996). In our 3D code, we have incorporated yet another type of method developed by Beeman, which has a somewhat better energy conservation than the Verlet algorithm (Frenkel and Smit, 1996). In the Beeman method, the position and velocity of particle a are calculated via

$$\mathbf{r}_a - \mathbf{r}_a^{(0)} + \mathbf{v}_a^{(0)}\delta t + \left(\frac{2}{3}\mathbf{a}_a^{(0)} - \frac{1}{6}\mathbf{a}_a^{(-1)}\right)(\delta t)^2$$
$$\mathbf{v}_a - \mathbf{v}_a^{(0)} + \frac{1}{3}\mathbf{a}_a \delta t + \left(\frac{5}{6}\mathbf{a}_a^{(0)} - \frac{1}{6}\mathbf{a}_a^{(-1)}\right)(\delta t)$$

where the superscript (–1) denotes the values at time t–δt. Note that the Beeman–Verlet algorithm is not self starting, so it requires the storage of the old value of the acceleration $\mathbf{a}^{(-1)}$.

7. *Efficiency Issues: Spring Constants and Neighbor Lists*

To perform simulations of relatively large systems for relatively long times, it is essential to optimize the computational strategy of discrete particle simulations. Obviously, the larger the time step δt, the more efficient the simulation method. For the soft-sphere model, the maximum value for δt is dictated by the duration of a contact. Since there are two different spring–dashpot systems in our current model, it is essential to assume that $t_{contact,n} = t_{contact,t}$, so that

$$\sqrt{\frac{\pi^2 + (\ln e)^2}{k_\mathrm{n}/m_\mathrm{eff}}} = \sqrt{\frac{\pi^2 + (\ln e_\mathrm{t})^2}{k_\mathrm{t}/m'_\mathrm{eff}}}$$

If we further assume that $e = e_\mathrm{t}$, then the relation between the normal and tangential spring stiffness is

$$\frac{k_\mathrm{t}}{k_\mathrm{n}} = \frac{m_\mathrm{eff}}{m'_\mathrm{eff}} = \frac{2}{7}$$

Based on the discussion in previous sections, we can calculate the time step by

$$\delta t = \frac{1}{K_N} t_{contact,n} = \frac{1}{K_N}\sqrt{\frac{\pi^2 + (\ln e)^2}{k_\mathrm{n}/m_\mathrm{eff}}}$$

where K_N is the minimum number of steps during one contact. Our experience is that K_N must not be less than 5, and is normally in the range 15–50. It can thus be seen that a smaller spring stiffness k_n leads to a larger time step, and therefore it is useful to first perform a number of test simulations with different values for k_n. Another issue is the maximum overlap $\delta_{\max}$, which occurs at $\dot{\delta}(t) = 0$. From Eq. (31) it follows that

$$\delta_{\max} = (v_0/\Omega_0)\exp\left[(-\Psi/\Omega)\arcsin(\Omega/\Omega_0)\right]$$

which must typically be less than 1% of the particle diameter.

A second way of speeding up the simulation is the use of neighbor lists and cell list, which was originally developed for MD simulations (Allen and Tildesley, 1990). The neighbor list contains a list of all particles within the cut-off sphere of a particular particle, so that the separations do not need to be calculated at each step, which is shown in Fig. 15. The neighbor list cut-off $s_{\text{cut-off}}$ should be defined with care. A too small cut-off value may result in some neighboring particles to be excluded from the list. In contrast, however, a big cut-off value will greatly reduce the computational efficiency. To speed up the searching for neighbors, the particles in each fluid cell in this research are put into a corresponding list. All neighbors of a particle will then be found either in the cell containing the particle or in an adjacent cell.

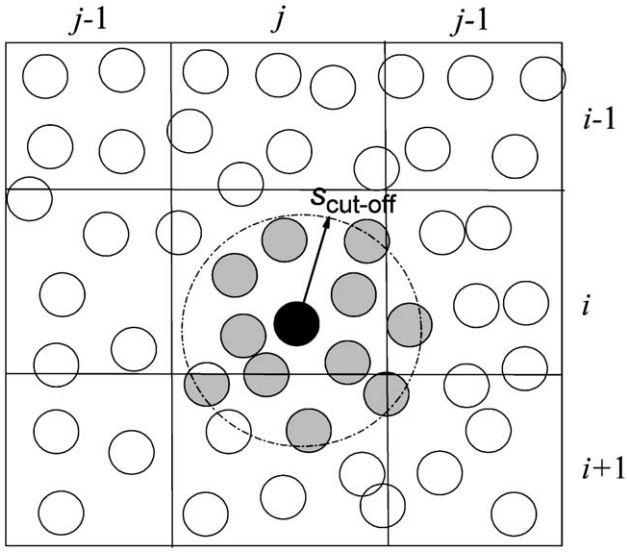

FIG. 15. The scheme of neighbor list and cell lists. The particle of interest is black; the grey particles are within the neighbor list cut-off.

C. Gas Dynamics

In the DPM the gas phase is treated as a continuum phase, the dynamics of which can be described by a set of volume-averaged Navier–Stokes equations (Kuipers *et al.*, 1992). From mass conservation, we have

$$\frac{\partial(\varepsilon\rho)}{\partial t} + \nabla\cdot(\varepsilon\rho\mathbf{u}) = 0 \tag{40}$$

where ρ is the gas density, ε the local porosity, and $\mathbf{u}$ the gas velocity. Momentum conservation gives that

$$\frac{\partial(\varepsilon\rho\mathbf{u})}{\partial t} + \nabla\cdot(\varepsilon\rho\mathbf{u}\mathbf{u}) = -\varepsilon\nabla p - \boldsymbol{S}_{\mathrm{p}} - \nabla\cdot(\varepsilon\bar{\tau}) + \varepsilon\rho\mathbf{g} \tag{41}$$

where p is the gas phase pressure, $\bar{\tau}$ the viscous stress tensor, $\mathbf{g}$ the gravitational acceleration, and $\boldsymbol{S}_{\mathrm{p}}$ a source term that describes the momentum exchange with the solid particles present in the control volume:

$$\boldsymbol{S}_p = \frac{1}{V}\int\sum_{a=1}^{N_{part}}\frac{\beta V_a}{1-\varepsilon}(\mathbf{u}-\mathbf{v}_a)\delta(\mathbf{r}-\mathbf{r}_a)dV \tag{42}$$

Here V represents the local volume of a computational cell and V_a the volume of particle a. The δ-function ensures that the drag force acts as a point force at the (central) position of this particle. In Eq. (42), β is the momentum transfer coefficient, which will be discussed in more detail in Section III.D. The gas phase density ρ is calculated from the ideal gas law:

$$\rho = \frac{pM}{RT}$$

where R is the universal gas constant ($8.314\,\mathrm{J/(mol\cdot K)}$), T the temperature, and M the molecular mass of the gas. The equation of state of the ideal gas can be applied for most gases at ambient temperature and pressure. The viscous stress tensor $\bar{\tau}$ is assumed to depend only on the gas motion. For gas-fluidized beds, the general form for a Newtonian fluid (Bird *et al.*, 1960) can be used:

$$\bar{\tau} = -\left(\lambda - \frac{2}{3}\mu\right)(\nabla\cdot\mathrm{u})\bar{\mathbf{I}} + \mu(\nabla\mathbf{u} + (\nabla\mathbf{u})^T) \tag{43}$$

with λ the gas phase bulk viscosity, μ the gas phase shear viscosity, and $\bar{\mathbf{I}}$ the unit tensor. Normally, the bulk viscosity of the gas phase can be set equal to zero (Bird *et al.*, 1960). Note that no turbulence modeling is taken into

account. For dense gas–solid fluidization, this can be justified since the turbulence is completely suppressed in the particle bed due to the high solids volume fraction.

The numerical method for solving the set of Eqs. (40) and (41) is similar to the method that is used in the TFM, which is discussed in detail in Section IV.E. The time step by which the gas-phase is updated is typically one order of magnitude larger than the time step δt that is used for updating the soft-sphere system. The boundary conditions are taken into account by utilizing fictitious cells at the boundaries and a flag-matrix concept, which allows different boundary conditions to be applied for each single cell. A variety of boundary conditions can be applied by specification of the value of the cell flag $fl(i, j, k)$, which defines the relevant boundary condition for the corresponding cell (i, j, k). A typical set of boundary conditions used in a 2D simulation is shown in Fig. 16.

In Table II, we explain the meaning of each type of boundary condition. Normally, the bottom distributor is defined as influx cells formulated by $fl(i, j, k) = 4$, where the void fraction is set to a constant value of 0.4.

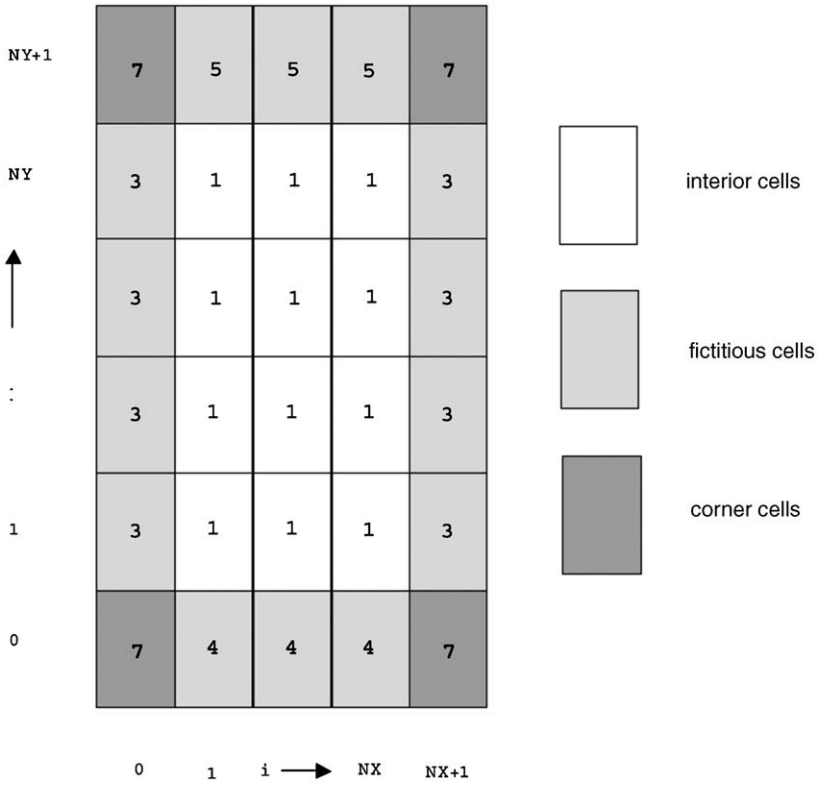

FIG. 16. The typical set of boundary conditions used in 2D simulations.

TABLE II
VALUES FOR THE CELL FLAG, WHICH DEFINE THE BOUNDARY CONDITIONS

fl(*i*, *j*, *k*)	The type of cell
1	Interior cell, no boundary conditions have to be specified
2	Impermeable wall, free-slip boundaries
3	Impermeable wall, no-slip boundaries
4	Influx cell, velocities have to be specified
5	Prescribed pressure cell, free-slip boundaries
6	Continuous outflow cell, free-slip boundaries
7	Corner cell, no boundary conditions have to be specified

D. INTERPHASE COUPLING

For dense gas–solid two-phase flows, a four-way coupling is required; however, the coupling between particles is managed in a natural way in DPMs. The task is, therefore, only to find a two-way coupling between the gas and the solid phases, which satisfies Newton's third law. Basically, the gas phase exerts two forces on particle a: a drag force $\mathbf{F}_{d,a}$ due the fluid–solid friction at the surface of the spheres, and a force $\mathbf{F}_{p,a} = -V_a \nabla p$ due to the pressure gradient ∇p in the gas phase. We will next describe these forces in more detail, along with the procedure to calculate void fraction, which is an essential quantity in the equations for the gas–solid interaction.

1. Drag Force

The drag force that the gas phase exerts on a particle a, consistent with the source term $\mathbf{S}_\mathrm{p}$ in expression Eq. (41), reads

$$\mathbf{F}_{d,a} = \frac{V_a \beta}{1-\varepsilon}(\mathbf{u} - \mathbf{v}_a) \tag{44}$$

where β is the momentum exchange coefficient. The commonly used drag correlations for β in the simulation of gas-fluidized beds are the Ergun (1952) equation for denser beds ($\varepsilon < 0.8$):

$$\frac{\beta d^2 \varepsilon}{\mu(1-\varepsilon)} = 150(1-\varepsilon) + 1.75 Re_a \tag{45}$$

and the Wen and Yu (1966) equation for dilute systems ($\varepsilon > 0.8$):

$$\frac{\beta d^2 \varepsilon}{\mu(1-\varepsilon)} = \frac{3}{4} C_d Re_a \varepsilon^{-1.65} \tag{46}$$

with $Re_a = \rho\varepsilon d_a|\mathbf{u}–\mathbf{v}_a|/\mu$ the Reynolds number of particle a and C_d the drag coefficient, for which the expression by Schiller and Nauman (1935) is used:

$$C_d = \begin{cases} 24(1 + 0.15Re_a^{0.687})/Re_a & Re_a < 10^3 \\ 0.44 & Re_a > 10^3 \end{cases}$$

Note that the validity of both the Ergun and Wen and Yu equations has recently been questioned on the basis of LB data, and alternative drag-force correlations have been proposed. From LB simulations, Hill *et al.* (2001a, b) suggest the following relation for Stokes flow (lim $Re_\mathrm{a} \to 0$):

$$\frac{\beta d^2 \varepsilon}{\mu(1-\varepsilon)} = A_o(1-\varepsilon)$$

with

$$A_o = \begin{cases} 180 & \varepsilon < 0.6 \\ \dfrac{18\varepsilon^3\left(1+\frac{3}{\sqrt{2}}(1-\varepsilon)^{1/2}+\frac{135}{64}(1-\varepsilon)+16.14(1-\varepsilon)\right)}{(1-\varepsilon)+0.681(1-\varepsilon)^2-8.48(1-\varepsilon)^3+8.16(1-\varepsilon)^4} & \varepsilon > 0.6 \end{cases}$$

whereas for $Re_a > 40$, they found that the drag force increases linearly with Re_a:

$$\frac{\beta d^2 \varepsilon}{\mu(1-\varepsilon)} = A_2(1-\varepsilon) + \left[0.6057\varepsilon^3 + 1.908\varepsilon^3(1-\varepsilon) + 0.209\varepsilon^{-2}\right] Re_a \qquad (47)$$

In the paper by Hill *et al.* (2001b), values for A_2 are only given for a finite number of gas fractions[1]; however, A_2 is nearly the same as A_o (Koch and Hill, 2001). Note that in Section II.D we suggest a different expression for β, also on the basis of lattice Boltzmann simulations.

2. *Force from the Pressure Gradient*

The force on particle a due to the pressure gradient ∇p in the gas phase is equal to

$$\mathbf{F}_{p,a} = -V_a \nabla p$$

Note that the reaction of this force (thus the two-way coupling) is incorporated in the momentum conservation equation of the gas phase in the first term on the RHS of Eq. (41). The local value for ∇p at $\mathbf{r}_a$ is obtained from a volume-weighted averaging technique using the values of the pressure gradients at the eight surrounding grid nodes. The volume-weighted averaging technique used to

[1] In Ref. Hill *et al.* (2001b), values are listed for F_2, which relates to A_2 via $F_2 = A_2(1-\varepsilon)/(18\varepsilon^3)$.

obtain the local-averaged value $\bar{Q}$ of a quantity Q_{ijk} from the eight surrounding computational nodes is shown in Fig. 17. The local-averaged value is calculated as follows:

$$\bar{Q} = \frac{Q_1 V_8 + Q_2 V_7 + Q_3 V_6 + Q_4 V_5 + Q_5 V_4 + Q_6 V_3 + Q_7 V_2 + Q_8 V_1}{DX \cdot DY \cdot DZ}$$

where

$$V_1 = \delta_x \delta_y \delta_z \quad V_2 = \tilde{\delta}_x \delta_y \delta_z \quad V_3 = \delta_x \tilde{\delta}_y \delta_z \quad V_4 = \tilde{\delta}_x \tilde{\delta}_y \delta_z$$
$$V_5 = \delta_x \delta_y \tilde{\delta}_z \quad V_6 = \tilde{\delta}_x \delta_y \tilde{\delta}_z \quad V_7 = \delta_x \tilde{\delta}_y \tilde{\delta}_z \quad V_8 = \tilde{\delta}_x \tilde{\delta}_y \tilde{\delta}_z$$

with $\tilde{\delta}_x = DX - \delta x$, $\tilde{\delta}_y = DY - \delta y$, $\tilde{\delta}_z = DZ - \delta z$, and the distances δ_x, δ_y, and δ_z—necessary in this averaging technique—are calculated from the position of the particle in the staggered grid (see also Fig. 24). Note that the same technique of volume weighting is also used to obtain local gas velocities and local void fractions at the position of the center of the particle.

3. *Void Fraction Calculation*

From the position of each particle, we can calculate its contribution to the local solid volume fraction ε_s in any specified fluid cell. This local void fraction, $\varepsilon = 1 - \varepsilon_s$, is one of the key parameters that controls the momentum exchange between the phases and should be determined with care.

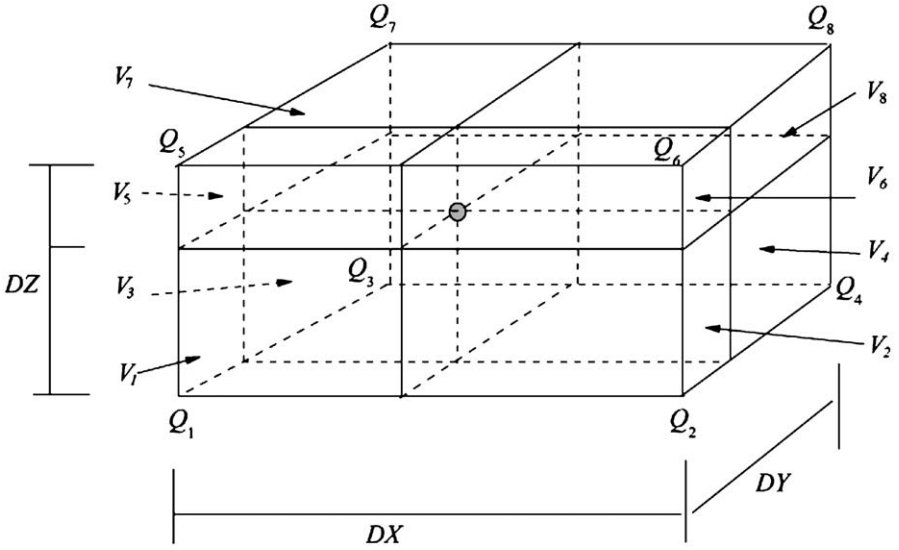

FIG. 17. The scheme of volume-weighted averaging.

For a 2D situation, the void fraction $\varepsilon(i, j)$ can be calculated on the basis of the area occupied by the particles in the cell of interest. A particle can be present in multiple cells, however, as shown in Fig. 18. Hoomans *et al.* (1996) developed a method to account for the multiple cell overlap. The area of $A_{ii,jj}$ is given by

$$\frac{A_{ii,jj}}{R_a^2} = \delta_1\delta_2 - \frac{1}{2}\left[\delta_1\sqrt{1-\delta_1^2} + \delta_2\sqrt{1-\delta_2^2} - \arccos\delta_1 + \arcsin\delta_2\right] \tag{48}$$

and area $A_{i,jj}$ by

$$\frac{A_{i,jj}}{R_a^2} = \frac{1}{2}\pi - \delta_1\delta_2 + \frac{1}{2}\left[\delta_1\sqrt{1-\delta_1^2} + \delta_2\sqrt{1-\delta_2^2} - \arccos\delta_1 + \arccos\delta_2\right] \tag{49}$$

with $\delta_1 = d_1/R_a$ and $\delta_2 = d_2/R_a$ (see Fig. 18). The area $A_{ii,j}$ can be calculated by an equation similar to Eq. (49). However, the void fraction calculated in this way is based on a 2D distribution of disks, whereas the empirical drag-force correlations are derived for 3D systems. To correct for this inconsistency, the void fraction calculated on the basis of area (ε_{2D}) is transformed into a 3D void fraction (ε_{3D}) using the following equation:

$$\varepsilon_{3D} = 1 - \frac{2}{\sqrt{\pi\sqrt{3}}(1-\varepsilon_{2D})^{3/2}}$$

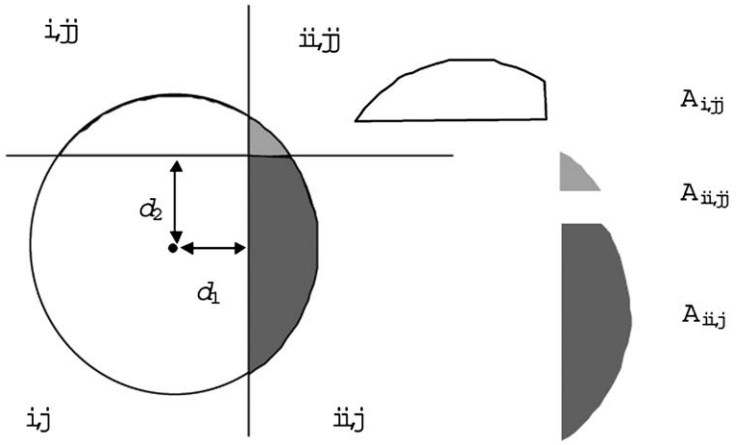

FIG. 18. The multiple cell overlap of a single particle. From Hoomans, Ph.D. thesis, University of Twente (2000).

In a true 3D situation, we can calculate the void fraction on the basis of actual volume of the particles. However, no analytical expression is available for volume $V_{ii,jj}$. Hoomans *et al.* (1996) suggested the approximation

$$V_{ii,jj} \approx \frac{V_{ii}}{V_{\mathrm{a}}}\frac{V_{jj}}{V_{\mathrm{a}}}V_{\mathrm{a}} \tag{50}$$

with $V_{ii} = V_{ii,jj} + V_{ii,j}$ and $V_{jj} = V_{ii,jj} + V_{i,jj}$. The volume of the sphere caps V_{ii} and V_{jj} can be calculated exactly by

$$\frac{V_{ii}}{V_{\mathrm{a}}} = \frac{1}{4}(1-\delta_1)^2(2+\delta_1) \quad \frac{V_{jj}}{V_{\mathrm{a}}} = \frac{1}{4}(1-\delta_2)^2(2+\delta_2)$$

with $\delta_i = d_i/R_a$ being the distance from the center of the particle to the cell boundary relative to the radius of the particle and $V_a = 4\pi {R_a}^3/3$ the volume of the particle. The error in the calculation of the porosity that is introduced by the approximation in Eq. (50) is negligibly small when the particle radii are an order of magnitude smaller than the size of the CFD-grid cell, which is required in any case in order to have a grid-independent value of the porosity. In this context, it is noteworthy that recently a new method has been developed that can generate a grid-independent estimate of ε, even when the size of the particles is of the order of the size of the grid cells (Link *et al.*, 2005).

E. Energy Budget

To relate the discrete particle simulations to the KTGFs, it is very useful to analyze the detailed information of the energy evolution in the system. The total energy balance of the system is obtained by calculating all relevant forms of energy as well as the work performed due to the action of external forces.

- Translational kinetic energy $E_{\mathrm{kin}}^{\mathrm{trans}}$ and rotational kinetic energy $E_{\mathrm{kin}}^{\mathrm{rot}}$

$$E_{\mathrm{kin}}^{\mathrm{trans}} = \frac{1}{2}\sum_{a=1}^{N_{part}} m_a(\mathbf{v}_a \cdot \mathbf{v}_a) \qquad E_{\mathrm{kin}}^{\mathrm{rot}} = \frac{1}{2}\sum_{a=1}^{N_{part}} I_a(\omega_a \cdot \omega_a) \tag{51}$$

- Potential energy from gravity

$$E_p = -\sum_{a=1}^{N_{part}} m_a(\mathbf{g} \cdot \mathbf{r}_a)$$

- Potential energy of the normal spring and tangential spring

$$E_s = \frac{1}{2}\sum_{a=1}^{N_{part}}\sum_{b}(k_n\delta_{ab,n}^2 + k_t\delta_{ab,t}^2)$$

where $b > a$ and $b \in$ the contactlist of a, and $\delta_{ab,n}$, $\delta_{ab,t}$ the overlap and relative tangential displacement, respectively, of particle a and b.

- The work done by the external forces and the cohesive force in one time step δt

$$W_{\text{ext}} = \delta t \sum_{a=1}^{N_{part}} (\mathbf{F}_{d,a} + \mathbf{F}_{p,a} + \mathbf{F}_{coh,a}) \cdot \mathbf{v}_a$$

Also, the energy dissipated during the particle–particle contact process has to be considered and is determined by the following:

- Energy dissipated by the normal and tangential spring in one time step δt

$$E_{ds} = \delta t \sum_{a=1}^{N_{part}} \sum_{b} (\eta_n (\mathbf{v}_{ab,n} \cdot \mathbf{v}_{ab,n}) + \eta_t (\mathbf{v}_{ab,t} \cdot \mathbf{v}_{ab,t}))$$

- Energy dissipated by the friction between particles in one time step δt

$$E_{df} = \delta t \sum_{a=1}^{N_{part}} \sum_{b} (\mu_f |\mathbf{F}_{ab,n}| \mathbf{t}_{ab,n} \cdot \mathbf{v}_{ab,t})$$

where $b > a$ and $b \in$ the contactlist of a.

The total energy of the system is then equal to

$$E_{\text{tot}} = E_p + E_{\text{kin}}^{\text{trans}} + E_{\text{kin}}^{\text{rot}} + E_s + E_{st} - W_{\text{ext}} + E_{ds} + E_{df}$$

F. Results for the Excess Compressibility

In previous work, we have mainly used the DPM model to investigate the effects of the coefficient of normal restitution and the drag force on the formation of bubbles in fluidized beds (Hoomans *et al.*, 1996; Li and Kuipers, 2003, 2005; Bokkers *et al.*, 2004; Van der Hoef *et al.*, 2004), and not so much to obtain information on the constitutive relations that are used in the TFMs. In this section, however, we want to present some recent results from the DPM model on the excess compressibility of the solids phase, which is a key quantity in the constitutive equations as derived from the KTGF (see Section IV.D.). The excess compressibility y can be obtained from the simulation by use of the virial theorem (Allen and Tildesley, 1990).

$$y = \frac{1}{6mN_{\text{part}}\bar{\theta}} \sum_{a} \sum_{b} \mathbf{F}_{ab} \cdot \mathbf{r}_{ab} \tag{52}$$

where the sums are over all particles, with the restriction that $a \neq b$. In Eq. (52), $\mathbf{F}_{ab}$ is the interaction force between particles a and b. For the soft-sphere model

as presented in the previous sections, in the absence of cohesive forces, $\mathbf{F}_{ab}$ is equal to the sum of $\mathbf{F}_{ab,n}$ and $\mathbf{F}_{ab,t}$, as given by Eqs. (26) and (21), and then only when particles a and b are in contact. Furthermore, in Eq. (52), $\bar{\theta}$ is the average granular temperature, which can be defined as the average over the total volume of the local granular temperature defined by Eq. (59). In the absence of any drift velocity, $m\bar{\theta} = 2E_{\mathrm{kin}}^{\mathrm{trans}}/(3N)$, with $E_{\mathrm{kin}}^{\mathrm{trans}}$ as the total translational kinetic energy given by Eq. (51). Note that for the hard-sphere model there are no forces, and a different procedure is required. In that case, the solids pressure (and thus the excess compressibility) can be obtained from the average number of collisions per unit time (Allen and Tildesley, 1990).

We have performed simulations for 500 particles with periodic boundary conditions and no gas phase present. Owing to the inelastic collisions, the particles will continuously dissipate energy, which would eventually cause the particles to come to a quiescent state. In this work, we therefore drive the system by two different techniques: (1) rescaling the particle velocities every time step, according to the desired granular temperature; (2) accelerating the particles randomly. Method (2) is most robust but less efficient. The rescaling procedure, however, does not attain an equilibrium state for high solid fractions. For this reason, the random acceleration procedure is used to simulate the denser system with a solid fraction higher than 0.45, while the rescaling procedure is used for lower solid fractions. For more details on the procedures, we refer to a recent paper (Ye *et al.*, 2005). All the parameters are normalized by the particle radius, particle density, and granular temperature.

First, we should check whether the soft-sphere model gives results comparable to those from the hard-sphere model, since the approximate theories of granular flow are based on the latter model. To this end, we carried out several sets of simulations with particles starting from either random positions or face-centered cubic (FCC) positions. The thermodynamic properties of the hard-sphere system for these two configurations have been well documented by many researchers (Alder and Wainwright, 1957; Carnahan and Starling, 1969; Hoover and Ree, 1969; Erpenbeck and Wood, 1984). In Fig. 19, we show our simulation results for smooth, elastic, and cohesiveless spheres in periodic boundary domains, where at the start of the simulation the particles are placed in an FCC grid. For such systems, Hoover and Ree (1969) observed a phase transition from the fluid state to the solid state at $y = 7.27$. As can be seen, both the hard-sphere and soft-sphere simulations clearly display this transition point. For the fluid state, our simulation data from both models is in very good agreement with the Carnahan–Starling equation of state (Carnahan and Starling, 1969).

$$y^{\mathrm{ES}} = \frac{4\varepsilon_{\mathrm{s}} - 2\varepsilon_{\mathrm{s}}^2}{(1-\varepsilon_{\mathrm{s}})^3} \tag{53}$$

The conclusion is that the soft-sphere model can be used as an alternative for the hard-sphere model, as far as the calculation of the excess compressibility is concerned.

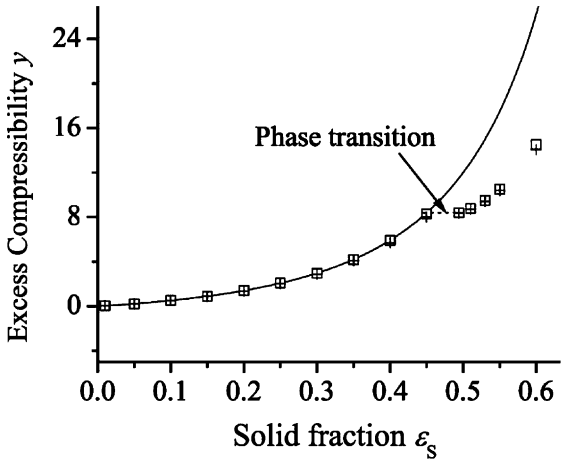

FIG. 19. Simulation results for both the soft-sphere model (squares) and the hard-sphere model (the crosses), compared with the Carnahan–Starling equation (solid-line). At the start of the simulation, the particles are arranged in a FCC configuration. Spring stiffness is $K = 70{,}000$, granular temperature is $\theta = 1.0$, and coefficient of normal restitution is $e = 1.0$. The system is driven by rescaling.

Next, we consider a system of inelastic spheres (ISs). As can be seen from Eq. (81), the KTGF predicts that the excess compressibility y^{IS} of ISs is a linear function of the coefficient of normal restitution e,

$$y^{\mathrm{IS}} = \frac{(1-e)}{2} y^{\mathrm{ES}} \tag{54}$$

where y^{ES} is the excess compressibility of elastic spheres (ESs). In Fig. 20, we show our simulation results for the excess compressibility of ISs, both for the soft-sphere and the hard-sphere model. The solid fraction in the initial configuration is fixed at 0.05. It is shown that for this dilute system, the simulation results of both models are in very good agreement with the prediction in Eq. (54) from the KTGF (solid line). Note that the Eq. (54) is derived under the assumption that the particles are only slightly inelastic, i.e., $e \sim 1.0$.

In Fig. 21, the excess compressibility is shown as a function of the solid fraction for different coefficients of normal restitution e. These results are compared with the Eq. (54), where the excess compressibility y^{ES} is taken from either the Ma–Ahmadi correlation (Ma and Ahmadi, 1986) or the Carnahan–Starling correlation. As can be seen, the excess compressibility agrees well with both correlations for a solid fraction ε_s up to 0.55. For extremely dense systems, i.e., $\varepsilon_s > 0.55$, the Ma–Ahmadi correlation presents a much better estimate of the excess compressibility, which is also the case for purely elastic particles (see Fig. 23).

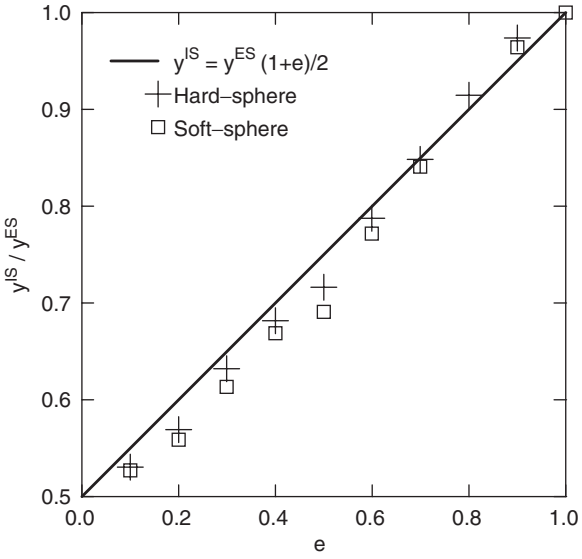

FIG. 20. Excess compressibility y^{IS} for a system of inelastic hard spheres, as function of the coefficient of normal restitution, for one solid fraction ($\varepsilon_s = 0.05$). The excess compressibility has been normalized by the excess compressibility y^{ES} of the elastic hard spheres system. Other simulation parameters are as in Fig. 19.

Up to this point, we have neglected the cohesive van der Waals forces between the particles, which is only justified if particles are larger than say 1 mm. Presently, the van der Waals forces have not been included in the KTGF; a first step would be to consider the effect of such forces on the excess compressibility by also including the interparticle force of Eq. (36) in $\mathbf{F}_{ab}$ of Eq. (52). In Fig. 22, the results for the excess compressibility for different Hamaker constants A are shown. For simplicity, a coefficient of normal restitution $e = 1.0$ is used. We consider two different Hamaker constants: $A = 3.0 \times 10^{-12}$ and $A = 3.0 \times 10^{-10}$ (in units where $\rho_s = 1$, $R = 1$, and $\theta = 1$). From Fig. 22, we see that for these two Hamaker constants, the simulation results differ only slightly from the prediction in Eq. (54), where y^{ES} is calculated from the Ma–Ahmadi correlation, which suggests that cohesion has only a weak influence on the excess compressibility—at least for the values of Hamaker constant that we studied. In this context, it should be noted that the quantification of the cohesive force is not straightforward since there is no reference force (such as gravitational force) in these systems. We consider these systems as slightly cohesive since the ratio of the cohesive potential and the average kinetic energy per particle is small, i.e., $\varphi = 6.25 \times 10^{-8} \sim 6.25 \times 10^{-6}$. At the same time, the ratio between the cohesive force and contact force ranges from 1.11×10^{-5} to 1.11×10^{-3}. If a strong cohesive force is present, particles in the system may form complicated structures, whereas a homogeneous state is one of the basic assumptions underlying

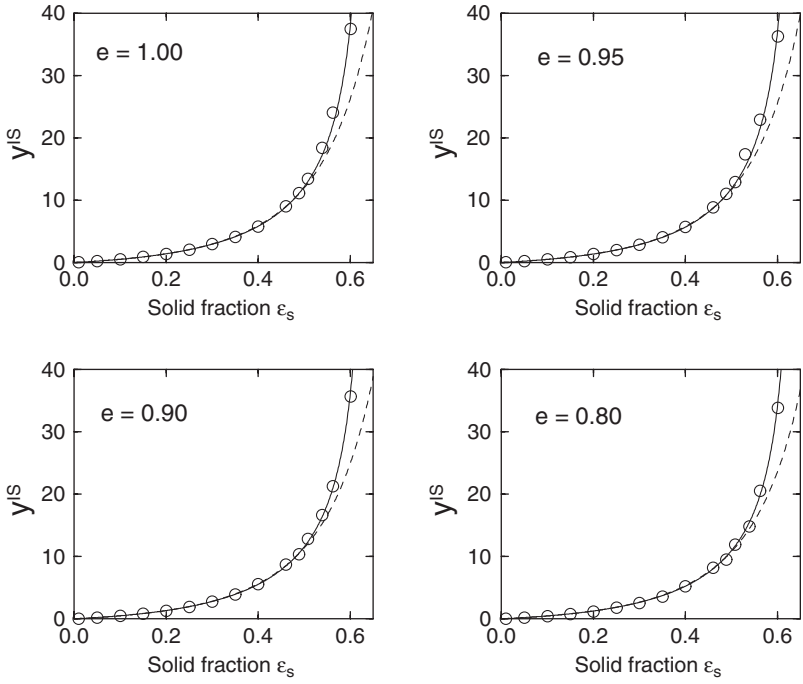

FIG. 21. The excess compressibility from soft-sphere simulations, with random initial particle positions, for different coefficients of normal restitution e: (a) $e = 1.0$ (top-right); (b) $e = 0.95$ (top-left); (c) $e = 0.90$ (bottom-right); (d) $e = 0.80$ (bottom-left). The simulation results (symbols) are compared with Eq. (54) based on the Ma–Ahmadi correlation (solid line) or the Carnahan–Starling correlation (dashed line). The spring stiffness is set to $k_n = 70{,}000$.

the KTGF. A more detailed analysis of the effect of the cohesive force on the excess compressibility can be found in Ref. Ye *et al.* (2005).

IV. Two-Fluid Model

A. Introduction

In the Euler–Euler models, i.e., the TFMs, it is assumed that both the gas and the solid phase are interpenetrating continua. This continuous approach is especially useful and computationally cost-effective when the volume fractions of the phases are comparable, or when the interaction within and between the phases plays a significant role in determining the hydrodynamics of the system. As discussed before, it is relatively straightforward to model the gas phase, for instance by the use of well-established CFD techniques. The challenge is to establish an accurate "hydrodynamic" description of the particulate phase.

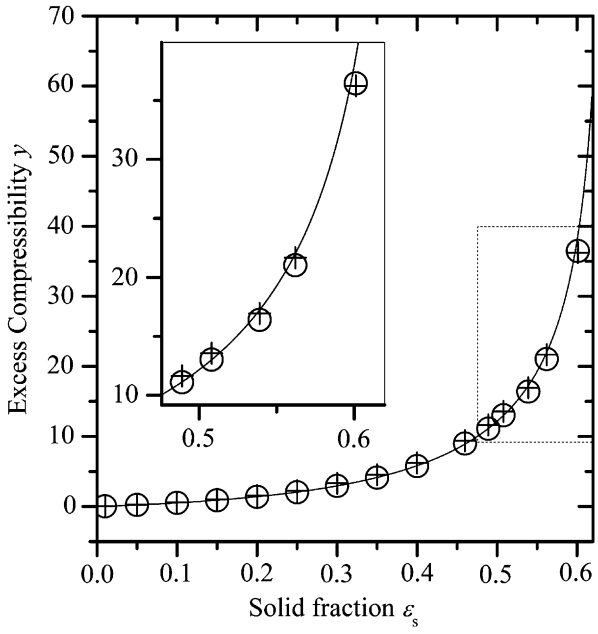

FIG. 22. The effect of the cohesive force on the excess compressibility. The coefficient of normal restitution is $e = 1.0$, and granular temperature is $T = 1.0$. The Hamaker constant is $A = 3.0 \times 10^{-12}$ (circles) and 3.0×10^{-10} (crosses).

Anderson and Jackson (1967, 1968, 1969) and Ishii (1975) have separately derived the governing equations for TFMs from first principles. Although the details of constructing the averaged equations are different, the final equations are essentially the same. The TFMs differ significantly from each other as different closures for the solid stress tensor are used.

There are basically three types of approaches to define the solid stress tensor, or more specifically the solid viscosity. In the early hydrodynamic models—developed by Jackson and his co-workers (Anderson and Jackson, 1967; Anderson *et al.*, 1995), Kuipers *et al.*, (1992), and Tsuo and Gidaspow (1990)—the viscosity is defined as an empirical constant, and also the dependence of the solid phase pressure on the solid volume fraction is determined from experiments. The advantage of this model is its simplicity, the drawback is that it does not take into account the underlying characteristics of the solid phase rheology.

In another class of models, pioneered by Elghobashi and Abou-Arab (1983) and Chen (1985), a particle turbulent viscosity, derived by extending the concept of turbulence from the gas phase to the solid phase, has been used. This is the so-called $k-\varepsilon$ model, where the k corresponds to the granular temperature and ε is a dissipation parameter for which another conservation law is required. By coupling with the gas phase $k-\varepsilon$ turbulence model, Zhou and Huang (1990) developed a $k-\varepsilon$ model for turbulent gas–particle flows. The $k-\varepsilon$ models do not

include the effect of particle–particle collisions, and so these models are restricted to dilute gas–particle flows.

Significant contributions to the modeling of gas–solid flows have been made by Gidaspow and co-workers (1994), who combined the kinetic theory for the granular phase with continuum representations for the particle phase. There are a number of other studies using this approach. Sinclair and Jackson (1989) predicted the core-annular regime for steady developed flow in a riser. Ding *et al.* (1990) simulated a bubbling fluidized bed. Transient simulations and comparisons to data were done by Samuelsberg and Hjertager (1996). Nieuwland *et al.* (1996) investigated a circulating fluidized bed using the KTGF. Detamore *et al.* (2001) have performed an analysis of scale-up of circulating fluidized beds using kinetic theory.

One of the strengths of the KTGF, although still under development, is that it can offer a very clear physical picture with respect to the key parameters (e.g., particle pressure, particle viscosity, and other transport coefficients) that are used in the TFMs. The TFMs based on KTGF requires less *ad hoc* adjustments compared to the other two types of models. Therefore, it is the most promising framework for modeling engineering-scale fluidized beds.

B. Governing Equations

In the TFM, both the gas phase and the solid phase are described as fully interpenetrating continua using a generalized form of the Navier–Stokes equations for interacting fluids. The continuity and momentum equations for the gas phase are given by expressions identical to Eqs. (40) and (41), except for the gas–solid interaction term:

$$\frac{\partial(\varepsilon\rho)}{\partial t} + (\nabla \cdot \varepsilon\rho\mathbf{u}) = 0 \tag{55}$$

$$\frac{\partial(\varepsilon\rho\mathbf{u})}{\partial t} + (\nabla \cdot \varepsilon\rho\mathbf{u}\mathbf{u}) = -\varepsilon\nabla p - \beta(\mathbf{u} - \mathbf{u}_s) - \nabla \cdot (\varepsilon\bar{\tau}) + \varepsilon\rho\mathbf{g} \tag{56}$$

with $\bar{\tau}$ as the viscous stress tensor of the gas phase given by Eq. (43). The continuity and momentum equations for the particle phase are given by a similar set of equations:

$$\frac{\partial(\varepsilon_s\rho_s)}{\partial \mathrm{t}} + (\nabla \cdot \varepsilon_s\rho_s\mathbf{u}_s) = 0 \tag{57}$$

$$\frac{\partial(\varepsilon_s\rho_s\mathbf{u}_s)}{\partial t} + (\nabla \cdot \varepsilon_s\rho_s\mathbf{u}_s\mathbf{u}_s) = -\varepsilon_s\nabla p - \nabla p_s + \beta(\mathbf{u} - \mathbf{u}_s) - \nabla \cdot \bar{\boldsymbol{\tau}}_s + \varepsilon_s\rho_s\mathbf{g} \tag{58}$$

where $\varepsilon_s = 1-\varepsilon$ and $\mathrm{u_s}$ is the velocity of the solid phase. Note that ρ_s is the material density of the solid phase, so that the local mass per unit volume is equal to $\rho_s\varepsilon_s$. Obviously, the numerical scheme for updating the solid phase is now analogous to (and synchronous with) that of the gas phase, the details of

which are given in Section IV.E. Since the concept of particles has disappeared completely in such a modeling, the effect of particle–particle interactions can only be included indirectly, i.e., via the effective solid pressure p_s and the effective solid stress tensor $\bar{\tau}_s$. A description that allows for a more detailed description of particle–particle interactions follows from the KTGF, which expresses the pressure and the solid stress tensor as a function of the local granular temperature θ, which is defined from the fluctuation in the velocity of the individual solid particles. More precisely, the granular temperature at $\mathbf{r}$ is defined as

$$\theta = \frac{1}{3}\left\langle \frac{1}{N_{\mathbf{r}}}\sum_{a=1}^{N_{\mathbf{r}}}(\mathbf{v}_a - \mathbf{u}_s)^2 \right\rangle \tag{59}$$

where $\langle . \rangle$ is an ensemble average, and the sum is over all $N_{\mathbf{r}}$ particles in a small control volume δV around $\mathbf{r}$. Note that also the solid density and velocity as they appear in Eqs. (57) and (58) can be defined from the positions and momenta of the individual particles by similar type of averages[2]:

$$\varepsilon_s\rho_s = \left\langle \frac{1}{\delta V}\sum_{a=1}^{N_{\mathbf{r}}} m_a \right\rangle \quad \varepsilon_s\rho_s\mathbf{u}_s = \left\langle \frac{1}{\delta V}\sum_{a=1}^{N_{\mathbf{r}}} m_a\mathbf{v}_a \right\rangle \tag{60}$$

For particles of equal mass, we thus have $\varepsilon_{\mathrm{s}}\rho_{\mathrm{s}} = mn$ with n the local number density of particles. From the KTGF, the time evolution of the granular temperature is given by

$$\frac{3}{2}\left[\frac{\partial}{\partial t}(\varepsilon_s\rho_s\theta) + \nabla\cdot(\varepsilon_s\rho_s\theta\mathbf{u}_s)\right] = -(p_s\bar{\mathbf{I}} + \bar{\tau}_s) : \nabla\mathbf{u}_{\mathrm{s}} - \nabla\cdot\boldsymbol{q}_s - 3\beta\theta - \gamma \tag{61}$$

with $\mathbf{q}_s$ the kinetic energy flux and γ the dissipation of kinetic energy due to inelastic particle collisions. In Eqs. (58) and (61), there are three unknown quantities (pressure, stress tensor, and energy flux), which must be expressed in terms of the three basic hydrodynamic variables (density, velocity, and temperature), in order to get a closed set of equations. This is the subject of the KTGF, and the resulting closures will be presented in Section IV.D. However, before doing so, we will first give a brief description of the general principles of kinetic theory.

[2]Note that for $\delta V \to 0$ the local density and momentum density can be written as $\varepsilon_{\mathrm{s}}p_{\mathrm{s}} = \sum_a m_a\delta(\mathrm{r}-\mathrm{r}_i)$ and $\varepsilon_{\mathrm{s}}p_{\mathrm{s}}\mathbf{u}_{\mathrm{s}} = \sum_a m_a\mathbf{v}_a\delta\ (\mathrm{r}-\mathrm{r}_i)$, which are the expressions that are usually found in literature.

C. General Kinetic Theory

In this section, we will only discuss the basic principles of kinetic theory, where for detailed derivations we refer to the classic textbook by Chapman and Cowling (1970), and a more recent book by Liboff (1998). Of central importance in the kinetic theory is the single particle distribution function $f_s(\mathbf{r}, \mathbf{v})$, which can be defined as the number density of the solid particles in the 6D coordinate and velocity space. That is, $f_s(\mathbf{r}, \mathbf{v}, t)\, d\mathbf{v}\, d\mathbf{r}$ is the average number of particles to be found in a 6D "volume" $d\mathbf{v}\, d\mathbf{r}$ around $\mathbf{r}, \mathbf{v}$. This means that the local density and velocity of the solid phase in the continuous description are given by

$$\bar{\rho}_s(\mathbf{r}, t) = \int_{-\infty}^{\infty} m f_s(\mathbf{r}, \mathbf{v}, t) d\mathbf{v} \tag{62}$$

and

$$\bar{\rho}_s(\mathbf{r}, t)\mathbf{u}_s(\mathbf{r}, t) = \int_{-\infty}^{\infty} m\mathbf{v} f_s(\mathbf{r}, \mathbf{v}, t) d\mathbf{v} \tag{63}$$

where the local density is defined as $\bar{\rho}_s = \rho_s \varepsilon_s$ with ρ_s as the material density of the solid particles. The *granular temperature*, defined by Eq. (59), follows from

$$\bar{\rho}_s(\mathbf{r}, t)\theta(\mathbf{r}, t) = \frac{1}{3}\int_{-\infty}^{\infty} m(\mathbf{v} - \mathbf{u}_s)^2 f_s(\mathbf{r}, \mathbf{v}, t) d\mathbf{v} \tag{64}$$

The evolution of the one-particle distribution function f_s can be described by the Boltzmann equation

$$\frac{\partial}{\partial t} f_s(\mathbf{r}, \mathbf{v}, t) + \mathbf{v} \cdot \nabla f_s(\mathbf{r}, \mathbf{v}, t) = C \tag{65}$$

which is basically a continuity equation, where the second term on the left-hand side (LHS) represents the change of f_s in time due to streaming and the collision function C on RHS represents the change of f_s due to particle–particle interactions. Conservation of mass, momentum, and energy in a collision gives that C should satisfy

$$\int_{-\infty}^{\infty} C d\mathbf{v} = 0, \quad \int_{-\infty}^{\infty} C\mathbf{v} d\mathbf{v} = 0, \quad \int_{-\infty}^{\infty} C\upsilon^2 d\mathbf{v} = 0$$

Taking the same integrals ($\int \ldots d\mathbf{v}, \int \ldots \mathbf{v} d\mathbf{v}$, and $\int \ldots \upsilon^2 d\mathbf{v}$) of the Boltzmann equation Eq. (65), making use of Eqs. (62) and (63), yields

$$\frac{\partial}{\partial t}\bar{\rho}_s + \nabla \cdot (\bar{\rho}_s \mathbf{u}_s) = 0 \tag{66}$$

$$\frac{\partial}{\partial t}(\bar{\rho}_s \mathbf{u}_s) + \nabla \cdot (\bar{\rho}_s \mathbf{u}_s \mathbf{u}_s) = -\nabla \cdot \bar{\mathbf{p}} \tag{67}$$

$$\frac{3}{2}\left[\frac{\partial}{\partial t}(\bar{\rho}_s \theta) + \nabla \cdot (\bar{\rho}_s \theta \mathbf{u}_s)\right] = -\bar{\mathbf{p}} : \nabla \mathbf{u}_s - \nabla \cdot \mathbf{q}_s \tag{68}$$

with

$$\bar{\mathbf{p}} = \int_{-\infty}^{\infty} m\mathbf{V}\mathbf{V} f_s(\mathbf{r}, \mathbf{v}, t) d\mathbf{v}, \quad \mathbf{q} = \int_{-\infty}^{\infty} \frac{m\mathbf{V}^2}{2} \mathbf{V} f_s(\mathbf{r}, \mathbf{v}, t) d\mathbf{v}, \quad \mathbf{V} = \mathbf{v} - \mathbf{u}_s$$

In principle, one should solve the Boltzmann equation Eq. (65) in order to arrive at explicit expressions for the pressure tensor $\bar{\mathbf{p}}$ and heat flux $\mathbf{q}$, which proves not possible, not even for the simple BGK equation Eq. (11). However, one can arrive at an approximate expression via the Chapman–Enskog expansion, in which the distribution function is expanded about the equilibrium distribution function f_s^{eq}, where the expansion parameter is a measure of the variation of the hydrodynamic fields in time and space. To second order, one arrives at the familiar expression for $\bar{\mathbf{p}}$ and $\mathbf{q}$

$$\bar{\mathbf{p}} = p_s \bar{\mathbf{I}} + \bar{\tau}_s, \quad \mathbf{q}_s = -\kappa_s \nabla \theta \tag{69}$$

with $\bar{\mathbf{I}}$ is the unit tensor, and

$$\bar{\tau}_s = -\mu_s \left[(\nabla \mathbf{u}_s) + (\nabla \mathbf{u}_s)^T\right] - \left(\lambda_s - \frac{2}{3}\mu_s\right)\left[(\nabla \cdot \mathbf{u}_s)\bar{\mathbf{I}}\right] \tag{70}$$

where $(\nabla u)_{\alpha\beta} = \nabla_\alpha u_\beta, (\nabla u)^T_{\alpha\beta} = \nabla_\beta u_\alpha$. Inserting the above expression for $\bar{\mathbf{p}}$ and $\mathbf{q}$ into Eqs. (67) and (68) will give the Navier–Stokes equations, where the parameters κ_s, λ_s, μ_s, and ps can be calculated (at least in princeiple) when the collision function C is known. For the simple BGK equation Eq. (11), this will result in the relations of Eq. (13). For an accurate description of the solid phase, however, one requires a much more detailed expression for C, which contains the details of the particle–particle interactions. Although this is a laborious route, it opens a possibility for making a link between the "microscopic" details of particle collisions and the "macroscopic" transport coefficients. Apart from the details of the particle–particle interactions, C does also depend on the joint probability function $f_{\mathrm{s}}^{(2)}(\mathbf{r}_1, \mathbf{v}_1, \mathbf{r}_2, \mathbf{v}_2, t)$, provided that the interactions between the particles are pair-wise additive (generally for n-body interactions, C will depend on $f_{\mathrm{s}}^{(n)}$). In order to get a closed equation, $f_{\mathrm{s}}^{(2)}$ should be described in term of f_{s}. If the velocities $\mathbf{v}_1$ and $\mathbf{v}_2$ are not correlated, one can write

$$f_s^{(2)}(\mathbf{r}_1, \mathbf{v}_1, \mathbf{r}_2, \mathbf{v}_2, t) = g(r_{12}, \varepsilon_{\mathrm{s}}) f_{\mathrm{s}}(\mathbf{r}_1, \mathbf{v}_1, t) f_s(\mathbf{r}_2, \mathbf{v}_2, t)$$

where $g(r_{12}, \varepsilon_s)$ is the pair distribution function, which depends only on the distance $r_{12} = |\mathbf{r}_2 - \mathbf{r}_1|$ and the solid fraction.

For sufficiently low density, $g = 1$, the collision function takes the form

$$C = \frac{1}{m^2} \int d\Omega \sigma(\Omega) \int d\mathbf{v}'(\mathbf{v} - \mathbf{v}') \left[f_s(\tilde{\mathbf{v}}) f_s(\tilde{\mathbf{v}}') - f_s(\mathbf{v}) f_s(\mathbf{v}') \right] \tag{71}$$

where we have omitted the $\mathbf{r}$, t argument of f_s. In Eq. (71), $\tilde{\mathbf{v}}$, $\tilde{\mathbf{v}}'$, are the velocities of the two particles involved *after* the collision, which can be constructed from the initial velocities $\mathbf{v}$, $\mathbf{v}'$ from conservation of energy and momentum:

$$\tilde{\mathbf{v}} = \mathbf{v} + \boldsymbol{\alpha}(\boldsymbol{\alpha} \cdot (\mathbf{v} - \mathbf{v}')) \qquad \tilde{\mathbf{v}}' = \mathbf{v}' + \boldsymbol{\alpha}(\boldsymbol{\alpha} \cdot (\mathbf{v}' - \mathbf{v}))$$

with $\boldsymbol{\alpha}$ as the unity vector along the line connecting the two centers of the particle before the collision. Furthermore, in Eq. (71), $\sigma(\Omega)$ represents the "cross-section" and Ω is the solid angle in which the particle is scattered. More details on these concepts can be found in the standard literature (Chapman and Cowling, 1970; Liboff, 1998). Using this form of the collision function, it can be shown that pressure p_s, shear viscosity μ_s, and thermal conductivity κ_s in Eqs. (69) and (70) are given by

$$\mu_s^{\mathrm{id}} = \frac{5}{96} \pi \rho_s d \sqrt{\frac{\theta}{\pi}}, \quad \kappa_s^{\mathrm{id}} = \frac{75}{384} \pi \rho_s d \sqrt{\frac{\theta}{\pi}}, \quad p_s^{\mathrm{id}} = \varepsilon_s \rho_s \theta \tag{72}$$

where d is the diameter of the particles, and the superscript id (ideal) indicates that the expressions are for the limit of a dilute gas, for which the pressure is given by the ideal gas law.

For high densities, g cannot be set equal to one, and the collision function becomes much more complex and so is not given here. It turns out, however, that instead of using the full radial distribution function, it is sufficient to use the value at contact $r = R$, so that we define a new function:

$$\chi(\varepsilon_s) = g(R, \varepsilon_s)$$

In the standard Enskog theory (SET), the shear viscosity and thermal conductivity of ESs are found to be equal to[3]

$$\mu_s^{\mathrm{ES}} = \mu_s^{\mathrm{id}} \left(\frac{1}{\chi b \rho_s} + \frac{4}{5} + 0.7614 \chi b \rho_s \right) b \rho_s \tag{73}$$

[3]See Chapman and Cowling (1970). Note that the true expression for μ_s^{ES} reads $\mu_s^{\mathrm{ES}} = c_1 \mu_s^{\mathrm{id}} (\frac{1}{\chi b \rho_s} + \frac{4}{5} + \frac{4}{25}(1 + \frac{12}{\pi c_2}) \chi b \rho_s) b \rho_s$, with $c_1 = c_2 = 1.016$. In most expressions in literature, c_1 is set equal to 1; in expression Eq. (82) of Gidaspow, both $c_1 = c_2 = 1$, which is the cause of the slightly different coefficient 0.771, compared to 0.7614 in Eq. (75). For practical purposes, the difference is negligible. Similar remarks can be made about κ.

$$\kappa_s^{\mathrm{ES}} = \kappa_s^{\mathrm{id}}\left(\frac{1}{\chi b\rho_s} + \frac{6}{5} + 0.7574\chi b\rho_s\right) b\rho_s \tag{74}$$

with $b = 2\varepsilon_s\pi d^3/3\,m$, so that $bp_s = 4\varepsilon_s$. Note that the pressure of a dense system is directly related to the radial distribution function at contact (Chapman and Cowling, 1970; Hansen and McDonald, 1986):

$$p_s^{\mathrm{ES}} = p_s^{\mathrm{id}}(1 + y^{\mathrm{ES}}) \qquad y^{\mathrm{ES}} = \chi b\rho_s = 4\chi\varepsilon_s$$

with y^{ES} the excess compressibility of the elastic hard-sphere system. Thus in the Enskog theory, the transport coefficients are completely determined by the y^{ES}:

$$\mu_s^{\mathrm{ES}} = 4\mu_s^{\mathrm{id}}\varepsilon_s\left(\frac{1}{y^{\mathrm{ES}}} + \frac{4}{5} + 0.7614y^{\mathrm{ES}}\right) \tag{75}$$

$$\kappa_s^{\mathrm{ES}} = 4\kappa_s^{\mathrm{id}}\varepsilon_s\left(\frac{1}{y^{\mathrm{ES}}} + \frac{6}{5} + 0.7574y^{\mathrm{ES}}\right) \tag{76}$$

Various expressions for y^{ES} have been proposed in literature based on the virial coefficients and simulation data. Most of these have the following general form:

$$y^{\mathrm{ES}}(\varepsilon_s) = \frac{\sum_{n=0} c_n(4\varepsilon_s)^{n+1}}{(1 - (\varepsilon_s/\varepsilon_{\mathrm{cp}})^a)^b} \tag{77}$$

with $\varepsilon_{\mathrm{cp}}$ the "close-packed" solid fraction, at which the pressure diverges. In Table III, we summarize the parameters found by different authors. A comparison of expression in Eq. (77) with the MD simulation data from Alder and Wainwright (1960) and Woodcock (1981) is shown in Fig. 23. In our current

TABLE III
VALUES FOR THE PARAMETERS IN EQ. (77)

	CS	MA	SSM	TC
$\varepsilon_{\mathrm{cp}}$	1	0.64356	0.6435	0.6875
a	1	3	1	1
b	3	0.67802	0.76	1
c_o	1	1	1	1
c_1	−1/8	0.625	0.3298	0.2613
c_2	0	0.2869	0.08867	0.05968
c_3	0	0.070554	0.01472	0.005905
c_4	0	0	0.0005396	–0.001191
c_5	0	0	−0.0003574	–0.0004455
c_6	0	0	−0.0005705	–0.0004818
c_7	0	0	–0.0001212	–0.00003636
c_8	0	0	–0.0001151	–0.00008182

Note: CS: Carnahan and Starling (J. Chem. Phys. **51**, 635 (1969)); MA: Ma and Ahmadi (J. Chem. Phys. **84**, 3449 (1986)); SSM: Song, Stratt and Mason (J. Chem. Phys. **88**, 1126 (1988)); TC: Tobochnik and Chapin (J. Chem. Phys. **88**, 5824 (1988)).

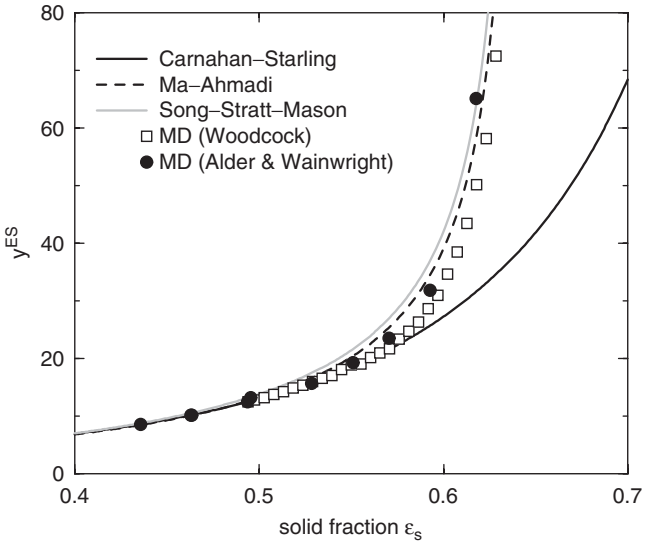

FIG. 23. Comparison of the expressions from Eq. (77) and Table III with data from MD simulations.

version of the TFM, we use the expression by Ma and Ahmadi (1986) (see also Fig. 21). Alder *et al.* (1970) have also measured the shear viscosity in MD simulations of dense hard-sphere systems. It was found that the Enskog approximation in Eq. (75) is very accurate up to $\varepsilon_s = 0.3$; however, for higher solid fractions the theory significantly underestimates the shear viscosity up to a factor of two for $\varepsilon_s \approx 0.5$.

D. Kinetic Theory of Granular Flow

In the KTGF, the dissipation of energy in collisions is included in the Enskog theory. Currently, only the effect of the coefficient of normal restitution has been considered, although it is anticipated that friction also plays an important role. The derivation of the constitutive equations for ISs can be found in the book by Gidaspow (1994) and the papers by Jenkins and Savage (1983), Lun *et al.* (1984), Ding and Gidaspow (1990), and Nieuwland *et al.* (1996). Here, we will present the expressions for p_s, μ_s, and K_s from the book of Gidaspow (1994) (Eqs. (T.9.1), (9.183), (9.250), (9.262), (9.268), and (9.272)):

$$p_s^{\mathrm{IS}} = [1 + 2(1+e)\varepsilon_s g]\ \varepsilon_s \rho_s \theta \tag{78}$$

$$\mu_s^{\mathrm{IS}} = \frac{5}{96}\pi\rho_s d\sqrt{\frac{\theta}{\pi}}\frac{2}{(1+e)g}\left(1+\frac{4}{5}(1+e)\varepsilon_s g\right)^2 + \frac{4}{5}\varepsilon_s^2\rho_s d g(1+e)\sqrt{\frac{\theta}{\pi}} \tag{79}$$

$$\kappa_s^{\mathrm{IS}} = \frac{75}{384}\pi\rho_s d\sqrt{\frac{\theta}{\pi}}\frac{2}{(1+e)g}\left(1+\frac{6}{5}(1+e)\varepsilon_s g\right)^2 + 2\varepsilon_s^2\rho_s dg(1+e)\sqrt{\frac{\theta}{\pi}} \tag{80}$$

where g is the value of the radial distribution function of a hard-sphere fluid at contact and e is the coefficient of normal restitution. Note that from Eq. (78) it follows that the excess compressibility of the IS system is equal to

$$y^{\mathrm{IS}} = 2(1+e)\varepsilon_s g = \frac{(1+e)}{2}y^{\mathrm{ES}} \tag{81}$$

that is, the dissipation in the collisions reduces the excess compressibility by a factor of $(1+e)/2$. Replacing $2(1+e)\varepsilon_s g$ in Eqs. (79) and (80) by y^{IS} and using expression in Eq. (72) for μ_s^{id} and k_s^{id} gives

$$\mu = \mu_s^{\mathrm{id}}4\varepsilon_s\left[\frac{1}{y^{\mathrm{IS}}}\left(1+\frac{2}{5}y^{\mathrm{IS}}\right)^2 + \frac{48}{25\pi}y^{\mathrm{IS}}\right] = \mu_s^{\mathrm{id}}4\varepsilon_s\left(\frac{1}{y_{\mathrm{IS}}}+\frac{4}{5}+0.771y^{\mathrm{IS}}\right) \tag{82}$$

$$\kappa = \kappa_s^{\mathrm{id}}4\varepsilon_s\left[\frac{1}{y^{\mathrm{IS}}}\left(1+\frac{3}{5}y^{\mathrm{IS}}\right)^2 + \frac{32}{25\pi}y^{\mathrm{IS}}\right] = \kappa_s^{\mathrm{id}}4\varepsilon_s\left(\frac{1}{y_{\mathrm{IS}}}+\frac{6}{5}+0.767y^{\mathrm{IS}}\right) \tag{83}$$

which are of the same form as the Enskog expressions in Eqs. (75) and (76), with y^{ES} replaced by y^{IS}.[3] It thus turns out, like for the elastic hard spheres, that the constitutive equations are completely determined by the excess compressibility, and that the general form of the Enskog equations is not affected by the dissipation of energy in the collisions.

Note that in the granular temperature equation Eq. (61), there is one extra term that is absent in the SET, namely the dissipation of fluctuating kinetic energy γ. From the KTGF follows that

$$\gamma = \frac{3}{2}(1-e)y^{\mathrm{IS}}\rho_s\varepsilon_s\theta\left[\frac{4}{d}\sqrt{\frac{\theta}{\pi}} - \nabla\cdot\mathbf{u}_s\right]$$

E. Numerical Solution Method

Owing to the tendency of inelastic particles to contract in high-density clusters, and the strong nonlinearity of the particle pressure near the maximum packing density, special attention has to be paid to the numerical implementation of the model equations. Most "classic" constant property TFMs are solved using computational methods based on the implicit continuous Eulerian (ICE) method pioneered by Harlow and Amsden (1975). The implementation is based on a finite difference technique and the algorithms closely resemble the SIMPLE algorithm (Patankar and Spalding, 1972), whereby a staggered grid is employed to reduce numerical instability. A detailed discussion on the application of this numerical technique to TFMs for gas-fluidized beds is presented by Kuipers *et al.* (1992).

In principle, this numerical solution method can be straightforwardly applied to "modern" TFMs with closure laws according to the KTGF. However, when doing so, the numerical stability of the TFM is highly affected by the value of the coefficient of normal restitution. Problems that can be handled with acceptable time steps of 10^{-4} s for ideal particles ($e = 1$) require time steps of 10^{-5} s when the coefficient of normal restitution is taken to be 0.97, and unacceptably small time steps of 10^{-6} s have to be taken when the coefficient of normal restitution is reduced below 0.93. This extreme sensitivity to the value of the coefficient of normal restitution is caused by the fact that particle volume fractions at the next time level are estimated without taking into account the strong nonlinear dependence of the particle pressure on the particle volume fraction. A new numerical algorithm, which estimates the new particle volume fraction taking the compressibility of the particulate phase more directly into account, is presented in this section.

1. Discretization of the Governing Equations

The set of conservation equations, supplemented with the constitutive equations, boundary, and initial conditions cannot be solved analytically, and a numerical method must be applied to obtain an approximate solution. Therefore, the domain of interest is divided into a number of fixed Eulerian cells through which the gas–solid dispersion moves. A standard finite difference technique is applied to discretize the governing equations.[4] The cells are labeled by indices i, j, and k located at their centers, and a staggered grid configuration is applied. According to this configuration the scalar variables are defined at the cell centers, whereas the velocities are defined at the cell faces, as indicated in Fig. 24. Furthermore, different control volumes have to be applied for mass and granular energy conservation on one hand and the momentum conservation equations on the other. The control volumes for mass and granular energy conservation coincide with the Eulerian cells, whereas the control volumes for momentum conservation in all three directions are shifted half a cell with respect to the Eulerian cells. Applying first-order time differencing and fully implicit treatment of the convective fluxes, the discretized form of continuity equation for the solid phase, Eq. (57), becomes

$$\begin{aligned}(\varepsilon_s\rho_s)^{n+1}_{i,j,k} - (\varepsilon_s\rho_s)^{n}_{i,j,k} &+ \frac{\delta t}{\delta x}\left\{\langle\varepsilon_s\rho_s u_{s,x}\rangle^{n+1}_{i+\frac{1}{2},j,k} - \langle\varepsilon_s\rho_s u_{s,x}\rangle^{n+1}_{i-\frac{1}{2},j,k}\right\} \\ &+ \frac{\delta t}{\delta y}\left\{\langle\varepsilon_s\rho_s u_{s,y}\rangle^{n+1}_{i,j+\frac{1}{2},k} - \langle\varepsilon_s\rho_s u_{s,y}\rangle^{n+1}_{i,j-\frac{1}{2},k}\right\} \\ &+ \frac{\delta t}{\delta z}\left\{\langle\varepsilon_s\rho_s u_{s,z}\rangle^{n+1}_{i,j,k+\frac{1}{2}} - \langle\varepsilon_s\rho_s u_{s,z}\rangle^{n+1}_{i,j,k-\frac{1}{2}}\right\} = 0 \qquad (84)\end{aligned}$$

[4]This part is based upon Chapter 2 of the thesis of Goldschmidt (2001).

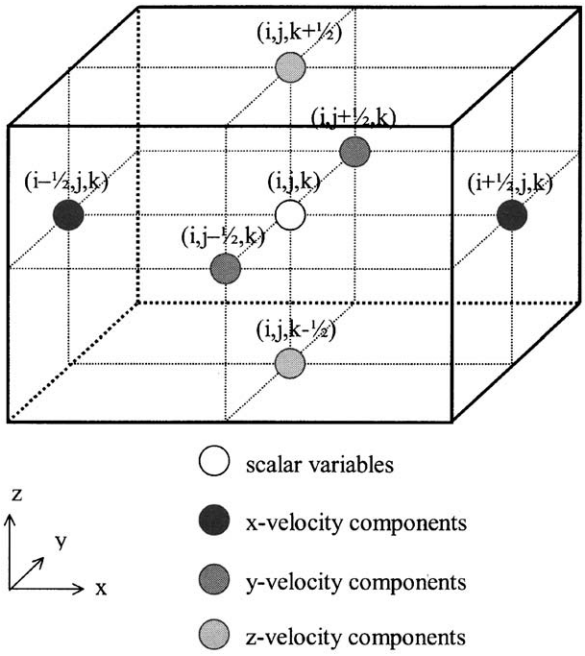

FIG. 24. Positions at which the key variables are evaluated for a typical computational cell in the staggered-grid configuration.

where the superscripts n and $n+1$ indicate that the quantities are at the old and the new time, respectively. For the discretization of all convective mass, momentum, and fluctuating kinetic energy fluxes the second-order accurate Barton scheme (Centrella and Wilson, 1984; Hawley *et al.*, 1984) is applied. A schematic representation of this scheme for the convective transport of a quantity D (e.g., $\varepsilon\rho$) by a velocity $V_{i+1/2}$ (e.g., u_x) is given in Fig. 25. In the discretization of the momentum Eq. (58), the terms associated with the gas and solid pressure gradients are treated fully implicitly. The interphase momentum transfer term is treated in a linear implicit fashion, and all other terms are treated explicitly. The discretization of the solid phase momentum in Eq. (58) for the x-direction is given by

$$(\varepsilon_s\rho_s u_{s,x})^{n+1}_{i+\frac{1}{2},j,k} = A^n_{i+\frac{1}{2},j,k} - (\varepsilon_s)^{n+1}_{i+\frac{1}{2},j,k}\frac{\delta t}{\delta x}\left\{(p)^{n+1}_{i+1,j,k} - (p)^{n+1}_{i,j,k}\right\} - \frac{\delta t}{\delta x}\left\{(p_s)^{n+1}_{i+1,j,k} - (p_s)^{n+1}_{i,j,k}\right\} + \delta t\beta^n_{i+\frac{1}{2},j,k}(u_x - u_{s,x})^{n+1}_{i+\frac{1}{2},j,k} \qquad (85)$$

where momentum convection, viscous interaction, and gravity have been collected in the explicit term A_n. The equation for the y-direction is obtained by

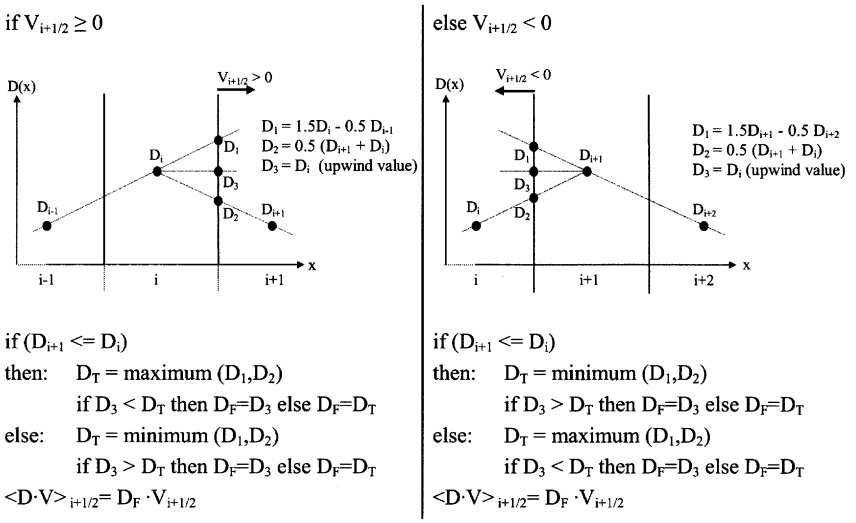

FIG. 25. Schematic representation of the Barton scheme for the convective flux of a quantity D by velocity $V_{i+1/2}$ in the x-direction.

substituting y for x, B for A, and a change of subscripts:

$$(\ldots)_{i+\frac{1}{2},j,k} \Rightarrow (\ldots)_{i,j+\frac{1}{2},k} \qquad (\ldots)_{i+1,j,k} \Rightarrow (\ldots)_{i,j+1,k}$$

and the equation for the z-direction is obtained by the substituting z for x, C for A, and a change of subscripts

$$(\ldots)_{i+\frac{1}{2},j,k} \Rightarrow (\ldots)_{i,j,k+\frac{1}{2}} \qquad (\ldots)_{i+1,j,k} \Rightarrow (\ldots)_{i,j,k+1}$$

Note that the mass and momentum equations for the gas phase can simply be obtained by replacing $\varepsilon_s \rightarrow \varepsilon$, $\rho_s \rightarrow \rho$, $\mathbf{u}_s \rightarrow \mathbf{u}$ in Eqs. (84) and (85), and dropping the terms concerning the particle-pressure gradient.

The granular energy equation is solved in a fully implicit manner. The solution of the equation however proceeds through a separate iterative procedure that solves the granular temperature equations for the whole computational domain when this is required by the main solution procedure discussed in the next paragraph. In this separate iterative procedure, the terms regarding convective transport and generation of fluctuating kinetic energy by viscous shear are explicitly expressed in terms of the most recently obtained granular temperature θ^*. The granular energy dissipation term is treated in a semi-implicit manner, whereas all other terms are treated fully implicitly. The

applied discretization of the granular temperature equation is given by

$$\begin{aligned}\frac{3}{2}(\varepsilon_s\rho_s\theta)^{n+1}_{i,j,k} = {} & \frac{3}{2}(\varepsilon_s\rho_s\theta)^{n}_{i,j} + D^{*}_{i,j,k} - \delta t 3\beta^{n}_{i,j,k}\theta^{n+1}_{i,j,k} - \delta t\left(\frac{\gamma}{\theta}\right)^{*}_{i,j,k}\theta^{n+1}_{i,j,k} \\ & - (p_s)^{n+1}_{i,j,k}\frac{\delta t}{\delta x}\left\{(u_{s,x})^{*}_{i+\frac{1}{2},j,k} - (u_{s,x})^{*}_{i-\frac{1}{2},j,k}\right\} \\ & - (p_s)^{n+1}_{i,j,k}\frac{\delta t}{\delta y}\left\{(u_{s,y})^{*}_{i,j+\frac{1}{2},k} - (u_{k,y})^{*}_{i,j-\frac{1}{2},k}\right\} \\ & - (p_s)^{n+1}_{i,j,k}\frac{\delta t}{\delta x}\left\{(u_{s,z})^{*}_{i,j,k+\frac{1}{2}} - (u_{k,y})^{*}_{i,j,k-\frac{1}{2}}\right\} \\ & + \frac{\delta t}{\delta x}\left\{(\kappa_s)^{*}_{i+\frac{1}{2},j,k}\frac{1}{\delta x}\left\{\theta^{n+1}_{i+1,j,k} - \theta^{n+1}_{i,j,k}\right\} - (\kappa_s)^{*}_{i-\frac{1}{2},j,k}\frac{1}{\delta x}\left\{\theta^{n+1}_{i,j,k} - \theta^{n+1}_{i-1,j,k}\right\}\right\} \\ & + \frac{\delta t}{\delta x}\left\{(\kappa_s)^{*}_{i,j+\frac{1}{2},k}\frac{1}{\delta y}\left\{\theta^{n+1}_{i,j+1,k} - \theta^{n+1}_{i,j,k}\right\} - (\kappa_s)^{*}_{i,j+\frac{1}{2},k}\frac{1}{\delta y}\left\{\theta^{n+1}_{i,j,k} - \theta^{n+1}_{i,j-1,k}\right\}\right\} \\ & + \frac{\delta t}{\delta z}\left\{(\kappa_s)^{*}_{i,j,k+\frac{1}{2}}\frac{1}{\delta z}\left\{\theta^{n+1}_{i,j,k+1} - \theta^{n+1}_{i,j,k}\right\} - (\kappa_s)^{*}_{i,j,k-\frac{1}{2}}\frac{1}{\delta z}\left\{\theta^{n+1}_{i,j,k} - \theta^{n+1}_{i,j,k-1}\right\}\right\} \end{aligned} \tag{86}$$

In this equation, the superscript (*) indicates that a term is computed based upon the most recent information, which complies with the $(n+1)$th time level when all iterative loops have converged. Further, the convective transport and viscous generation of fluctuating kinetic energy have been collected in the explicit term D^*. The iterative solution procedure for the granular energy equations continues until the convergence criteria

$$\theta^{n+1}_{i,j,k} - \theta^{*}_{i,j,k} < \varepsilon_\theta \cdot \theta^{n+1}_{i,j,k} \tag{87}$$

are simultaneously satisfied for all cells within the computational domain. For a typical value of $\varepsilon_\theta = 10^{-6}$, this takes only a couple of iterations per time step.

2. *Solution Procedure of the Finite Difference Equations*

The numerical solution of the discretized model equations evolves through a sequence of computational cycles, or time steps, each of duration δt. For each computational cycle, the advanced $(n+1)$-level values at time $t+\delta t$ of all key variables have to be calculated for the entire computational domain. This calculation requires the old n-level values at time t, which are known from either the previous computational cycle or the specified initial conditions. Then each computational cycle consists of two distinct phases:

- calculation of the explicit terms A^n, B^n, and C^n in the momentum equations for all interior cells and
- implicit determination of the pressure, volume fraction, and granular temperature distributions throughout the computational domain with an iterative procedure. The implicit phase consists of several steps.

The first step involves the calculation of the mass residuals of the solid phase $(D_s)_{i,j,k}$ and the gas phase $(D_g)_{i,j,k}$ from the continuity equations, for all interior cells:

$$\begin{aligned}(D_{\mathrm{s}})^{*}_{i,j,k} = {} & (\varepsilon_{\mathrm{s}}\rho_{\mathrm{s}})^{*}_{i,j,k} - (\varepsilon_{\mathrm{s}}\rho_{\mathrm{s}})^{n}_{i,j,k} \\ & + \frac{\delta t}{\delta x}\left\{\langle \varepsilon_{\mathrm{s}}\rho_{\mathrm{s}}u_{\mathrm{s},x}\rangle^{*}_{i+\frac{1}{2},j,k} - \langle \varepsilon_{\mathrm{s}}\rho_{\mathrm{s}}u_{\mathrm{s},x}\rangle^{*}_{i-\frac{1}{2},j,k}\right\} \\ & + \frac{\delta t}{\delta y}\left\{\langle \varepsilon_{\mathrm{s}}\rho_{\mathrm{s}}u_{\mathrm{s},y}\rangle^{*}_{i,j+\frac{1}{2},k} - \langle \varepsilon_{\mathrm{s}}\rho_{\mathrm{s}}u_{\mathrm{s},y}\rangle^{*}_{i,j-\frac{1}{2},k}\right\} \\ & + \frac{\delta t}{\delta z}\left\{\langle \varepsilon_{\mathrm{s}}\rho_{\mathrm{s}}u_{\mathrm{s},z}\rangle^{*}_{i,j,k+\frac{1}{2}} - \langle \varepsilon_{\mathrm{s}}\rho_{\mathrm{s}}u_{\mathrm{s},z}\rangle^{*}_{i,j,k-\frac{1}{2}}\right\}\end{aligned} \tag{88}$$

$$\begin{aligned}(D_{\mathrm{g}})^{*}_{i,j,k} = {} & (\varepsilon\rho)^{*}_{i,j,k} - (\varepsilon\rho)^{n}_{i,j,k} \\ & + \frac{\delta t}{\delta x}\left\{\langle \varepsilon\rho u_x\rangle^{*}_{i+\frac{1}{2},j,k} - \langle \varepsilon\rho u_x\rangle^{*}_{i-\frac{1}{2},j,k}\right\} \\ & + \frac{\delta t}{\delta y}\left\{\langle \varepsilon\rho u_y\rangle^{*}_{i,j+\frac{1}{2},k} - \langle \varepsilon\rho u_y\rangle^{*}_{i,j-\frac{1}{2},k}\right\} \\ & + \frac{\delta t}{\delta z}\left\{\langle \varepsilon\rho u_z\rangle^{*}_{i,j,k+\frac{1}{2}} - \langle \varepsilon\rho u_z\rangle^{*}_{i,j,k-\frac{1}{2}}\right\}\end{aligned} \tag{89}$$

If the convergence criteria

$$(D_{\mathrm{g}})^{*}_{i,j,k} < \boldsymbol{\varepsilon}_g \cdot (\varepsilon\rho)^{*}_{i,j,k} \tag{90}$$

$$(D_{\mathrm{s}})^{*}_{i,j,k} < \boldsymbol{\varepsilon}_{\mathrm{s}} \cdot (\varepsilon_{\mathrm{s}}\rho_{\mathrm{s}})^{*}_{i,j,k} \tag{91}$$

are not satisfied for all computational cells (typically $\boldsymbol{\varepsilon}_{\mathrm{g}} = \boldsymbol{\varepsilon}_{\mathrm{s}} = 10^{-6}$), a whole field pressure correction is calculated, satisfying

$$\begin{aligned}(D_g)^{*}_{i,j,k} = {} & -(J_g)^{n}_{i,j,k}(\delta p)_{i,j,k} \\ & -(J_g)^{n}_{i-1,j,k}(\delta p)_{i-1,j,k} - (J_g)^{n}_{i+1,j,k}(\delta p)_{i+1,j,k} - (J_g)^{n}_{i,j-1,k}(\delta p)_{i,j-1,k} \\ & -(J_g)^{n}_{i,j+1,k}(\delta p)_{i,j+1,k} - (J_g)^{n}_{i,j,k-1}(\delta p)_{i,j,k-1} - (J_g)^{n}_{i,j,k+1}(\delta p)_{i,j,k+1}\end{aligned} \tag{92}$$

where $(J_g)^n$ represents the Jacobi matrix for the gas phase. This matrix contains the derivatives of the defects D_g with respect to the gas phase pressure, for which explicit expressions can be obtained from the continuity equation for the gas phase in combination with the momentum equations. To save computational effort, the elements of the Jacobi matrix are evaluated at the old time level. The banded matrix problem corresponding to Eq. (92) is solved using a standard ICCG sparse matrix technique. Once new pressures have been obtained, the corresponding new gas phase densities are calculated.

So far, the solution procedure has been exactly the same as the SIMPLE procedure that is usually applied for the solution of the "classic" TFMs with

constant property closure equations. In the next step however, the standard procedures continue with the computation of the new velocities from the coupled momentum equations, after which the new volume fractions are obtained from the solid phase mass balances, and only then the new solid pressures are determined. This regularly leads to excessive compaction and extremely high particle pressures in areas where the particle packing densities are close to random close packing. Therefore, the new solution procedure computes the particle volume fractions, taking the compressibility of the solid phase more directly into account. Similar to the pressure correction for the gas phase, a whole field particle volume fraction correction is computed, satisfying

$$\begin{aligned}(D_{\mathrm{s}})^{*}_{i,j,k} = & -(J_{\mathrm{s}})^{n}_{i,j,k}(\delta\varepsilon_{\mathrm{s}})_{i,j,k} \\ & -(J_{\mathrm{s}})^{n}_{i-1,j,k}(\delta\varepsilon_{\mathrm{s}})_{i-1,j,k} - (J_{\mathrm{s}})^{n}_{i+1,j,k}(\delta\varepsilon_{\mathrm{s}})_{i+1,j,k} - (J_{\mathrm{s}})^{n}_{i,j-1,k}(\delta\varepsilon_{\mathrm{s}})_{i,j-1,k} \\ & -(J_{\mathrm{s}})^{n}_{i,j+1,k}(\delta\varepsilon_{\mathrm{s}})_{i,j+1,k} - (J_{\mathrm{s}})^{n}_{i,j,k-1}(\delta\varepsilon_{\mathrm{s}})_{i,j,k-1} - (J_{\mathrm{s}})^{n}_{i,j,k+1}(\delta\varepsilon_{\mathrm{s}})_{i,j,k+1} \end{aligned} \tag{93}$$

In this Eq. $(J_s)^n$ is the Jacobi matrix for the solid phase, which contains the derivatives of the mass residuals for the particulate phase to the solid volume fraction. Explicit expressions for the elements of the Jacobi matrix can be obtained from the continuity for the solid phase and the momentum equations. For example for the central element, the following expression is obtained from the solid phase continuity equation, in which the convective terms are evaluated with central finite difference expressions:

$$\begin{aligned}(J_{\mathrm{s}})^{n}_{i,j,k} = \frac{\partial(D_{\mathrm{s}})^{*}_{i,j,k}}{\partial(\varepsilon_{\mathrm{s}})^{*}_{i,j,k}} = (\rho_{\mathrm{s}})^{*}_{i,j,k} & + \frac{\delta t}{\delta x}\left\{\frac{\partial(\varepsilon_{\mathrm{s}}\rho_{\mathrm{s}}u_{\mathrm{s},x})^{*}_{i+\frac{1}{2},j,k}}{\partial(\varepsilon_{\mathrm{s}})^{*}_{i,j,k}} - \frac{\partial(\varepsilon_{\mathrm{s}}\rho_{\mathrm{s}}u_{\mathrm{s},x})^{*}_{i-\frac{1}{2},j,k}}{\partial(\varepsilon_{\mathrm{s}})^{*}_{i,j,k}}\right\} \\ & + \frac{\delta t}{\delta y}\left\{\frac{\partial(\varepsilon_{\mathrm{s}}\rho_{\mathrm{s}}u_{\mathrm{s},y})^{*}_{i,j+\frac{1}{2},k}}{\partial(\varepsilon_{s})^{*}_{i,j,k}} - \frac{\partial(\varepsilon_{\mathrm{s}}\rho_{\mathrm{s}}u_{\mathrm{s},y})^{*}_{i,j-\frac{1}{2},k}}{\partial(\varepsilon_{s})^{*}_{i,j,k}}\right\} \\ & + \frac{\delta t}{\delta z}\left\{\frac{\partial(\varepsilon_{\mathrm{s}}\rho_{\mathrm{s}}u_{\mathrm{s},z})^{*}_{i,j,k+\frac{1}{2}}}{\partial(\varepsilon_{\mathrm{s}})^{*}_{i,j,k}} - \frac{\partial(\varepsilon_{\mathrm{s}}\rho_{\mathrm{s}}u_{\mathrm{s},z})^{*}_{i,j,k-\frac{1}{2}}}{\partial(\varepsilon_{\mathrm{s}})^{*}_{i,j,k}}\right\}\end{aligned} \tag{94}$$

The derivatives of the mass fluxes to the solid volume fractions can subsequently be obtained from the solid phase momentum equations. From Eq. (85), the discretized x-momentum equation, the derivatives of the mass fluxes in the x-direction can easily be obtained, e.g.,

$$\begin{aligned}\frac{\partial(\varepsilon_{\mathrm{s}}\rho_{\mathrm{s}}u_{\mathrm{s},x})^{*}_{i+\frac{1}{2},j,k}}{\partial(\varepsilon_{\mathrm{s}})^{*}_{i,j,k}} = & -\frac{1}{2}\frac{\delta t}{\delta x}\left\{(p)^{*}_{i+1,j,k} - (p)^{*}_{i,j,k}\right\} + \frac{\delta t}{\delta x}\left(\frac{\partial p_{\mathrm{s}}}{\partial\varepsilon_{\mathrm{s}}}\right)^{*}_{i,j,k} \\ & + \delta t\beta^{n}_{i+\frac{1}{2},j,k}\frac{\partial(u_x - u_{\mathrm{s},x})^{*}_{i+\frac{1}{2},j,k}}{\partial(\varepsilon_{\mathrm{s}})^{*}_{i,j,k}}\end{aligned} \tag{95}$$

The second term on the RHS of this equation shows that the compressibility of the solid phase is taken directly into account in the estimation of the new particle volume fractions. Furthermore, the expression for the derivatives of the velocities to the solid pressure can be obtained by combination with the x-momentum equation for the gas phase that results in

$$\frac{\partial(\varepsilon\rho u_x)^*_{i+\frac{1}{2},j,k}}{\partial(\varepsilon_s)^*_{i,j,k}} = \frac{1}{2}\frac{\delta t}{\delta x}\left\{(p)^*_{i+1,j,k} - (p)^*_{i,j,k}\right\} - \delta t\beta^n_{i+\frac{1}{2},j,k}\frac{\partial(u_x - u_{s,x})^*_{i+\frac{1}{2},j,k}}{\partial(\varepsilon_s)^*_{i,j,k}} \tag{96}$$

Together with Eq. (93), this equation forms a set of equations from which explicit expressions for the derivatives of the velocities can readily be obtained. Expressions for the y- and z-direction and for the other elements of the Jacobi matrix are obtained in a similar manner.

After the new solid volume fractions have been obtained from Eq. (93), new particle pressures are calculated, where after new velocities can be obtained from the coupled momentum equations. Next, new granular temperatures are calculated from the granular energy equations by an iterative procedure described in Section IV.E.1. Finally, the new mass residuals $(D_g)_{i,j,k}$ and $(D_s)_{i,j,k}$ are computed and the convergence criteria are checked again.

Though this new algorithm still requires some time step refinement for computations with highly inelastic particles, it turns out that most computations can be carried out with acceptable time steps of 10^{-5} s or larger. An alternative numerical method that is also based on the compressibility of the dispersed particulate phase is presented by Laux (1998). In this so-called compressible disperse-phase method the shear stresses in the momentum equations are implicitly taken into account, which further enhances the stability of the code in the quasi-static state near minimum fluidization, especially when frictional shear is taken into account. In theory, the stability of the numerical solution method can be further enhanced by fully implicit discretization and simultaneous solution of all governing equations. This latter is however not expected to result in faster solution of the TFM equations since the numerical efforts per time step increase.

F. Application to Geldart A Particles

A great challenge in CFD modeling of gas–solid two-phase flows is to obtain realistic predictions of the fluidization behavior of small particles such as Geldart A particles (Geldart, 1973), for which the standard TFM has so far failed to predict even the bubbling fluidization. Ferschneider and Mege (1996) found a major overprediction of bed expansion in a bubbling bed of FCC particles, and Bayle *et al.* (2001) obtained the same results in a turbulent bed of FCC particles. Recently, Lettieri *et al.* (2003) used a particle–bed model, originally developed by Chen *et al.* (1999), to investigate the homogeneous fluidization of Geldart A particles. It has been demonstrated that a

homogeneous expansion can be obtained in this particle–bed model. However in this model, an artificial particle-phase elasticity force is required. McKeen and Pugsley (2003) used the two-fluid CFD code MFIX to simulate a freely bubbling bed of FCC catalyst for $U_0 = 0.05$–$0.2\,\mathrm{m/s}$ and compared their simulation results with ECT data. In accordance with findings of Ferschneider and Mege (1996), McKeen and Pugsley (2003) also found that the standard CFD model greatly overpredicted bed expansion without any modifications of the drag closures. By using a scale factor of 0.25 for the commonly used gas–solid drag laws, they found that their simulation results are in accordance with experimental observations. They argued that this is due to the formation of clusters with a size smaller than the CFD grid size. Such small-scale clusters have not been reported before, in particular for particles with a size of $75\,\mu\mathrm{m}$.

Although the van der Waals force can play a role in the fluidization of Geldart A particles, it is not clear how this force affects the gas–solid drag. The influence of the cohesion on the KTGF has not been carefully checked so far. Recently, Kim and Arastoopour (2002) tried to extend the kinetic theory to cohesive particles; however, their final expression for the particular phase stress is very complex. A simpler route would be to assume that the Enskog expressions in Eqs. (75)–(76) still hold for cohesive particles, only with a modified excess compressibility. However at present, it proves difficult to give an accurate estimate of the deviation of y due to the cohesive force (see Fig. 22). Moreover, as discussed in Section III.F, also the magnitude of the cohesive force itself (i.e., the Hamaker constant) is not known. For this reason, we will only study the effect of the gas–particle drag in this section, where we use two different models: (i) the "ab-initio" drag model in Eq. (47) derived from detailed scale LB simulations and (ii) the empirical drag model in Eq. (46). Note that for the latter model, the literature values for the exponent n are extremely scattered (Morgan *et al.*, 1971). In Table IV, we show the results for n from different experiments for Geldart A particles, which are clearly much higher than the value $n = 4.65$, originally obtained by Richardson and Zaki (1954). In this section, we show results using the Wen and Yu expression with the commonly used value $n = 4.65$, and with the highest reported value $n = 9.6$, from the experiments by Lettieri *et al.* (2002).

For the simulations we use a 2D TFM as described in the previous sections. The simulation conditions are specified in Table V. The gas flow enters at the bottom through a porous distributor. The initial gas volume fraction in each fluid cell is set to an average value of 0.4 and with a random variation of $\pm 5\%$. Also for the boundary condition at the bottom, we use a uniform gas velocity with a superimposed random component (10%), following Goldschmidt *et al.* (2004).

The simulations show that for low gas velocities ($U_0 = 0.009$ m/s), the commonly used exponent $n = 4.65$ does not yield a realistic bed expansion dynamics for Geldart A particles. By using a large exponent ($n = 9.6$), which was determined by gas fluidization of Geldart A particles, we can get a bed expansion

TABLE IV
EXPONENT n FOR GELDART A PARTICLES

d_p (μm)	n
Lettieri *et al.* (2002), Newton and Gates (2002):	Gas-fluidization
71	9.6
57	9.0
49	8.2
Massimilla *et al.* (1972):	Gas-fluidization ()
60	7.12
53	6.86
45	6.1
Lewis and Bowerman (1952):	Liquid-fluidization
86	8.3
Whitmore (1957):	Liquid-sedimentation
65	9.5

TABLE V
SIMULATION CONDITIONS

Parameters	Value	Parameter	Value
Gas shear viscosity	1.8×10^{-5} Pa · s	CFD cells	30×45
Gas temperature	293 K	Size of the cell	$5 \times 5\,\text{mm}^2$
Gas pressure	1.01×10^5 Pa	Particle diameter	75 μm
Gas constant	8.314 J/(mol K)	Particle density	$1{,}500\,\text{kg/m}^3$
CFD time step	1.0×10^{-4} s	Coefficient of restitution	0.97

around 31% of the initial bed height, which is much closer to the experimental results (Geldart, 1973). Basically, a larger exponent n in Eq. (46) will lead to a higher drag at the same gas velocity. It can thus be argued that at low-gas velocities the drag force is underestimated by the commonly used drag models. The question arises what the physical origin is of such large exponents. One possibility is that they are caused by microstructures that form from small-scale instabilities and perhaps other mechanisms. Also, the experiments by Lettieri *et al.* (2002) showed a much larger apparent terminal velocity, which is indicative of a much larger effective size. If such microstructures cannot be captured by the CFD grid, then the use of a modified drag function, such that the experimental bed expansion is obtained, is a possible way to go about. It should be stressed, however, that this type of approach is rather *ad hoc* and not in the spirit of the multiscale modeling strategy.

It has been reported by several researchers (Ferschneider and Mege, 1996; Bayle *et al.*, 2001; McKeen and Pugsley, 2003) that an overestimated bed expansion was found at a high-gas velocity (~0.2 m/s). We also carried out several simulations for a high gas velocity, $U_0 = 0.2\,\text{m/s}$. We still use the drag model given by Eq. (46) with an exponent $n = 4.65$. The simulation domain, however,

is enlarged so that a high bed expansion can be accommodated. The computational domain is composed of 30 × 70 cells, and the size of each cell still remains as 5 × 5 mm^2. With such a high gas velocity the bed in fact is in the turbulent fluidization regime. In Fig. 26, we show the results obtained at different points in time when the bed reaches a dynamical equilibrium. Clearly, the particle phase displays a turbulence-like flow pattern. Also, an overestimation of bed height is found in the simulations, which is around 100% of the initial bed height.

We also carried out a set of simulations using Eq. (47) as a drag model, which was based on the data of LB simulations. The results are shown in Fig. 27. As can be seen, no big differences can be observed compared to the results from the drag model given by Eq. (46) with an exponent $n = 4.65$.

A similar simulation was also carried out by McKeen and Pugsley (2003). They also found an overestimation of the bed height, compared to their experimental results. They argued that a factor should be used to scale down the

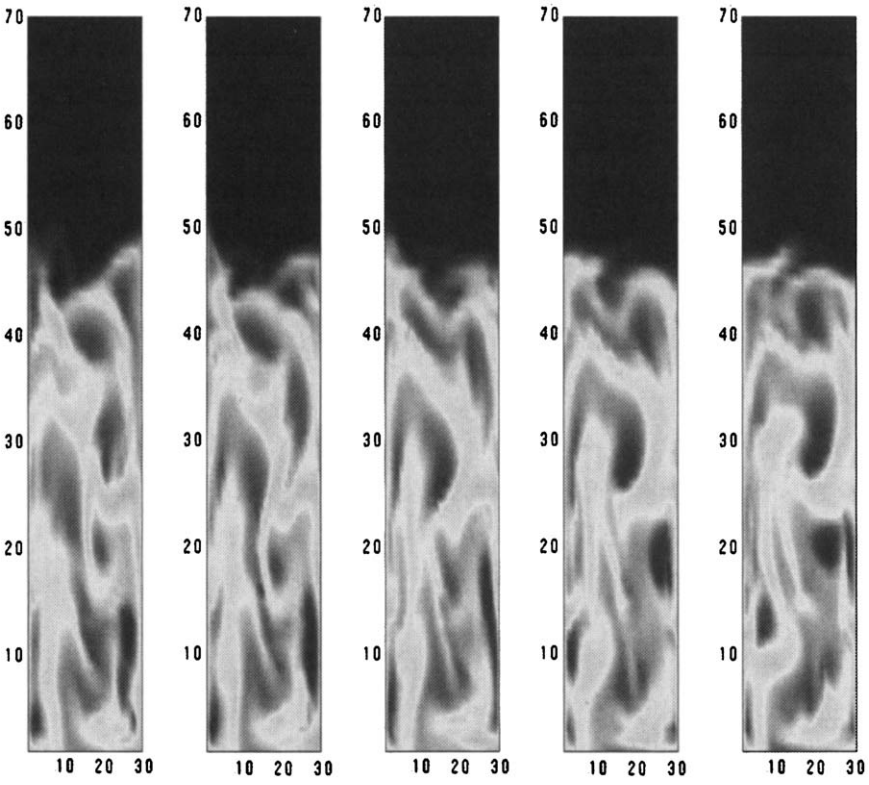

FIG. 26. The bed expansion dynamics of Geldart A particles from the TFM. The superficial gas velocity U_0 is set to 0.2 m/s. The exponent n of the Wen and Yu equation is set to 4.65. No cohesion is considered here. The results are, from the right to left, taken at $t = 9.6$, 9.7, 9.8, 9.9, and 10.0 s.

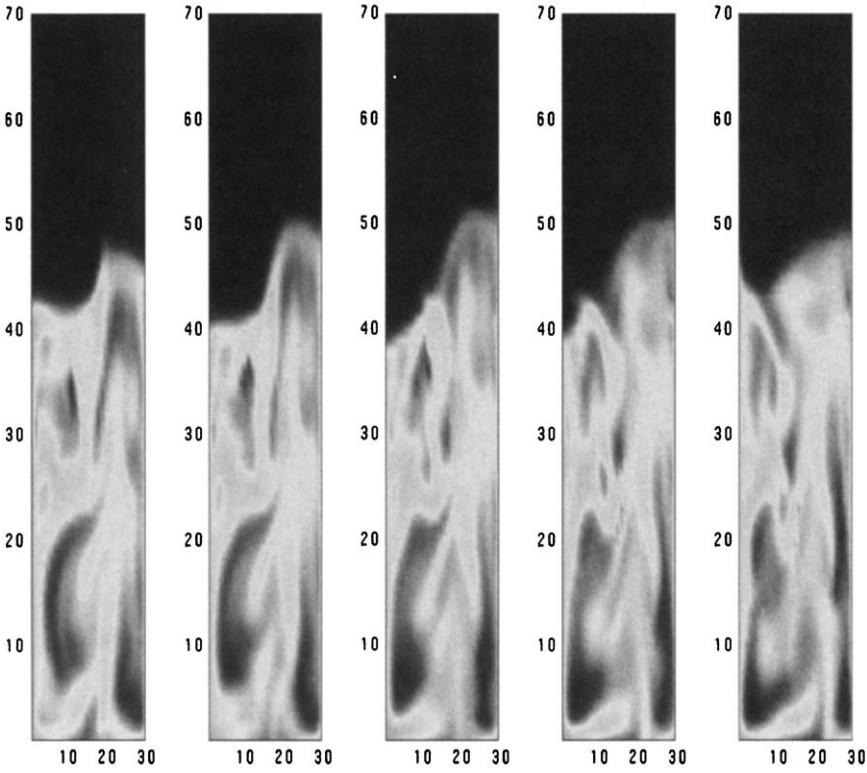

FIG. 27. The same as in Fig. 26, but now using the LB drag model in Eq. (47) from Hill *et al.* (2001b), with $A_2 = A_o$.

drag force in this regime in order to obtain a better agreement with the experiments. In Fig. 28, we show the results of our simulations with a drag force ($n = 4.65$) scaled down by a factor 0.15. A significant decrease of the bed height is found, with a bed expansion that is around 16% of the initial bed height, close to the experimental observations (McKeen and Pugsley, 2003).

V. Towards Industrial-Scale Models

In Section I, we mentioned that the TFM can simulate fluidized beds at *engineering* scales (height 1–2 m), and that the large-scale industrial fluidized-bed reactors (diameter 1–5 m, height 3–20 m) are still far beyond its capabilities. Clearly, it would be highly desirable to predict the properties of gas–solid flows at the industrial scale; however at present, there is no fully evolved model—based on fundamental principles—which is capable of this. In this section, we outline some new ideas in this direction that have been developed both at the

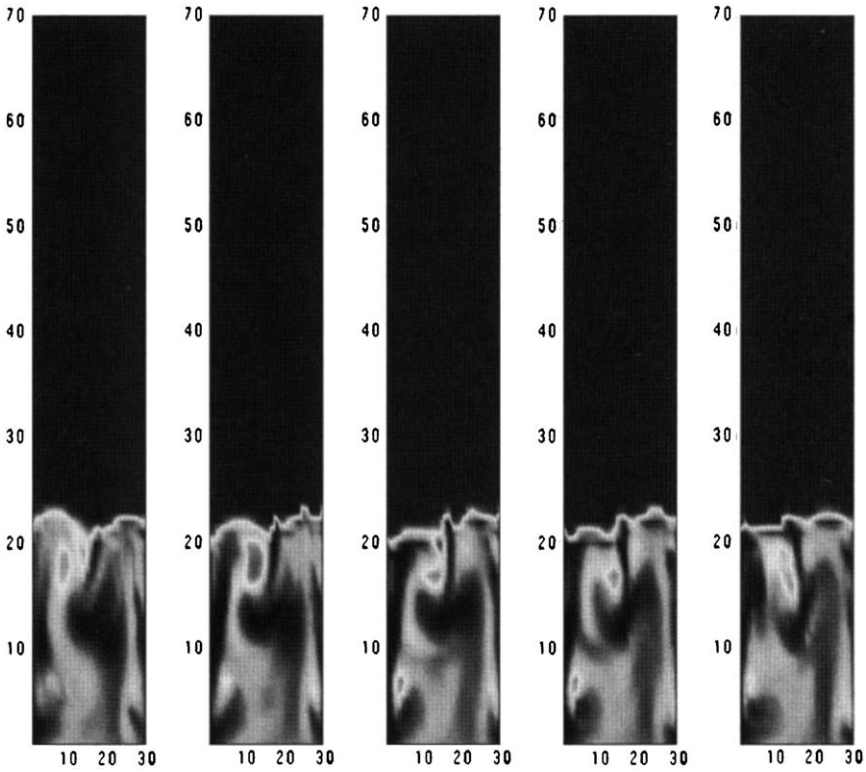

FIG. 28. The same as in Fig. 26, but with the drag force scaled by a factor of 0.15.

Princeton University and at the University of Twente. Before doing so; however, it is first important to understand why the current class of TFMs is not suitable for describing large-scale gas–solid flows.

A. The Limits of the Two-Fluid Model

Let us step back and examine the TFM and the closures we described thus far in the chapter. Recall that the details of flow at the level of individual particles are erased by the averaging process leading to the TFM equations, and that their consequences appear in the averaged equations through terms which have to be closed. The size of the averaging region was not explicitly considered anywhere in the derivation of the TFM equations or the closures, and it was implicitly assumed that a separation of scale exists—namely, the size of the averaging region is much larger than the particle size—but is much smaller than the scale of the macroscopic flow structure that we wish to study by solving the TFM equations. The assumption of such a separation of scales underlies the very formulation of continuum models.

Furthermore, the closures for the fluid−particle drag and the particle-phase stresses that we discussed were all derived from data or analysis of nearly homogeneous systems. In what follows, we refer to the TFM equations with closures deduced from nearly homogeneous systems as the *microscopic TFM* equations. The kinetic theory based model equations fall in this category.

We illustrated how these equations are discretized over an appropriate numerical grid and also showed some sample results. One can readily appreciate that one must choose the grid sizes in the numerical solution of the TFM equations to be smaller than the shortest length scale at which the TFM equations afford inhomogeneities. This requirement leads to a practical difficulty when one tries to solve these microscopic TFM equations for gas–particle flows, as discussed below.

Gas–particle flows in fluidized beds and riser reactors are inherently unstable and they manifest *inhomogeneous structures* over a wide range of length and time scales. There is a substantial body of literature where researchers have sought to capture these fluctuations through numerical simulation of microscopic TFM equations, and it is now clear that TFMs for such flows do reveal unstable modes whose length scale is as small as ten particle diameters (e.g., see Agrawal *et al.*, 2001; Andrews *et al.*, 2005).

This is illustrated in Fig. 29. Transient simulations of a fluidized suspension of ambient air and typical fluid catalytic cracking catalyst particles were performed (using MFIX (Syamlal *et al.*, 1993; Syamlal, 1998, which is an open-domain code for solving multiphase flow problems) in a 2D periodic domain at different grid resolutions. These simulations employed kinetic theory-based (microscopic) TFM equations; see Agrawal *et al.* (2001) for a summary of the equations, closures, and parameter values used in the simulations. Although there are some slight differences between the closure expressions used by these authors and those described (as illustrative examples) in this article, the differences are only quantitative and not qualitative, so there is no need to present these closures here. A pressure drop that is commensurate with the weight of the gas–particle mixture in the periodic box was applied across the box in the vertical direction, which provided the driving force for the upflow of the fluidizing gas. The simulations revealed that an initially homogeneous suspension gave way to an inhomogeneous state with persistent fluctuations. Snapshots of the particle volume fraction fields obtained in simulations with different number of spatial grids are shown in Fig. 29.

It is readily apparent that finer and finer structures get resolved as the number of spatial grids is increased. Statistical quantities, such as average slip velocity between the gas and particle phases, obtained by averaging over the whole domain, were found to depend on the grid resolution employed in the simulations and they became *nearly* grid-size independent only when grid sizes of the order of a few (≈ 10) particle diameters were used. Thus, if one sets out to solve microscopic TFM equations, grid sizes of the order of few particle

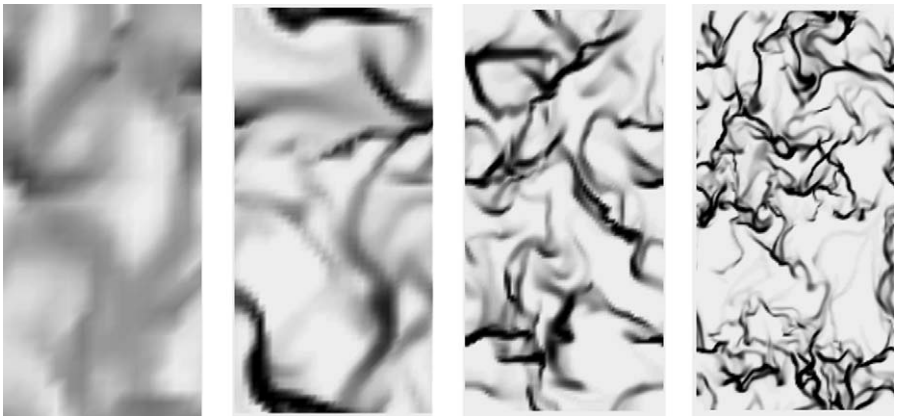

FIG. 29. Snapshots of particle volume fraction fields obtained while solving a kinetic theory-based TFM. 75 μm fluid catalytic particles in ambient air. Simulations were done over a 16×32 cm periodic domain. The average particle volume fraction in the domain is 0.05. Dark (light) color indicates regions of high (low) particle volume fractions. (See Refs. Agrawal *et al.*, 2001; Andrews *et al.*, 2005) for other parameter values.) Source: Andrews and Sundaresan (2005).

diameters are required; such fine spatial grids (and the fact that inhomogeneous structures extend down to this fine scale) limit the time steps that can be taken as well. For most devices of practical (commercial) interest, such extremely fine spatial grids and small time steps are unaffordable (e.g., see Sundaresan, 2000). Indeed, gas–particle flows in large fluidized beds and risers are often simulated by solving discretized versions of the TFM equations over *coarse spatial grids*. Such coarse-grid simulations do not resolve the small-scale (i.e., subgrid scale) spatial structures that, according to the microscopic TFM equations, do indeed exist. The effect of these unresolved structures must be brought to bear on the structures resolved in coarse-grid simulations through appropriate modifications to the closures—for example, the effective drag coefficient in the coarse-grid simulations will be smaller than that in the original TFM to reflect the tendency of the gas to flow around the unresolved clusters. Qualitatively, this is equivalent to an effectively larger apparent size for the particles.

One can readily pursue this line of thought and examine the influence of these unresolved structures on the effective interphase transfer and dispersion coefficients that should be used in coarse-grid simulations. Inhomogeneous distribution of particles will promote by passing of the gas around the particle-rich regions and this will necessarily decrease the effective interphase mass and energy transfer rates. Similarly, fluctuations associated with the small-scale inhomogeneities will contribute to the rate of dispersion of the particles and the gas, but they will be unaccounted for in the coarse-grid simulations of the microscopic TFM equations.

B. State-of-the-Art on Dealing with Unresolved Structures

Researchers have approached this problem of treating unresolved structures through various approximate schemes. O'Brien and Syamlal (1993) and Boemer *et al.* (1994) pointed out the need to correct the drag coefficient to account for the consequence of clustering and proposed a correction for the very dilute limit. Some authors have used apparent cluster size in an effective drag-coefficient closure as a tuning parameter; for example see McKeen and Pugsley (2003), who attribute the larger apparent size to interparticle attractive forces, and others have deduced corrections to the drag coefficient using energy minimization multiscale approach (see Yang *et al.*, 2004). The concept of particle-phase turbulence has also been explored to introduce the effect of the fluctuations associated with clusters and streamers on the particle-phase stresses (Dasgupta *et al.*, 1994; Hrenya and Sinclair, 1997). However, a systematic approach that combines the influence of the unresolved structures on the drag coefficient and the stresses that can arise even when interparticle forces are not important has not yet emerged.

One can summarize the multiscale character of TFM simulations using coarse spatial grids as follows. When confronted with the task of performing simulation of gas–particle flows in large process vessels, one faces constraints on affordable grid resolution; this can lead to unresolved subgrid structures that would have been obtained if only the TFM equations were solved on a fine spatial grid. The consequence of these subgrid structures on the flow pattern resolved by the coarse-grid simulations should be brought in through appropriate corrections to the closure relations. If one simply uses the closures in the microscopic TFM without adding the corrections, then there is no guarantee that the obtained solution is a true solution for the TFM equations that one sets out to solve.

This is well known in other contexts, such as single-phase turbulence. Large eddy simulations introduce corrections to the fluid-phase stress through subgrid models; for example, Smagorinsky, in his pioneering work (Smagorinsky, 1963), introduced a model for subgrid viscosity correction.

Agrawal *et al.* (2001) pointed out that, in gas–particle flows such as those encountered in fluidized beds and riser flows, one should include subgrid corrections for not only the effective particle and fluid-phase stresses but also the effective drag. They showed that the effective drag law and the effective stresses obtained by averaging (the results gathered in highly resolved simulations of a set of microscopic TFM equations, such as that corresponding to the most resolved snapshot in Fig. 29 over the whole (periodic) domain were very different from those used in the microscopic TFM *and* that they depended on size of the domain over which simulations were carried out (Agrawal *et al.*, 2001). They also found that all the effects seen in the 2D simulations persisted when simulations were repeated in three dimensions (3D) and that both 2D and 3D simulations revealed the same qualitative trends.

Andrews *et al.* (2005) performed many highly resolved simulations of fluidized gas–particle mixtures in a 2D periodic domain, whose size coincided with that of the grid size in an anticipated large-scale riser flow simulation. Through such highly resolved simulations, they constructed *ad hoc* subgrid models for the effects of the fine-scale flow structures on the drag force and the stresses, and examined the consequence of these subgrid models on the outcome of the coarse-grid simulations of gas–particle flow in a large-scale vertical riser. They have demonstrated that these subgrid scale corrections can affect the predicted flow patterns profoundly.

Thus, there is no doubt that one must carefully examine whether the microscopic TFM equations must be modified to introduce the effects of unresolved structures before embarking on coarse-grid simulations of gas–particle flows in chemical reactors. At the same time, the *ad hoc* method employed by Andrews *et al.* (2005), namely performing highly resolved simulations in periodic domains whose linear dimensions are the same as those of the grids, is not a rigorous approach to take either; for example, one can anticipate that the periodic boundary conditions imposed in such highly resolved simulations would place some restrictions (on the small-scale flow structure) that would be absent in the real, large-scale flow. Thus, alternate approaches to constructing closures suitable for coarse-grid computations must be developed.

Adopting the approach pursued in large eddy simulations, one can start with the TFM equations and perform a filtering operation, where the averaging is done over a "filter" length scale that is somewhat larger than the grid size to be used in the coarse-grid simulation of large-scale process vessels and over high (temporal) frequencies. The mathematical steps involved in filtering any version of the microscopic TFM are conceptually straightforward (e.g., see Zhang and VanderHeyden, 2002) and will not be presented here. We simply note that the dominant terms in the filtered equations can be recast in exactly the same form as the original TFM equations; however, effective stresses, interphase interaction force term, etc. will now involve additional contributions resulting from the filtering process. (It is because of this similarity that one can use the same platform such as MFIX to perform integration of the filtered equations as well.) Insight into these closures for the additional contributions resulting from the filtering process can be gained through analysis of computational data gathered through highly resolved simulations in sufficiently large domains, while ensuring that the overall flow domain simulated is considerably larger than the region over which the filtering operation is performed. This is illustrated below by some results obtained by Andrews and Sundaresan (2005).

Consider a highly resolved simulation of a set of microscopic TFM equations for a fluidized suspension of particles in a large periodic domain. The filtering operation does not require a periodic domain; however, as each location in a periodic domain is statistically equivalent to any other location, statistical averages can be gathered much faster when simulations are done in periodic domains. After an initial transient period that depends on the initial conditions,

persistent, time-dependent, and spatially inhomogeneous structures develop. Fig. 30 shows an instantaneous snapshot of the particle volume fraction field in one such 2D simulation (performed using MFIX) and the cells (i.e., fine grids) used in the simulations. One can then zoom in any region of desired size and average any quantity of interest over all the cells inside that region, and obtain region-averaged (filtered) values. Note that one can choose a large number of regions inside the overall domain and thus several region-averaged values can be constructed for any quantity of interest from each instantaneous snapshot. When the system is in a statistical steady state, one can construct tens of thousands of such averages by repeating the analysis at various time instants.

Returning to Fig. 30, note that the averages over different regions at any given time are not equivalent; for example, at the given instant, different regions (of the same size) will correspond to different region-averaged particle volume fractions, particle and fluid velocities, and so on. Thus, one cannot simply lump the results obtained over all the regions; instead, the results must be grouped

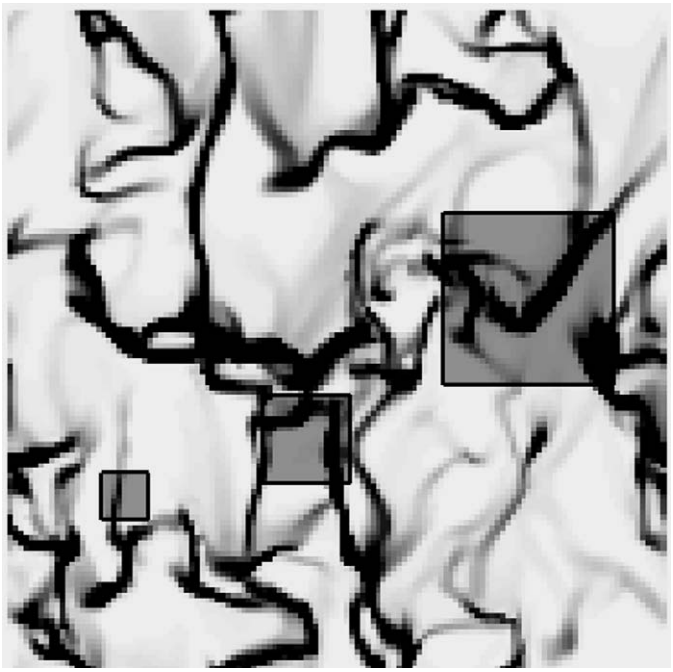

FIG. 30. Snapshot of particle volume fraction fields obtained while solving a kinetic theory-based TFM. Fluid catalytic particles in air. Simulations were done over a 16×16 cm periodic domain. 128×128 cells (shown in the figure). The average particle volume fraction in the domain is 0.05. Dark (light) color indicates regions of high (low) particle volume fractions. Squares of different sizes illustrate regions (i.e., filters) of different sizes over which averaging over the cells is performed. Source: Andrews and Sundaresan (2005).

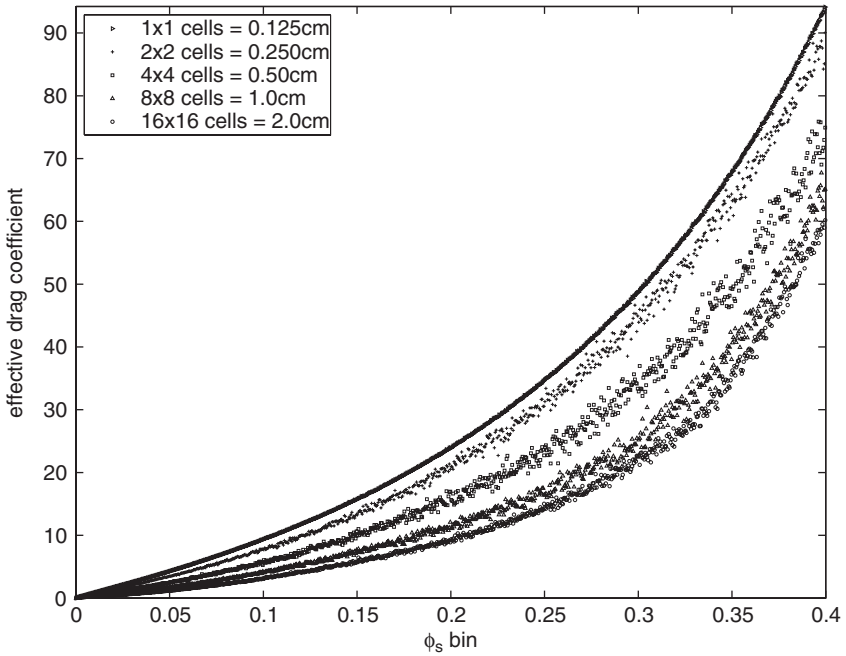

FIG. 31. Filtered drag coefficient (in CGS units) extracted from simulations over 16 × 16 cm domain using 128 × 128 cells. Source: Andrews and Sundaresan (2005).

into bins based on various markers and perform statistical averages within each bin to get useful information. The 2D simulations of Andrews and Sundaresan (2005) revealed that the single most important marker for regions is the average particle volume fraction in that region. Therefore, in order to expose the effects of particle volume fraction on the filtered (i.e., region-averaged) quantities, they classified the region-averaged data into bins of particle volume fraction and evaluated the filtered slip velocity, fluid–particle interaction force, etc., and averaged each of these quantities within each bin. From such bin statistics, they calculated the filtered drag coefficient, filtered particle-phase pressure, and filtered particle-phase viscosity as functions of filtered particle volume fraction.

Fig. 31 shows the variation of the filtered drag coefficient as a function of the filtered (i.e., region-average) particle volume fraction for various filter sizes.[5] Each point represents the average of many realizations in a bin. (Here, the filtered drag coefficient is defined as the region-average drag force divided by the region-average slip velocity.) It is clear from Fig. 31 that the filtered drag

[5]Strictly speaking, one should use 2D bins involving particle volume fraction and a Reynolds number based on slip velocity to classify the filtered drag coefficient; however in these simulations, the Reynolds number effect was found to be weak and hence the data were collapsed to just volume fraction bins.

coefficient depends on the size of the filter used in the analysis. This figure includes results obtained from three different simulations corresponding to three different average particle volume fractions in the domain (0.05, 0.15, and 0.40). The larger the filter size the smaller is the drag coefficient , the reason being that the averaging (i.e., filtering) is being performed over larger and larger clusters—the larger the clusters, the greater is the bypassing of the gas around the clusters and hence lower is the apparent drag coefficient.

Fig. 32 shows the variation of filtered particle-phase pressure as a function of the filtered particle volume fraction for various filter sizes. Here the filtered particle-phase pressure includes the pressure arising from the streaming and collisional parts captured by the kinetic theory and the sub-filter-scale Reynolds-stress like velocity fluctuations (see Agrawal *et al.*, 2001 for further details). Indeed, the contributions resulting from the sub-filter-scale velocity fluctuations swamp the kinetic theory pressure, indicating that at the coarse-grid scale one can even ignore the kinetic theory contributions to the pressure! This figure clearly shows that the filtered particle-phase pressure increases with filter size, and this is a direct consequence of the fact that the energy associated with the

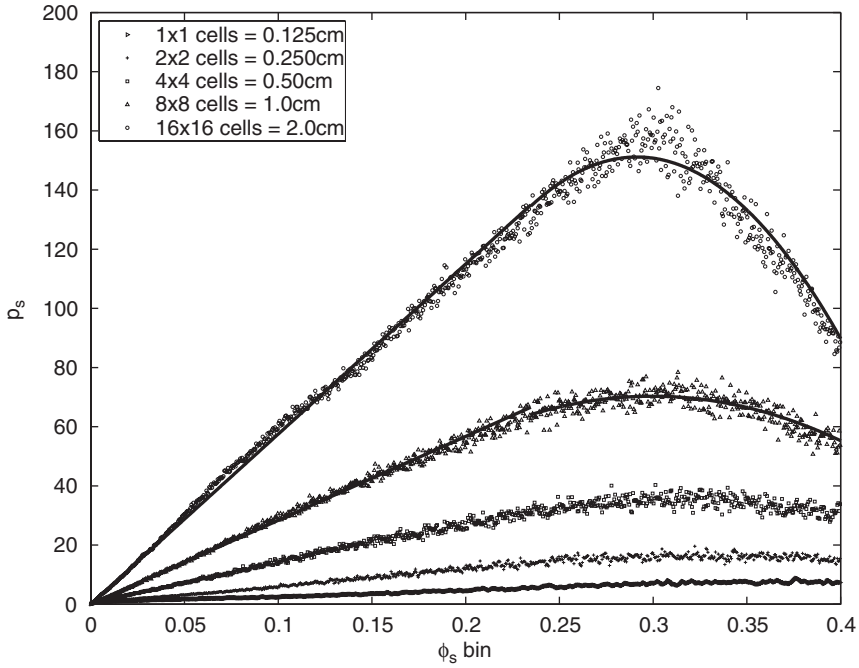

FIG. 32. Filtered particle phase pressure (in CGS units) extracted from simulations over 16 × 16 cm domain using 128 × 128 cells. Source: Andrews and Sundaresan (2005). The filtered particle-phase pressure includes the Reynolds stress-like fluctuations and the kinetic theory pressure.

velocity fluctuations increases with filter length (analogous to what one has in single-phase turbulence).

The trends presented in Figs. 31 and 32 qualitatively similar to those presented earlier by Agrawal *et al.* (2001) and Andrews *et al.* (2005) who, for the sake of simplicity, did simulations on much smaller domains and let the filter size be the same as the domain size. This shows clearly that the effects leading to the type of results presented in Figs. 31 and 32 are robust.

Andrews and Sundaresan (2005) have also extracted the filtered particle-phase viscosity from these simulations and found that at low particle volume fractions (0.0–0.25), the filtered viscosity varies nearly linearly with particle volume, and that it increases monotonically (and nearly linearly) with filter size.

A final piece of the proof-of-concept calculations is to compare the predictions obtained by solving the filtered TFM equations with highly resolved simulations of the microscopic TFM equations. For this purpose, Andrews and Sundaresan (2005) performed simulations of the microscopic TFM equations in a 16×32 cm periodic domain at various resolutions (e.g., see Fig. 29). From these simulations, they extracted domain-average quantities in the statistical steady state (see Agrawal *et al.*, 2001 for a discussion of how these data are gathered). Fig. 33 shows the domain-average slip velocity between the gas and particle phases at various grid resolutions (shown by the squares connected by

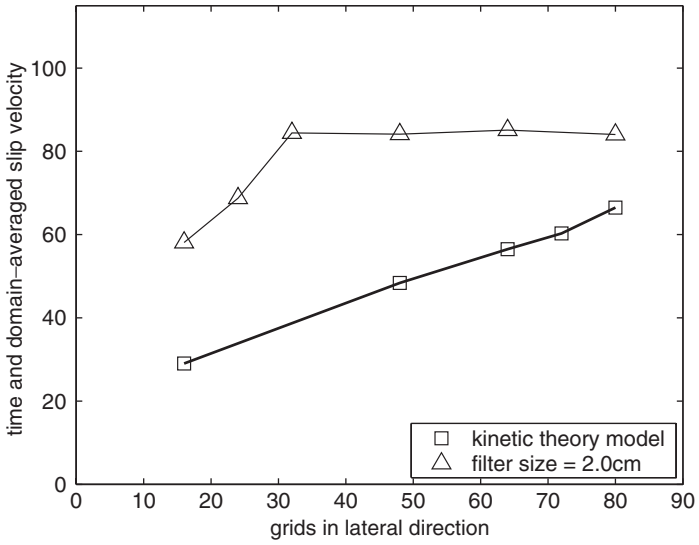

FIG. 33. Comparison of the domain-average slip velocity (in cm/s) determined by solving a microscopic TFM and the corresponding filtered TFM. 16×32 cm periodic domain. Domain-average particle volume fraction = 0.05. Number of grids in the vertical direction is twice that in the lateral direction. Source: Andrews and Sundaresan (2005).

the bold solid line in this figure). After sufficient grid resolution, this quantity clearly levels off, indicating convergence in a statistical sense. They also performed computations with the filtered TFM, using the computationally generated closures (e.g., drag and particle-phase pressure closures shown in Figs. 31 and 32, and particle-phase viscosity closure, not shown) for a 2×2 cm filter. The domain-average slip velocity obtained by solving the filtered equations at different grid resolutions are shown in Fig. 33 as triangles (connected by the thin solid line).

Fig. 33 reveals two important features. Firstly, at coarse resolutions, the domain-average slip velocity obtained by solving the microscopic TFM changes appreciably with grid resolution; in contrast, the grid-size dependence of the slip velocity computed by solving the filtered TFM is much weaker. Secondly, at sufficiently high-grid resolution, both approaches yield comparable predictions, and this is an important first step in validating the filtered TFM approach.

Another result that is not evident in Fig. 33 concerns the computational times required for gathering the statistical steady-state values of various quantities (such as the slip velocity shown in Fig. 33); at comparable grid resolutions, the computational time required to solve the filtered equations is much smaller than that for the microscopic equations. This can be attributed to the fact that the structures obtained in the solution of the filtered equations are comparatively coarser than those for the microscopic TFM equations.

C. A Different Approach: The Discrete Bubble Model

An alternative scheme to tackle the problem of large-scale flow structures is being pursued at Twente University. In this model the *bubbles*, as observed in the DPM and TFM models of gas-fluidized beds, are considered as discrete entities. This is the so-called discrete bubble model, which has been successfully applied in the field of gas–liquid bubble columns (Delnoij *et al.*, 1997). The idea to apply this model to describe the large-scale solids circulation that prevail in gas–solid reactors is new, however, and involves some slight modifications of the equivalent model for gas–liquid systems (Bokkers *et al.*, 2005a). To this end, the emulsion phase is modeled as a continuum—like the liquid in a gas–liquid bubble column—and the larger bubbles are treated as discrete bubbles. Note that granular systems have no surface tension, so in that respect there is a pronounced difference with the bubbles present in gas–liquid bubble columns. For instance, the gas will be free to flow through a bubble in gas–solid systems, which is not the case for gas–liquid systems. As far as the numerical part is concerned, the DBM strongly resembles the DPM as outlined in Section III, since it is also of the Euler–Lagrange type with the emulsion phase described by the volume-average Navier–Stokes equations:

$$\frac{\partial(\varepsilon_e \rho_e)}{\partial t} + \nabla \cdot (\varepsilon_e \rho_e \mathbf{u}_e) = 0 \tag{97}$$

with ρ_e, ε_e, and $\mathbf{u}_e$ the density, volume fraction, and flow velocity, respectively, of the emulsion phase. Momentum conservation gives that

$$\frac{\partial(\varepsilon_e \rho_e \mathbf{u}_e)}{\partial t} + \nabla \cdot (\varepsilon_e \rho_e \mathbf{u}_e \mathbf{u}_e) = -\varepsilon_e \nabla p - \mathrm{S}_E - \nabla \cdot (\varepsilon \bar{\bar{\tau}}_e) + \varepsilon_e \rho_e \mathbf{g} \tag{98}$$

where the symbols take their usual meaning, and the subscript "e" indicates emulsion phase. The term $\mathbf{S}_E$ accounts for the two-way coupling between the dispersed phase and the continuous phase. The bubbles are considered as discrete elements that are tracked individually according to Newton's second law of motion:

$$m_b \frac{d\mathbf{v}_b}{dt} = \mathbf{F}_{\mathrm{tot}} \tag{99}$$

where $\mathbf{F}_{\mathrm{tot}}$ is the sum of different forces acting on a single bubble:

$$\mathbf{F}_{\mathrm{tot}} = \mathbf{F}_g + \mathbf{F}_p + \mathbf{F}_d + \mathbf{F}_W + \mathbf{F}_{VM} \tag{100}$$

As in the DPM model, the total force on the bubble has contributions from gravity ($\mathbf{F}_g$), pressure gradients ($\mathbf{F}_p$), and drag from the interaction with emulsion phase ($\mathbf{F}_d$). The sum of $\mathbf{F}_g$ and $\mathbf{F}_p$ is equal to $(p_e - p)\ V_b \mathbf{g}$, with V_b the volume of the bubble. For the drag force on a single bubble (diameter d_b), the correlations for the drag force on a single sphere are used, only with a modified drag coefficient C_d, such that it yields the relation $v_{br} = 0.711\sqrt{g d_b}$ by Davies and Taylor (1950) for the rise velocity of a single bubble. Note that in Eq. (100), there are two forces present that are not included in the DPM, namely the wake force $\mathbf{F}_W$ and the virtual mass force $\mathbf{F}_{VM}$. The wake force, accounting for the acceleration of a bubble in the wake of a leading bubble, is neglected in this application; whereas for the virtual mass force, the relation by Auton (1983) is used:

$$\mathbf{F}_{VM} = -\left(\frac{D\mathbf{I}}{Dt} + \mathbf{I} \cdot \nabla \mathbf{u}\right), \quad \mathbf{I} = 0.5 \rho_e V_b (\mathbf{v}_b - \mathbf{u}_e)$$

An advantage of this approach to model large-scale fluidized bed reactors is that the behavior of bubbles in fluidized beds can be readily incorporated in the force balance of the bubbles. In this respect, one can think of the rise velocity, and the tendency of rising bubbles to be drawn towards the center of the bed, from the mutual interaction of bubbles and from wall effects (Kobayashi *et al.*, 2000). In Fig. 34, two preliminary calculations are shown for an industrial-scale gas-phase polymerization reactor, using the discrete bubble model. The geometry of the fluidized bed was $1.0 \times 3.0 \times 1.0$ m (w × h × d). The emulsion phase has a density of 400 kg/m^3, and the apparent viscosity was set to 1.0 Pa s. The density of the bubble phase was 25 g/m^3. The bubbles were injected via 49 nozzles positioned equally distributed in a square in the middle of the column.

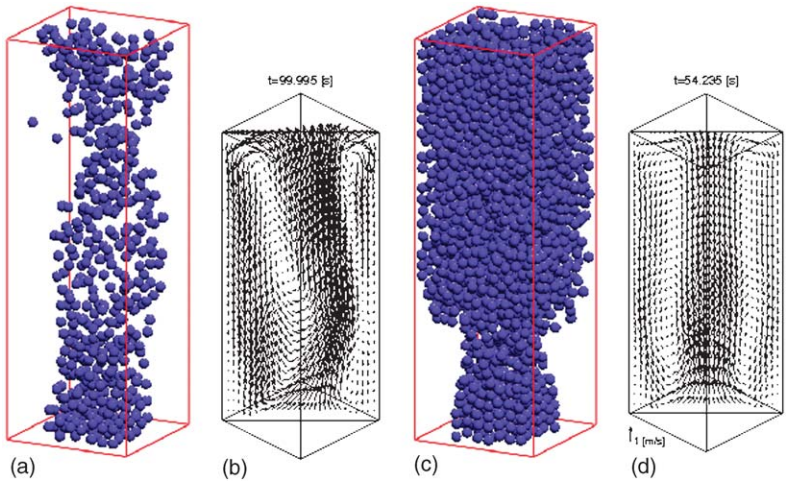

FIG. 34. Snapshots of the bubble hold-up in the DBM model without bubble coalescence, and the time average vector plot of the emulsion phase after 100 s of simulation; (a) + (b) $u_0 = 0.1$.

In Figs. 34a and 34c, snapshots are shown of the bubbles that rise in the fluidized bed with a superficial gas velocity of 0.1 m/s (a) and 0.3 m/s (c). It is clearly shown that the bubble holdup is much larger with a superficial gas velocity of 0.3 m/s. However, the number of bubbles in this case is too large, since bubble coalescence has not been accounted for in these simulations. In Figs. 34b and 34d, time-averaged plots are shown of the emulsion velocity after 100 s of simulation. The large convection patterns, upflow in the middle and downflow along the wall, are clearly demonstrated. Coalescence, which is a highly prevalent phenomenon in fluidized beds, is not included in the simulations described above. However, since all the bubbles are tracked individually, it is relatively straightforward to include this in the DBM. In the latest version of the DBM (Bokkers *et al.*, 2005a), a simple coalescence model is included, which was found to have a large effect on the macroscale circulation pattern. In this model, all the bubbles that "collide" will coalesce till a maximum size, where the largest bubbles start to breakup.

VI. Outlook

In this chapter, we have discussed three levels of modeling for dense gas–solid flows, with the emphasis on the technical details of each of the models, which have not been published elsewhere. Up till now, the models have mainly been used to obtain *qualitative* information, that is, to acquire insight into the mechanisms underlying the gas–solid flow structures. However, the ultimate objective of the multiscale approach is to obtain *quantitative*

information that can be fed into the higher level models. Such a program has just started at the University of Twente, and in Sections II.D and III.F we have shown some first results from this line of research. Much remains to be done, however; specifically for each level:

(i) For the LBM, we have presented a new drag-force correlation for ideal systems: homogeneous (unbounded) static arrays of perfect monodisperse spheres; in fluidized beds, however, such systems are hardly ever encountered. Therefore, the next step(s) would be to consider the effects of heterogeneity, mobility, and polydispersity. With respect to the latter, our LB studies for binary systems at very low Reynolds numbers showed that the drag-force relations that are currently used for such systems are wrong by up to a *factor* of 5, for relatively moderate diameter ratios of 1:4 (Van der Hoef *et al.*, 2005). For higher Reynolds numbers (100 and 500), the results show a similar trend (Beetstra *et al.*, 2006). Some preliminary results on size segregation indicate that our new drag-force relations have a large effect on the segregation phenomena in binary fluidized systems (Beetstra *et al.*, 2006). With respect to heterogeneous structures, it will be obvious that the drag force of clusters of spheres will be very different from that of a homogeneous suspension. We have recently performed an LBM study for small clusters (close-to-sphere and H-shaped), and the conclusion was that the effective drag of the cluster was equivalent to that of a large sphere that has the same (projected) surface area as the cluster, perpendicular to the direction of flow (Beetstra *et al.*, 2006).

(ii) In the DPM, future work will be focused on measuring the particulate pressure and viscosity, where it will be of particular interest to test how well the general Enskog relation in Eq. (75) between the viscosity and excess compressibility holds, which follows from kinetic theory, and if necessary adjust the equations on the basis of the simulation data. The next step would be to include the effect of the gas phase (drag), particle friction, van der Waals interactions, and also polydispersity. Note that the determination of the viscosity is not straightforward, and has to our knowledge not been measured previously in discrete particle simulations of fluidized beds. One option is to use methods from MD simulations (Allen and Tildesley, 1990)): statistical mechanics of nonequilibrium systems gives that the shear viscosity is equal to the time integral (Green–Kubo integral) of the stress–stress correlation function $\langle \sigma_{xy}(0)\sigma_{xy}(t) \rangle$, where σ_{xy} is the "microscopic" stress tensor, which can be written in terms of the particle positions, velocities, and forces (Hansen and McDonald, 1986; Allen and Tildesley, 1990). The second method is by measuring the velocity decay of the impact of a large sphere (diameter D) in a fluidized bed. When we assume that the collisions of the large intruder with the small bed particles take the effect of a Stokes–Einstein drag force $\sim 3\pi\mu_s D v$ on the large particle, with v the velocity of the intruder, then the effective solids viscosity

can be obtained directly. Our discrete particle simulations of such an impact in a bed of monodisperse particles are reported in Ref. Lohse *et al.* (2004).

(iii) With respect to the TFM, the main challenges are the simulations of polydisperse systems and fine powders. For the latter, we saw in Section IV.F that without an *ad hoc* scaling of the drag force, the current class of TFMs cannot predict the fluidization properties of A-powders. For even smaller particles, cluster-like structures might be formed, so that the application of the current version of KTGF should be seriously questioned in any case. In other words, it would be unlikely that a simple reduction of only gas–particle drag, as suggested by McKeen and Pugsley (2003), would suffice in that case. For *multidisperse* fluidized beds, the current class of TFMs still lacks the capability of describing quantitatively particle mixing and segregation rates. Recently, we have extended the KTGF to bidisperse systems (Bokkers, 2005; Bokkers *et al.*, 2006), and the next challenge would be to extend this to general polydisperse systems. Also in the current KTGF, the effect of particle–particle friction is not incorporated. A recent simulation study using the DPM showed that particle friction has a large influence on the mixing behavior when a single bubble is injected into the system (Bokkers *et al.*, 2006). It was also found that the effects of lack of friction could not be remedied by using a smaller coefficient of normal restitution, which implies that friction should be taken into account explicitly in the KTGF.

(iv) The models for describing industrial-scale gas–solid flow are clearly still in the preliminary stage. In this chapter, we have outlined two promising approaches and noted that much remains to be done before their usefulness as tools for the design and scale-up of chemical reactors can be ascertained. In Section V.B, we have demonstrated the potential value of the filtering approach. Many challenges still remain. It must be verified that results of the type shown in Figs. 31 and 32 persist in 3D; simple predictive theories to capture the filter-size dependence of the filtered drag coefficient and stresses must be developed, and the viability of this approach should be validated by comparison with experimental data.

For the discrete bubble model described in Section V.C, future work will be focused on implementation of closure equations in the force balance, like empirical relations for bubble-rise velocities and the interaction between bubbles. Clearly, a more refined model for the bubble–bubble interaction, including coalescence and breakup, is required along with a more realistic description of the rheology of fluidized suspensions. Finally, the adapted model should be augmented with a thermal energy balance, and associated closures for the thermophysical properties, to study heat transport in large-scale fluidized beds, such as FCC-regenerators and PE and PP gas-phase polymerization reactors.

REFERENCES

Agrawal, K., Loezos, P. N., Syamlal, M., and Sundaresan, S. J. *Fluid Mech* **445**, 151–185 (2001).
Alder, B. J., and Wainwright, T. E. *J. Chem. Phys.* **27**, 1208 (1957).
Alder, B. J., and Wainwright, T. E. *J. Chem. Phys.* **33**, 1439 (1960).
Alder, B. J., Gass, D. M., and Wainwright, T. E. *J. Chem. Phys.* **53**, 3813 (1970).
Allen, M. P., and Tildesley, D. J., "Computer Simulations of Liquids". Oxford Science Publications, Oxford, UK (1990).
Anderson, J. D., "Computational Fluid Dynamics: The Basics with Applications". McGraw-Hill, New York, USA (1995).
Anderson, T. B., and Jackson, R. *Ind. Eng. Chem. Fundam.* **6**, 527 (1967).
Anderson, T. B., and Jackson, R. *Ind. Eng. Chem. Fundam.* **7**, 12 (1968).
Anderson, T. B., and Jackson, R. *Ind. Eng. Chem. Fundam.* **8**, 137 (1969).
Anderson, K., Sundaresan, S., and Jackson, R. *J. Fluid Mech.* **303**, 327 (1995).
Andrews, A. T.IV, Loezos, P. N., and Sundaresan, S. *Ind. Eng. Chem. Res.* **44**, 6022–6037 (2005).
Andrews, A. T. IV., and Sundaresan, S. Closures for filtered two-fluid model equations of gas–particle flows, Manuscript in preparation (2006).
Auton, T. R., The dynamics of bubbles, drops and particles in motion in liquids, PhD thesis, University of Cambridge (1983).
Bayle, J., Mege, P., and Gauthier, T., Dispersion of bubble flow properties in a turbulent FCC fluidized bed, *in* "Fluidization X" (M. Kwauk, J. Li, and W. -C. Yang Eds.), pp. 125. Engineering Foundation, New York, USA (2001).
Beetstra, R., van der Hoef, M. A., and Kuipers, J. A. M. Drag force from lattice Boltzmann simulations of intermediate Reynolds number flow past mono- and bidisperse arrays of spheres, Manuscript submitted to *AIChE J.* (2006).
Beetstra, R., van der Hoef, M. A., and Kuipers, J. A. M. Numerical study of segregation using a new drag force correlation for polydisperse systems derived from lattice Boltzman simulations, Manuscript submitted the *Chem. Eng. Sci.* (2006, in press).
Beetstra, R., van der Hoef, M. A., and Kuipers, J. A. M., A lattice-Boltzmann simulation study of the drag coefficient of clusters of spheres, *Comput. Fluids* **35**, 966–970 (2006).
Bhatnagar, P., Gross, E., and Krook, M. *Phys. Rev.* **94**, 511 (1954).
Bird, G. A., "Molecular Gas Dynamics and Direct Simulation of Gas Flows". Oxford University Press, Oxford, UK (1976).
Bird, R. B., Stewart, W. E., and Lightfood, E. N., "Transport Phenomena". John Wiley & Sons, New York, USA (1960).
Boemer, A., Qi, H., Hannes, J., and Renz, U. Modelling of solids circulation in a fluidised bed with Eulerian approach. 29th IEA–FBC Meeting in Paris, France, Nov. 24–26, 1994 (1994).
Bokkers, G. A., Multi-level modelling of the hydrodynamics of gas phase polymerization reactors, PhD thesis, University of Twente (2005).
Bokkers, G. A., Van Sint Annaland, M., and Kuipers, J. A. M., Comparison of continuum models using kinetic theory of granular flow with discrete particle models and experiments: extent of particle mixing induced by bubbles. Proceedings of Fluidization XI, May 9–14, 2004, 187–194, Naples, Italy (2004).
Bokkers, G. A., Laverman, J. A., Van Sint Annaland, M., and Kuipers, J. A. M., Modelling of large-scale dense gas–solid bubbling fluidised beds using a novel discrete bubble model, *Chem. Eng. Sci.* **61**, 5590–5602 (2006).
Brendel, L., and Dippel, S., Lasting contacts in MD simulations, *in* "Physics of Dry Granular Media" (H. J. Herrmann, J. P. Hovi, and S. Luding Eds.), pp. 313–318. Kluwer Academic Publishers, Dordrecht (1998).
Campbell, C. S. *Ann. Rev. Fluid Mech.* **22**, 57 (1990).

Campbell, C. S., and Brennen, C. E. *J. Fluid Mech.* **151**, 167 (1985).
Carnahan, N. F., and Starling, K. E. *J. Chem. Phys.* **51**, 635 (1969).
Centrella, J., and Wilson, J. R. *Astrophys. J. Suppl. Ser.* **54**, 229 (1984).
Chapman, S., and Cowling, T. G., "The Mathematical Theory of Theory of Non-Uniform Gases". Cambridge University Press, Cambridge, UK (1970).
Chen, C. P., Studies in two-phase turbulence closure modeling, Ph.D. Thesis, Michigan State University, USA (1985).
Chen, Z., Gibilaro, L. G., and Foscolo, P. U. *Ind. Eng. Chem. Res.* **38**, 610 (1999).
Cundall, P. A., and Strack, O. D. L. *Géotechnique* **29**, 47 (1979).
Dasgupta, S., Jackson, R., and Sundaresan, S. *AIChE J* **40**, 215–228 (1994).
Davies, R. M., and Taylor, G. I. *Proc. R. Soc. Lond.* textbfA200, 375–390 (1950).
Delnoij, E., Kuipers, J. A. M., and van Swaaij, W. P. M. *Chem. Eng. Sci.* **52**, 3623 (1997).
Detamore, M. S., Swanson, M. A., Frender, K. R., and Hrenya, C. M. *Powder Technol* **116**, 190 (2001).
Ding, J., and Gidaspow, D. *AIChE J* **36**, 523 (1990).
Dufty, J. W. *J. Phys.: Condens. Mater.* **12**, 47 (2000).
Elghobashi, S. E., and Abou-Arab, T. W. *Phys. Fluids* **26**, 931 (1983).
Elgobashi, S. *Appl. Sci. Res.* **48**, 301–304 (1991).
Ergun, S. *Chem. Eng. Prog.* **48**, 89 (1952).
Ernst, M. H., and Dufty, J. W. *J. Stat. Phys.* **58**, 57 (1989).
Erpenbeck, J. J., and Wood, W. W. *J. Stat. Phys.* **35**, 321 (1984).
Ferschneider, G., and Mege, P. *Revue de l Institut français du pétrole* **51**, 301 (1996).
Frenkel, D., and Smit, B., "Understanding Molecular Simulation: From Algorithms to Applications". Academic Press, San Diego, USA (1996).
Frisch, U., d'Humières, D., Hasslacher, B., Lallemand, P., Pomeau, Y., and Rivet, J-P. *Complex Sys* **1**, 649 (1987).
Frisch, U., Hasslacher, B., and Pomeau, Y. *Phys. Rev. Lett.* **56**, 1505 (1986).
Geldart, D. *Powder Technol* **7**, 285 (1973).
Gidaspow, D., "Multiphase Flow and Fluidization: Continuum and Kinetic Theory Descriptions". Academic Press, Boston, USA (1994).
Goldhirsch, I. *Chaos* **9**, 659 (1999).
Goldschmidt, M. J. V., Beetstra, R., and Kuipers, J. A. *M. Powder Technol.* **142**, 23 (2004).
Goldschmidt, M. J. V., Kuipers, J. A. M., and van Swaaij, W. P. M. *Chem. Eng. Sci.* **56**, 571 (2001).
Hansen, J. -P., and McDonald, I. R., "Theory of Simple Liquids". Academic Press, London, UK (1986).
Harlow, F. H., and Amsden, A. A. *J. Comput. Phys.* **17**, 19 (1975).
Hawley, J. F., Smarr, L. L., and Wilson, J. R. *Astrophys. J. Suppl. Ser.* **55**, 211 (1984).
Helland, E., Occelli, R., and Tadrist, L. *CR Acad. Sci. II B* **327**, 1397 (1999).
Helland, E., Occelli, R., and Tadrist, L. *Powder Technol* **110**, 210 (2000).
Herrmann, H. J., and Luding, S. *Contin. Mech. Thermodyn.* **10**, 189 (1998).
Hill, R. J., Koch, D. L., and Ladd, A. J. *C. J. Fluid Mech.* **448**, 213 (2001a).
Hill, R. J., Koch, D. L., and Ladd, A. J. C. *J. Fluid Mech.* **448**, 243 (2001b).
Hoomans, B. P. B., Granular dynamics in gas–solids two-phase flows. Ph.D. dissertation, University of Twente, Enschede, The Netherlands (2000).
Hoomans, B. P. B., Kuipers, J. A. M., and van Swaaij, W. P. M. *Powder Technol* **109**, 41 (2000).
Hoomans, B. P. B., Kuipers, J. A. M., Briels, W. J., and van Swaaij, W. P. M. *Chem. Eng. Sci.* **47**, 99 (1996).
Hoover, W. G., and Ree, F. H. *J. Chem. Phys.* **49**, 3609 (1969).
Hrenya, C. M., and Sinclair, J. L. *AIChE J* **43**, 853–869 (1997).
Hunter, R. J. "Foundations of Colloid Science". vol. IClarendon Press, Oxford, UK (1986).
Ishii, M., "Thermo-Fluid Dynamic Theory of Two-Phase Flow". Eyrolles, Paris, France (1975).
Israelachvili, J., "Intermolecular & Surface Forces". Academic Press, London, UK (1991).

Iwadate, M., and Horio, M., Agglomerating fluidization of wet powders and group c powders: a numerical analysis, *in* "Fluidization IX" (L. S. Fan, and T. Knowlton Eds.), pp. 293. Engineering Foundation, Durango, USA (1998).
Jenkins, J. T., and Savage, S. B. *J. Fluid Mech.* **130**, 187 (1983).
Johnson, K. L., "Contact Mechanics". Cambridge University Press, Cambridge, UK (1985).
Kafui, K. D., Thornton, C., and Adams, M. J. *Chem. Eng. Sci.* **57**, 2395 (2002).
Kim, H., and Arastoopour, H. *Powder Technol* **122**, 83 (2002).
Kobayashi, N., Yamazaki, R., and Mori, S. *Powder Technol* **113**, 327 (2000).
Koch, D. L., and Hill, R. J. *Annu. Rev. Fluid Mech.* **33**, 619 (2001).
Kuipers, J. A. M., and van Swaaij, W. P. M. *Adv. Chem. Eng.* **24**, 227 (1998).
Kuipers, J. A. M., Hoomans, B. P. B, and van Swaaij, W. P. M. Hydrodynamic Modeling of Gas-Fluidized Beds and their Role for Design and Operation of Fluidized Bed Chemical Reactors. Proceedings of the Fluidization IX conference, 15–30, Durango, USA (1998).
Kuipers, J. A. M., van Duin, K. J., van Beckum, F. H. P., and van Swaaij, W. P. M. *Chem. Eng. Sci.* **47**, 1913 (1992).
Kunii, D., and Levenspiel, O., "Fluid Engineering". Butterworth Heinemann series in Chemical Engineering, London, UK (1991).
Ladd, A. J. C. *J. Fluid Mech.* **271**, 285 (1994).
Ladd, A. J. C., and Verberg, R. *J. Stat. Phys.* **104**, 1191 (2001).
Langston, P. A., Tüuzün, U., and Heyes, D. M. *Chem. Eng. Sci.* **49**, 1259 (1994).
Laux, H. Modeling of dilute and dense dispersed fluid-particle flow, PhD Thesis, NTNU Trondheim, Norway (1998).
Lettieri, P., Cammarata, L., Micale, G. D. M., and Yates, J. *Int. J. Chem. Reactor Eng.* **1**, A5 (2003).
Lettieri, P., Newton, D., and Yates, J. G. *Powder Technol* **123**, 221 (2002).
Lewis, E. W., and Bowerman, E. W. *Chem. Eng. Prog.* **48**, 603 (1952).
Li, J., and Kuipers, J. A. M. *Powder Technol* **127**, 173 (2002).
Li, J., and Kuipers, J. A. M. *Chem. Eng. Sci.* **58**, 711 (2003).
Li, J., and Kuipers, J. A. M. *Chem. Eng. Sci.* **60**, 1251 (2005).
Li, J., and Mason, D. J. *Powder Technol* **112**, 273 (2000).
Liboff, R. L., "Kinetic Theory". John Wiley & Sons, New York, USA (1998).
Link, J. M., Cuypers, L. A., Deen, N. G., and Kuipers, J. A. *M. Chem. Eng. Sci.* **60**, 3425 (2005).
Lohse, D., Bergmann, R., Mikkelsen, R., Zeilstra, C., Van der Meer, D., Versluis, M., Van der Weele, K., Van der Hoef, M. A., and Kuipers, J. A. M. *Phys. Rev. Lett.* **93**, 198003 (2004).
Luding, S., Collisions & contacts between two particles, *in* "Physics of Dry Granular Media" (H. J. Herrmann, J. P. Hovi, and S. Luding Eds.), p. 1–19. Kluwer Academic Publishers, Dordrecht (1998) Chpt. 5.
Lun, C. C. K. *Int. J. Multiphase flow* **26**, 1707 (2000).
Lun, C. K. K., Savage, S. B., Jeffrey, D. J., and Chepurniy, N. *J. Fluid Mech.* **140**, 223 (1984).
Ma, D., and Ahmadi, G. *J. Chem. Phys.* **84**, 3449 (1986).
Massimilla, L., Dons, G., and Zucchini, C. *Chem. Eng. Sci.* **27**, 2005 (1972).
McKeen, T. R., and Pugsley, T. S. *Powder Technol* **129**, 139 (2003).
McNamara, S., and Young, W. R. *Phys. Fluids* **4**, 496 (1992).
Morgan, J. P., Taylor, R. W., and Booth, F. L. *Powder Technol* **4**, 286 (1971).
Nieuwland, J. J., van Sint Annaland, M., Kuipers, J. A. M., and van Swaaij, W. P. M. *AIChE J* **42**, 1569 (1996).
O'Brien, T. J., and Syamlal, M Particle cluster effects in the numerical simulation of a circulating fluidized bed, in (A. Avidan, Ed.) Circulating Fluidized Bed Technology IV , Proceedings of the Fourth International Conference on Circulating Fluidized Beds, Hidden Valley Conference Center and Mountain Resort, August 1–5, 1993, Somerset, PA, (1993).
Ouyang, J., and Li, J. *Chem. Eng. Sci.* **54**, 2077 (1999).
Patankar, S. V., and Spalding, D. B. *Int. J. Heat Mass Transfer* **15**, 1787 (1972).
Qian, Y., d'Humières, D., and Lallemand, P. *Europhys. Lett.* **17**, 479 (1992).

Richardson, J. F., and Zaki, W. N. *Trans. Instn. Chem. Eng.* **32**, 35 (1954).
Samuelsberg, A., and Hjertager, B. H. *AIChE J* **42**, 1536 (1996).
Schäfer, J., Dippel, S., and Wolf, D. E. *J. Phys. I Fr.* **6**, 5 (1996).
Schiller, L., and Nauman, A. *V.D.I. Zeitung* **77**, 318 (1935).
Sinclair, J. L., and Jackson, R. *AIChE J* **35**, 1473 (1989).
Smagorinsky, J. *Monthly Weather Rev* **91**, 99–164 (1963).
Succi, S., "The Lattice Boltzmann Equation for Fluid Dynamics and Beyond". Oxford Science Publications, Clarendon Press, Oxford (2001).
Sundaresan, S. *AIChE J* **46**, 1102–1105 (2000).
Syamlal, M., MFIX Documentation: Numerical Techniques. DOE/MC-31346-5824. NTIS/DE98002029 (1998).
Syamlal, M., Rogers, W., and O'Brien, T. J., MFIX Documentation. U.S. Department of Energy, Federal Energy Technology Center, Morgantown, WV (1993).
Tsuji, Y., Kawaguchi, T., and Tanaka, T. *Powder Technol* **77**, 79 (1993).
Tsuo, Y. P., and Gidaspow, D. *AIChE J* **36**, 885 (1990).
Van der Hoef, M. A., Beetstra, R., and Kuipers, J. A. M. *J. Fluid Mech.* **528**, 233 (2005).
Van der Hoef, M. A., Van Sint Annaland, M., and Kuipers, J. A. M. *Chem. Eng. Sci.* **59**, 5157 (2004).
van Swaaij, W. P. M., Chemical reactors, *in* "Fluidization" Academic Press, London, UK J. F. Davidson, and R. Clift, Eds.), (1985).
Walton, O. R., Numerical simulation of inelastic frictional particle–particle interaction, *in* "Particulate Two-Phase Flow" (M. C. Roco Ed.), pp. 884. Butterworth-Heineman, Boston, USA (2004) Chap. 25.
Walton, O. R., and Braun, R. L. *J. Rheol.* **30**, 949 (1986).
Wen, C. Y., and Yu, Y. H. *Chem. Eng. Prog. Symp. Ser.* **62**, 100 (1966).
Whitmore, R. L. J. *Inst. Fuel* **30**, 328 (1957).
Woodcock, L. V. *Ann. N.Y. Acad. Sci.* **37**, 274 (1981).
Xu, B. H., and Yu, A. B. *Chem. Eng. Sci.* **52**, 2785 (1997).
Yang, N., Wang, W., Ge, W., Wang, L., and Li, J. *Ind. Eng. Chem. Res.* **43**, 5548–5561 (2004).
Ye, M., Van der Hoef, M. A., and Kuipers, J. A. M. *Chem. Eng. Res. Des.* **83**(A7), 833 (2005).
Zhang, D. Z., and VanderHeyden, W. B. *Int. J. Multiphase Flow.* **28**, 805–822 (2002).
Zhou, H., Flamant, G., Gauthier, D., and Flitris, Y. *Chem. Eng. Res. Des.* **81**, 1144 (2003).
Zhou, H., Flamant, G., Gauthier, D., and Lu, J. *Chem. Eng. Res. Des.* **82**, 918 (2004).
Zhou, L. X., and Huang, X. Q. *Sci. China* **33**, 428 (1990).